Nanofiber quantum photonics

Nanofiber quantum photonics

Nanofiber quantum photonics

Kali P Nayak[1], **Mark Sadgrove**[2], **Ramachandrarao Yalla**[1],
Fam Le Kien[3] **and Kohzo Hakuta**[1]

Abstract. Recent advances in the coherent control of single quanta of light, *photons*, is a topic of prime interest and is discussed under the common banner of *quantum photonics*. In the last decade, the subwavelength diameter waist of a tapered optical fiber, referred to as an *optical nanofiber*, has opened promising new avenues in the field of quantum optics, paving the way towards a versatile platform for quantum photonics applications. The key features of the technique are that the optical field can be tightly confined in the transverse direction while propagating over long distances as a guided mode and enabling strong interaction with the surrounding medium in the evanescent region. These features have led to surprising possibilities to manipulate single atoms and fiber-guided photons, e.g. efficient channeling of emission from single atoms and solid-state quantum emitters into the fiber guided modes, high optical depth with a few atoms around the nanofiber, trapping atoms around a nanofiber and atomic memories for fiber-guided photons. Furthermore, implementing a moderate longitudinal confinement in nanofiber cavities has enabled the strong-coupling regime of cavity quantum electrodynamics to be reached, and the long-range dipole-dipole interaction between quantum emitters mediated by the nanofiber offers a platform for quantum non-linear optics with an ensemble of atoms. In addition, the presence of the longitudinal component of the guided field has led to the unique capabilities for chiral light-matter interactions on nanofibers. In this article, we review the key developments of the nanofiber technology towards a vision for quantum photonics on an all-fiber interface.

[1] Center for Photonic Innovations, The University of Electro-Communications, Chofu, Tokyo 182-8585, Japan
[2] Research Institute of Electrical Communication, Tohoku University, Aoba-ku, Sendai 980-8577, Japan
[3] Quantum Systems Unit, Okinawa Institute of Science and Technology Graduate University, Onna, Okinawa 904-0495, Japan

E-mail: `k.hakuta@cpi.uec.ac.jp`

1. Introduction

The goal of ultimate control of single quanta of light, i.e. *single photons*, has driven researchers to a new era of *quantum photonics* [1, 2]. The field of quantum photonics deals with generation, detection and coherent manipulation of photonic quantum states for applications like quantum computing [3], quantum communication [4], quantum simulation [5, 6], quantum metrology [7] and so on. In this context, a key challenge is to realize an efficient interface for coherent transfer of quantum states between atomic and photonic qubits [4].

The interaction strength between a single atom and photons is determined by the overlap between the transverse spread of the photonic mode and the atomic absorption cross-section $\sigma = \frac{3\lambda^2}{2\pi}$, where λ is the wavelength of atomic resonance. Therefore strong transverse confinement of the photonic mode to subwavelength dimensions is an essential requirement to achieve efficient interaction. The atom-photon interaction can also be enhanced by implementing longitudinal confinement of the photonic mode in high-finesse optical cavities leading to cavity quantum electrodynamic (QED) effects [8, 9].

Over the past several decades the interaction of single atoms and photons in high-finesse, free-space, optical Fabry-Perot (FP) cavities has been investigated in numerous studies [4, 8, 9, 10, 11]. However, in the past decade there have been significant advances in implementing the transverse confinement of photonic modes in nanophotonic waveguides and cavities to realize hybrid quantum interfaces. Examples include, but are not limited to, photonic crystal waveguides and cavities [12, 13, 14], whispering gallery mode (WGM) cavities [15, 16, 17] and plasmonic nanostructures [18, 19, 20]. In a different approach, new ideas have also emerged to control single photons using quantum coherence in multiple emitters [21, 22]. Using electro-magnetically induced transparency (EIT), single photons can be coherently stored in an atomic ensemble as a collective excitation. Moreover, such a collective excitation can be efficiently retrieved from the atomic ensemble as a single photon.

In 2002, Hakuta and co-workers proposed a novel idea to control fiber guided light using EIT in a setting where the guided light of a subwavelength diameter silica optical fiber interacts with the surrounding medium in the evanescent region [23]. The key features of the technique are the strong transverse confinement of the guided field, the long interaction length along the fiber and the fiber-in-line property (i.e. the effect occurs in a subwavelength-diameter section of a tapered standard single-mode optical fiber), which is not easily achievable in other nanophotonic

systems. Shortly after this proposal, in 2003 Tong *et al* reported the fabrication and study of properties of silica nanowires for photonic applications [24]. Since then the study of subwavelength diameter optical fibers, referred to as *optical nanofibers*, has been of increasing interest to the scientific community. Optical nanofibers have been widely adapted for diverse applications ranging from nonlinear optics, nanophotonics, quantum optics and quantum photonics [25, 26, 27, 28].

In particular, in the last decade optical nanofibers have shown promising new avenues in quantum photonics. Following the pioneering works, between 2004 to 2007 Kien *et al* have reported a series of theoretical proposals on interfacing neutral atoms with nanofibers e.g. trapping atoms around a nanofiber [29, 30], efficient channeling of single-atom emission into the nanofiber guided modes [31] and efficient scattering of the nanofiber guided light by a single atom [32]. Moreover, the theoretical proposals were promptly followed by early experimental demonstrations of the atom-nanofiber interface. In 2007, Nayak *et al* [33] and Sague *et al* [34] experimentally demonstrated the efficient channeling of few-atom fluorescence into nanofiber guided modes and the efficient scattering of the guided light by a few laser-cooled atoms around the nanofiber, respectively.

Following these pioneering demonstrations, there have been several milestone experimental demonstrations that have enabled optical nanofibers as a workbench for quantum photonics applications. Photon correlation measurements have demonstrated detection of single-atom fluorescence through the nanofiber guided modes [35, 36]. Trapping atoms using nanofiber guided modes has enabled an optically dense quantum interface [37, 38]. Not only atoms but single solid-state quantum emitters like quantum dots [39, 40] and nanodiamonds [41, 42] have been interfaced with nanofiber guided modes leading to the measurement of channeling efficiency [43] of fluorescence photons into the nanofiber guided modes.

More recently, EIT and photon storage experiments [44, 45] along with experiments demonstrating Bragg reflection [46, 47] from an array of trapped atoms on a nanofiber, have opened a route towards quantum nonlinear optics with atomic ensembles. In order to further enhance the atom-photon coupling at the single-atom level, new prospects for cavity QED on nanofibers have been proposed [48] and various types of nanofiber cavities have been demonstrated [49, 50, 51, 52, 53]. This has led to demonstrations of Purcell enhancement [52] and the strong-coupling regime of cavity QED [54], paving the way towards quantum nonlinear optics with single atoms. Moreover, a detailed understanding of the longitudinal polariza-

tion component of the nanofiber guided modes, has led to demonstrations of chiral light-matter interaction on nanofibers such as directional spontaneous emission [55] and non-reciprocal light transmission [56] using an array of atoms trapped on the nanofiber. Such chiral light-matter interaction may open unique possibilities for quantum photonic applications.

The purpose of this article is to review the progress and present status of nanofiber technology in the context of quantum photonics. The review is organized as follows. In Section 2, we review the fundamental aspects of the nanofiber guided field and its interaction with atoms from a theoretical point of view. First we discuss the field distribution and transverse confinement of the fundamental guided mode of the nanofiber. Then we discuss the interaction between an atom and the nanofiber guided modes i.e. modified spontaneous emission and channeling of atomic fluorescence into nanofiber guided modes, scattering of guided light by an atom and trapping atoms using the optical dipole potential induced by the guided light. In Section 3, we review the technical aspects of fabricating and characterizing high quality nanofibers.

In Section 4, we review the experimental demonstrations for interfacing laser-cooled atoms with nanofiber guided modes. This includes spectroscopy and photon correlation measurement of atomic fluorescence coupled into the nanofiber guided modes, trapping atoms using nanofiber guided modes, scattering of the guided field by atoms under various settings leading to Bragg reflection and non-reciprocal light transmission and EIT and photon storage experiments. In Section 5, we review the experimental demonstrations for interfacing solid-state quantum emitters like quantum dots and nanodiamonds with nanofibers. This includes deposition techniques, spectroscopy and photon correlation measurement of single emitters on a nanofiber and measurement of channeling efficiency into nanofiber guided modes.

In Section 6, we review the prospects and experimental demonstrations of cavity QED on optical nanofibers. This includes demonstration of various types of nanofiber cavities along with demonstration of cavity QED effects under Purcell and strong-coupling regimes. In Section 7, we conclude the review with a brief outlook for future developments.

2. Fundamental aspects of the field in nanofiber guided modes

In this section we review the fundamental aspects of the nanofiber guided field and its interaction with atoms from a theoretical point of view. First we discuss the field distribution and transverse confinement
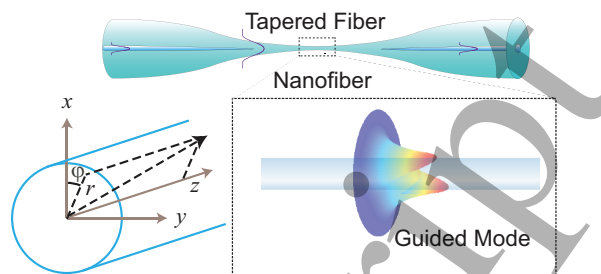

Figure 1. Schematic diagram showing the guided mode propagation in the nanofiber region of a tapered optical fiber.

of the fundamental guided mode of the nanofiber. Then we discuss several aspects of the interaction between an atom and the nanofiber guided modes, namely modified spontaneous emission and channeling of atomic fluorescence into nanofiber guided modes, scattering of guided light by an atom and trapping atoms using the optical dipole potential induced by the guided light.

2.1. Strong confinement of a single-mode optical nanofiber guided field

A brief schematic of light propagation in a nanofiber is shown in Fig. 1. The nanofiber is the subwavelength-diameter waist of a tapered single-mode optical fiber. A typical single-mode optical fiber consists of a central core with a diameter of 4-9 μm that guides the light and a surrounding clad with a diameter of 125 μm. Therefore by tapering the original fiber to form a nanofiber waist, the core of the original fiber almost vanishes at the nanofiber region. The cladding material of the original fiber serves as the core of the nanofiber and the surrounding medium serves as the clad. Details of the adiabatic coupling between modes of the original fiber and the nanofiber are discussed in the next section. In this subsection, we will discuss the intensity distribution and polarization orientation of the mode of an optical nanofiber that has a cylindrical, subwavelength-diameter silica core and an infinite vacuum clad. It should be noted that due to its thin diameter the nanofiber can support only the fundamental HE$_{11}$ mode which has no cut-off frequency. Therefore throughout this paper we discuss only the fundamental HE$_{11}$ mode.

2.1.1. Field distribution of fundamental mode with quasilinear polarization A brief description of light propagation in step-index optical fibers can be found in Appendix A. A detailed treatment of these issues can also be found in [57, 58, 59, 60, 61]. Here we present the field distribution of a fundamental mode of the nanofiber with quasilinear polarization. The radius of

Nanofiber quantum photonics 4

the nanofiber is a and the refractive index is n_1. The surrounding cladding medium has a refractive index n_2. We consider light of wavelength λ, frequency ω and free-space wave number $k = 2\pi/\lambda = \omega/c$, propagating in the nanofiber. Without loss of generality, we assume that the mode propagates in the forward direction. In the cylindrical coordinates (r, φ, z), the solutions of Maxwell's equations for the Cartesian components of the electric field amplitude $\boldsymbol{\mathcal{E}}$ in such a mode are given, for $r < a$ (inside the fiber), by

$$
\begin{aligned}
\mathcal{E}_x = &\, \mathrm{i}A\frac{\beta}{2h}[(1-s)J_0(hr)\cos\varphi_0 \\
&- (1+s)J_2(hr)\cos(2\varphi - \varphi_0)], \\
\mathcal{E}_y = &\, \mathrm{i}A\frac{\beta}{2h}[(1-s)J_0(hr)\sin\varphi_0 \\
&- (1+s)J_2(hr)\sin(2\varphi - \varphi_0)], \\
\mathcal{E}_z = &\, AJ_1(hr)\cos(\varphi - \varphi_0),
\end{aligned}
\tag{1}
$$

and, for $r > a$ (outside the fiber), by

$$
\begin{aligned}
\mathcal{E}_x = &\, \mathrm{i}A\frac{\beta}{2q}\frac{J_1(ha)}{K_1(qa)}[(1-s)K_0(qr)\cos\varphi_0 \\
&+ (1+s)K_2(qr)\cos(2\varphi - \varphi_0)], \\
\mathcal{E}_y = &\, \mathrm{i}A\frac{\beta}{2q}\frac{J_1(ha)}{K_1(qa)}[(1-s)K_0(qr)\sin\varphi_0 \\
&+ (1+s)K_2(qr)\sin(2\varphi - \varphi_0)], \\
\mathcal{E}_z = &\, A\frac{J_1(ha)}{K_1(qa)}K_1(qr)\cos(\varphi - \varphi_0),
\end{aligned}
\tag{2}
$$

where $s = [(qa)^{-2} + (ha)^{-2}]/[J_1'(ha)/haJ_1(ha) + K_1'(qa)/qaK_1(qa)]$ [57, 58, 59]. Here the parameters $h = (n_1^2 k^2 - \beta^2)^{1/2}$ and $q = (\beta^2 - n_2^2 k^2)^{1/2}$ characterize the fields inside and outside the fiber, respectively. The longitudinal propagation constant β is determined by the fiber eigenvalue equation discussed in appendix A. J_n and K_n stand for the Bessel functions of the first kind and the modified Bessel functions of the second kind, respectively. The coefficient A is determined by the normalization condition. The angle φ_0 determines the orientation axis of the polarization of the field. The angles $\varphi_0 = 0$ and $\varphi_0 = \pi/2$ correspond to polarizations aligned along the x and y axes, respectively.

In the case of nanofibers, the decay parameter qa of the evanescent wave may become sufficiently small. As a result, $K_1(qa)$ and $K_2(qa)$ may become much larger than $K_0(qa)$. Hence, the terms containing $K_1(qr)$ and $K_2(qr)$ in the expressions (2) may become significant in the outer vicinity of the fiber surface. This leads to a substantial longitudinal component $\mathcal{E}_z$ and azimuthal dependences of the transverse components $(\mathcal{E}_x, \mathcal{E}_y)$ of the field outside the fiber. In addition, it may be seen that the longitudinal component has a $\pi/2$ phase difference from the transverse components. This leads to polarization rotation along the axial plane. So we see that the
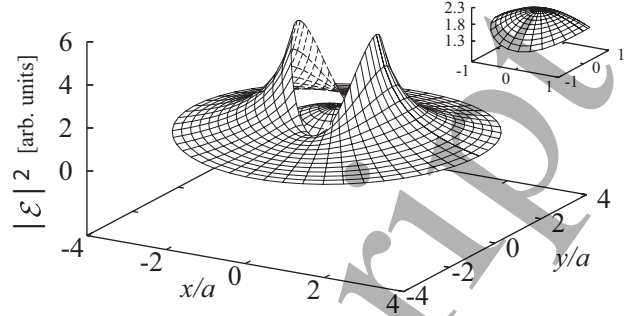

Figure 2. The transverse profile of the total intensity $|\mathcal{E}|^2$ of the electric field in a fundamental mode with quasilinear polarization. The inset shows the intensity profile of the field inside the fiber. The parameters used: $a = 200$ nm, $\lambda = 1.3\,\mu m$, $n_1 = 1.4469$, $n_2 = 1$ and $\varphi_0 = 0$. From Fam Le Kien *et al* [60].

properties of the exact fundamental mode HE_{11} may become substantially different from that of the linearly polarized mode LP_{01}.

Figure 2 shows the total intensity $|\mathcal{E}|^2$ of the electric field in a fundamental mode with quasilinear polarization. The major orientation axis of polarization is chosen along the x axis ($\varphi_0 = 0$). It may be seen that the profiles inside and outside the fiber are very different from each other. The spatial distribution of the field intensity is not cylindrically symmetric at all. A conspicuous discontinuity of the field intensity is observed at the fiber surface. This discontinuity is due to the boundary condition for the normal component of the electric field. The high contrast between the refractive indices n_1 and n_2 of the silica core and the vacuum clad, respectively, makes this effect dramatic.

Figure 3 shows the cross-section profiles of the intensities $|\mathcal{E}_x|^2$, $|\mathcal{E}_y|^2$ and $|\mathcal{E}_z|^2$ of the Cartesian-coordinate components of the electric field. We observe that the intensities $|\mathcal{E}_y|^2$ and $|\mathcal{E}_z|^2$ are weaker than the intensity $|\mathcal{E}_x|^2$. However, $|\mathcal{E}_y|^2$ and $|\mathcal{E}_z|^2$ are not negligible at all. Outside the fiber, $|\mathcal{E}_x|^2$ and $|\mathcal{E}_y|^2$ substantially depend on φ.

We note that the orientation of the total transverse component vector $\mathbf{E}_\perp = \mathrm{Re}[(\mathcal{E}_x\hat{\mathbf{x}} + \mathcal{E}_y\hat{\mathbf{y}})\mathrm{e}^{-\mathrm{i}(\omega t - \beta z)}]$ does not vary in time. However, the total electric field $\mathbf{E} = \mathrm{Re}[(\mathcal{E}_x\hat{\mathbf{x}} + \mathcal{E}_y\hat{\mathbf{y}} + \mathcal{E}_z\hat{\mathbf{z}})\mathrm{e}^{-\mathrm{i}(\omega t - \beta z)}]$ rotates elliptically with time, in a plane parallel to the fiber axis z.

2.1.2. Optimum field confinement and nanofiber diameter A key aspect of the nanofiber method is the strong transverse confinement of the guided optical field along with significant penetration length in the evanescent region to realize strong interaction with the surrounding medium. From a qualitative argument it may be seen that if the nanofiber is very thick the transverse confinement is weak. On the other hand, if
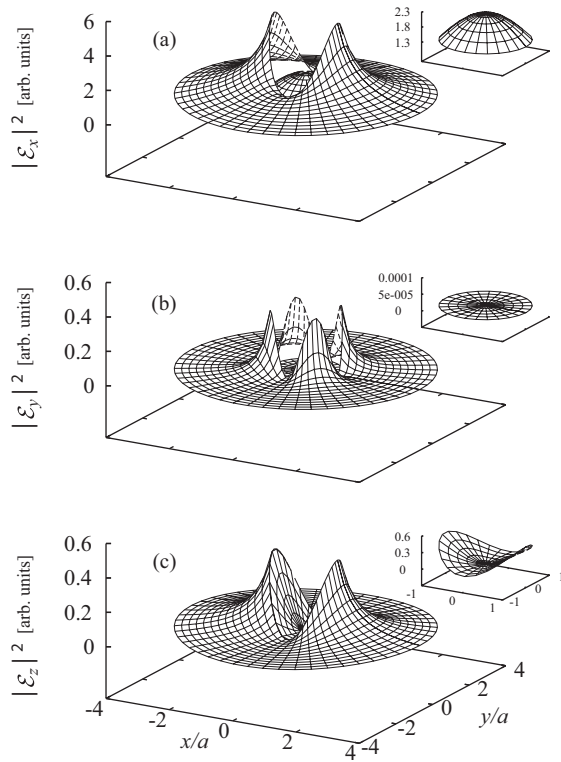
Figure 3. The transverse profiles of the intensities $|\mathcal{E}_x|^2$, $|\mathcal{E}_y|^2$ and $|\mathcal{E}_z|^2$ of the Cartesian-coordinate components of the electric field in a fundamental mode with quasilinear polarization. The insets show the intensity profiles of the field inside the fiber. The parameters used are as for figure 2. From Fam Le Kien *et al* [60].
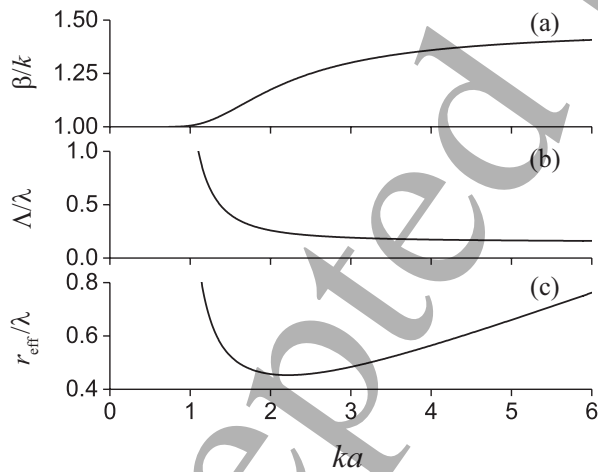

Figure 4. (a) Propagation constant β, (b) evanescent-wave penetration length Λ, and (c) effective mode radius r_{eff} of the fundamental HE_{11} mode as functions of the fiber size parameter ka. The wavelength of the light is chosen to be $\lambda = 852$ nm. The refractive index of the fiber is $n_1 = 1.4525$ and of the surrounding medium is $n_2 = 1$.

the fiber is too thin, the guided mode penetrates too deeply into the outside of the fiber resulting in weak

confinement. Therefore there must be some optimum diameter for which the transverse confinement will be strongest. In the following we discuss the parameters which determine this optimum nanofiber diameter.

We plot in Fig. 4, the propagation constant β, the evanescent-wave penetration length Λ, and the effective mode radius r_{eff} of the fundamental HE_{11} mode as functions of the fiber size parameter ka. The evanescent-wave penetration length of the nanofiber guided mode is given by $\Lambda = 1/q$. The effective mode radius is $r_{\mathrm{eff}} = \sqrt{A_{\mathrm{eff}}/\pi}$, where $A_{\mathrm{eff}} (= (\int |\mathbf{e}|^2 d\mathbf{r})^2 / \int |\mathbf{e}|^4 d\mathbf{r})$ is the effective mode area. The figure shows that r_{eff} has a minimum, and that the minimum value can be less than half of wavelength of light. Thus, when the nanofiber radius a is small enough but not too small, the guided field is tightly confined in the transverse plane, the evanescent-wave field can penetrate deeply into space, and the gradient of the field is steep.

2.2. Efficient interface for quantum emitters and fiber guided photons

The subwavelength confinement, the deep penetration into the surrounding medium, and the steep intensity gradient of the nanofiber guided field in the evanescent region open new possibilities to tailor light-matter interactions using a fiber mode. From the viewpoint of quantum optics we address the following three fundamental aspects of light-matter interaction. 1) Due to the strong confinement of the guided field, the spontaneous emission from atoms can be substantially modified around the nanofiber and a significant fraction of a single atom's emission can be channeled into the fiber guided mode. 2) Atoms and photons can be confined within the single-atom absorption cross-section leading to efficient scattering of the guided field by a single atom. 3) The steep gradient of the guided field can be used for trapping atoms around nanofiber using the optical dipole potential. In the following we present theoretical descriptions of these three fundamental aspects of nanofiber light-matter interfaces.

2.2.1. Modified spontaneous emission of an atom around a nanofiber The confinement of the guided modes substantially affects the spontaneous emission process and consequently enhances the coupling between quantum emitters and fiber guided modes [31, 62, 63, 64, 65]. Radiative decay of an atom in the vicinity of a nanofiber has been studied in the context of a two-level atom [62, 63, 64] as well as for realistic multilevel atoms including the hyperfine structure (hfs) of the energy levels [31, 65]. The parameters for the decay of populations [31, 62, 63, 64, 65] and cross-level coherences [31, 65] have been calculated.

Nanofiber quantum photonics 6

We follow Ref. [31] closely to demonstrate efficient radiative coupling between a multilevel atom and the guided modes of a nanofiber. We consider a cesium atom in the vicinity of a nanofiber (see the upper part of Fig. 5). The refractive index n_1 of the fiber is taken to be 1.45. The fiber axis z is taken to be the quantization axis for the atomic states. We study the cesium D_2 line, which occurs at the wavelength $\lambda_0 = 852$ nm. We introduce the notations $e \equiv e_{M'}$ and $g \equiv g_M$ for the magnetic sublevels $F'M'$ and FM of the hfs levels $6P_{3/2}F' = 5$ and $6S_{1/2}F = 4$, respectively. The coupling between $e_{M'}$ and g_M by spontaneous emission is illustrated in the lower part of Fig. 5.

In the interaction picture, the atomic dipole operator is given by

$$\mathbf{D} = \sum_{eg}(\mathbf{d}_{eg}^*\sigma_{ge}e^{-i\omega_0 t} + \mathbf{d}_{eg}\sigma_{ge}^\dagger e^{i\omega_0 t}). \tag{3}$$

Here the operators $\sigma_{ge} = |g\rangle\langle e|$ and $\sigma_{ge}^\dagger = \sigma_{eg} = |e\rangle\langle g|$ describe the downward and upward transitions, respectively, and $\mathbf{d}_{eg} = \langle e|\mathbf{D}|g\rangle e^{-i\omega_0 t}$ is the dipole matrix element. We introduce the notations $d^{(-1)} = (d_x - id_y)/\sqrt{2}$, $d^{(0)} = d_z$, and $d^{(1)} = -(d_x + id_y)/\sqrt{2}$ for the spherical tensor components of the dipole vector $\mathbf{d}$.
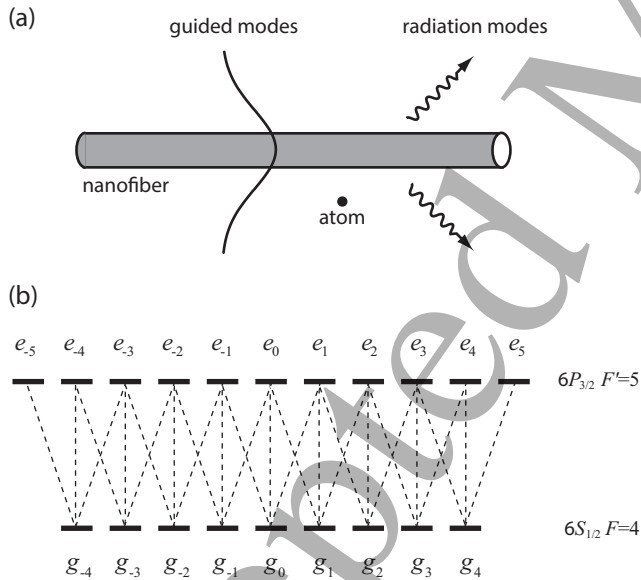
(a)

(b)

Figure 5. (a) An atom interacting with guided and radiation modes in the vicinity of an optical nanofiber. (b) Schematic of the $6P_{3/2}F' = 5$ and $6S_{1/2}F = 4$ hfs levels of a cesium atom. From Fam Le Kien *et al* [31].

We decompose the positive-frequency part $\mathbf{E}^{(+)}$ of the electric component of the field into the contributions from the guided and radiation modes as $\mathbf{E}^{(+)} = \mathbf{E}_{\text{guided}}^{(+)} + \mathbf{E}_{\text{rad}}^{(+)}$. The continuum field quantization follows the procedures presented in [66, 67, 68]. Regarding the guided modes, it is assumed

that the single-mode condition [57, 58, 59] is satisfied for the field frequency ω around the cesium D_2-line frequency ω_0. Each guided mode is labelled by an index $\mu = (\omega, f, p)$, where $f = +, -$ denotes forward or backward propagation direction, and $p = +, -$ denotes the counterclockwise or clockwise rotation of polarization. After quantization of the field in the guided modes, the following expression is obtained for $\mathbf{E}_{\text{guided}}^{(+)}$ in the interaction picture:

$$\mathbf{E}_{\text{guided}}^{(+)} = i\sum_\mu \sqrt{\frac{\hbar\omega\beta'}{4\pi\epsilon_0}}\, a_\mu \mathbf{e}^{(\mu)}e^{-i(\omega t - f\beta z - p\varphi)}. \tag{4}$$

Here β is the longitudinal propagation constant, β' is the derivative of β with respect to ω, a_μ is the respective photon annihilation operator, $\mathbf{e}^{(\mu)} = \mathbf{e}^{(\mu)}(r, \varphi)$ is the electric-field profile function of the guided mode μ in the classical problem (see Appendix A), and $\sum_\mu = \sum_{fp}\int_0^\infty d\omega$ is the summation over the guided modes.

Each radiation mode is labelled by the index $\nu = (\omega, \beta, m, p)$, where $m = 0, \pm 1, \pm 2, \ldots$ is the mode order and $p = \pm$ is the mode polarization. After quantization of the field in the radiation modes, the following expression is obtained for $\mathbf{E}_{\text{rad}}^{(+)}$ in the interaction picture:

$$\mathbf{E}_{\text{rad}}^{(+)} = i\sum_\nu \sqrt{\frac{\hbar\omega}{4\pi\epsilon_0}}\, a_\nu \mathbf{e}^{(\nu)}e^{-i(\omega t - \beta z - m\varphi)}. \tag{5}$$

Here a_ν is the respective photon annihilation operator, $\mathbf{e}^{(\nu)} = \mathbf{e}^{(\nu)}(r, \varphi)$ is the electric-field profile function of the radiation mode ν in the classical problem (see Appendix B), and $\sum_\nu = \sum_{mp}\int_0^\infty d\omega \int_{-k}^k d\beta$ is the summation over the radiation modes.

Assume that the atom is located at a point (r, φ, z). In the dipole and rotating-wave approximations, the coupling coefficients $G_{\mu eg}$ and $G_{\nu eg}$ of the atomic transition $e \leftrightarrow g$ with the guided mode $\mu = (\omega, f, p)$ and the radiation mode $\nu = (\omega, \beta, m, p)$, respectively, are given by the expressions

$$G_{\mu eg} = \frac{1}{\sqrt{Z_\mu}}\sqrt{\frac{\omega\beta'}{4\pi\epsilon_0\hbar}}\left(\mathbf{d}_{eg}\cdot\mathbf{e}^{(\mu)}\right)e^{i(f\beta z + p\varphi)},$$

$$G_{\nu eg} = \frac{1}{\sqrt{Z_\nu}}\sqrt{\frac{\omega}{4\pi\epsilon_0\hbar}}\left(\mathbf{d}_{eg}\cdot\mathbf{e}^{(\nu)}\right)e^{i(\beta z + m\varphi)}, \tag{6}$$

where Z_μ and Z_ν are the normalization constants and are determined by the equations

$$Z_\mu = \int_0^{2\pi} d\varphi \int_0^\infty n_{\text{rf}}^2 |\mathbf{e}^{(\mu)}|^2\, rdr \tag{7}$$

and

$$Z_\nu = \int_0^\infty d\omega \int_0^{2\pi} d\varphi \int_0^\infty n_{\text{rf}}^2 \left[\mathbf{e}^{(\nu)}\mathbf{e}^{(\nu')*}\right]_{\beta=\beta', m=m', p=p'} rdr. \tag{8}$$

Nanofiber quantum photonics   7

Here $n_{\rm rf}(r) = n_1$ for $r < a$, and $n_{\rm rf}(r) = n_2$ for $r > a$. The quantity $|\mathbf{e}^{(\mu)}|/\sqrt{Z_\mu}$ depends on the confinement of the guided mode in the fiber transverse plane. This quantity can be considered as the inverse of the square root of the local effective mode area.

We assume that the atom is initially prepared in the excited state $|e\rangle$ and the field is initially in the vacuum state $|0\rangle$. In this case, the total decay rate (Γ_{ee}) of the excited state population is given as the sum of decay rate into guided ($\gamma_{ee}^{(\rm g)}$) and radiation ($\gamma_{ee}^{\rm r}$) modes as follows

$$\Gamma_{ee} = \gamma_{ee}^{(\rm g)} + \gamma_{ee}^{(\rm r)}. \tag{9}$$

The decay rates into guided and radiation modes are given by

$$\gamma_{ee}^{(\rm g)} = 2\pi \sum_g \sum_\mu |G_{\mu eg}|^2 \tag{10}$$

$$\gamma_{ee}^{(\rm r)} = 2\pi \sum_g \sum_\nu |G_{\nu eg}|^2.$$

The channeling efficiency into the guided modes can be defined as

$$\eta = \frac{\gamma_{ee}^{(\rm g)}}{\Gamma_{ee}} = \frac{\gamma_{ee}^{(\rm g)}}{\gamma_{ee}^{(\rm g)} + \gamma_{ee}^{(\rm r)}}. \tag{11}$$
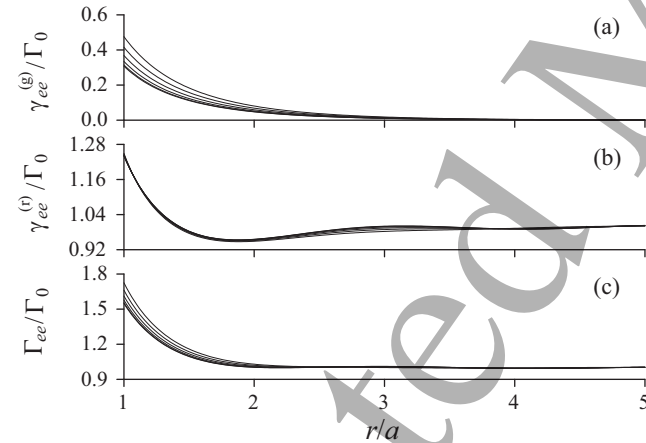

Figure 6. Spontaneous emission rates into (a) guided modes, (b) radiation modes, and (c) both types of modes, for the magnetic sublevels $6P_{3/2}F' = 5 M'$, plotted as functions of the position of the atom. The fiber axis z is the quantization axis. In each plot, different lines correspond to different values $|M'| = 0, 1, 2, 3, 4$, and 5. The fiber radius is $a = 200$ nm and the wavelength of the atomic transition is $\lambda_0 = 852$ nm. The refractive indices of the fiber and the vacuum clad are $n_1 = 1.45$ and $n_2 = 1$, respectively. The rates are normalized to the free-space decay rate $\Gamma_0 = 33 \times 10^6$ s^{-1}. From Fam Le Kien *et al* [31].

In the following, we discuss the results of numerical calculations of Ref. [31] for the decay characteristics of magnetic sublevels of a cesium atom in the presence of a nanofiber. The plots in Fig. 6 show

the spatial dependence of the spontaneous emission rates for various magnetic sublevels $6P_{3/2}F' = 5 M'$ into guided modes, radiation modes, and both types of modes. The fiber radius a is chosen to be 200 nm. It can be seen from Fig. 6 that different magnetic sublevels of the same state $6P_{3/2}$ have different decay rates in the vicinity of the nanofiber surface, unlike the case of atomic cesium in free space. The presence of the nanofiber produces substantial decay rates into the guided modes. In addition, the decay rates into radiation modes $\gamma_{ee}^{(\rm r)}$ and the total decay rates Γ_{ee} are enhanced from the free-space rate Γ_0 by small factors. As expected, the effect of the nanofiber on the decay rates is largest for the atom on the nanofiber surface. When the atom is far away from the nanofiber, $\gamma_{ee}^{(\rm g)}$ reduces to zero while $\gamma_{ee}^{(\rm r)}$ and Γ_{ee} approach the free-space value Γ_0. The small oscillations around the value of unity in Fig. 6(b) can be ascribed to the constructive/destructive interference due to reflections from the nanofiber surface [63].
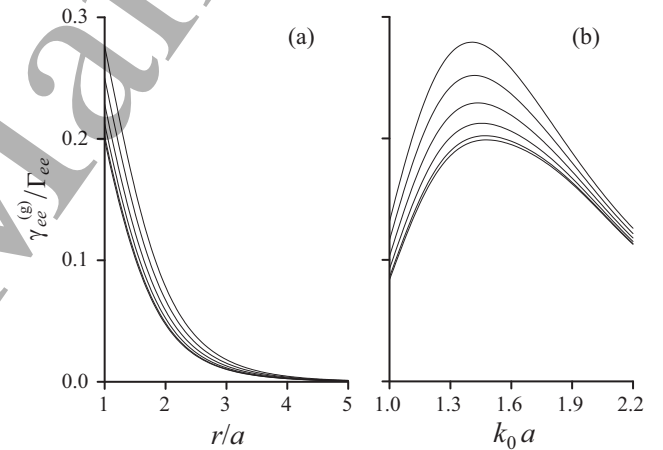
Figure 7. Channeling efficiency of spontaneous emission into guided modes for various magnetic sublevels, as functions of (a) the atomic position and (b) the fiber radius. In (a), the nanofiber radius is $a = 200$ nm. In (b), the atom is on the nanofiber surface. Other parameters are as in Fig. 6. Note that the peaks in (b) occur around $k_0 a = 1.45$, which correspond to $a = 200$ nm for the cesium D_2 line. From Fam Le Kien *et al* [31].

In order to get deeper insight into the channeling of spontaneous emission into guided modes, we plot the channeling efficiency η for various magnetic sublevels in Figs. 7(a) and 7(b) as a function of r/a and $k_0 a$, respectively. From Fig. 7(a), it may be seen that, in the close vicinity of the nanofiber surface, the channeling efficiencies into guided modes are substantial, in the range from 0.2 (for $M_e = 0$) to 0.28 (for $M_e = \pm 5$). As the atom-surface separation increases, $\gamma_{ee}^{(\rm g)}/\Gamma_{ee}$ quickly reduces to zero, as expected. From Fig. 7(b) it can be seen that, $\gamma_{ee}^{(\rm g)}/\Gamma_{ee}$ is sensitive to $k_0 a$, reaching a maximum at around $k_0 a = 1.45$.

This size parameter corresponds to a nanofiber radius of about 200 nm. For such a parameter, a significant fraction (up to 28% for $M_e = \pm 5$) of spontaneous emission by the atom can be channeled into guided modes.

We note that the hfs eigenstates of an alkali-metal atom are specified with respect to a quantization axis. Therefore, the decay parameters of a realistic atom depend on the orientation of the magnetic field relative to the fiber axis. The effect of the orientation of the quantization axis on the radiative decay parameters of a cesium atom near a nanofiber has been studied in Ref. [65].

We also note that, when the size parameter V is larger than the cut-off value $V_c \cong 2.405$, the fiber can support not only the fundamental mode HE_{11} but also higher-order modes. Spontaneous emission from an alkali-metal atom into the fundamental and higher-order modes of a vacuum-clad ultrathin optical fiber has recently been investigated [69].

2.2.2. Scattering of guided light by a single atom
We now discuss the scattering of a guided mode field from an atom trapped near to an optical nanofiber as depicted in Fig. 5, following closely the treatment given in Refs. [32] and [70]. We will consider atomic cesium, and specifically its D_2 line at a wavelength of $\lambda_0 = 852$ nm. The atom is assumed to be initially prepared in the ground state $6S_{1/2}$ with a hyperfine level $F = 4$. Probe light in the fiber mode is assumed to be tuned close to the resonance between this ground state and the excited state $6P_{3/2}$ with a hyperfine level $F' = 5$.

For our description of the cesium atom's internal state, we take the z-axis (fiber axis) as the quantization axis, and we assume that the atom is situated on the positive x-axis. We denote the spherical tensor components of the dipole matrix element by $d_{eg}^{(-1)} = (d_x - id_y)/\sqrt{2}$, $d_{eg}^{(0)} = d_z$, and $d_{eg}^{(1)} = -(d_x + id_y)/\sqrt{2}$. Additionally, we denote the spherical tensor components of the field envelope vector $\boldsymbol{\mathcal{E}}$ by $\mathcal{E}_q$ with ($q = 0, \pm 1$). Specifically, we have $\mathcal{E}_{-1} = (\mathcal{E}_x - i\mathcal{E}_y)/\sqrt{2}$, $\mathcal{E}_0 = \mathcal{E}_z$, and $\mathcal{E}_1 = -(\mathcal{E}_x + i\mathcal{E}_y)/\sqrt{2}$. The Rabi frequencies

$$\Omega_{eg} = \frac{1}{\hbar}(\mathbf{d}_{eg} \cdot \boldsymbol{\mathcal{E}}) = \frac{1}{\hbar}\sum_{q=0,\pm 1}(-1)^q d_{eg}^{(q)}\mathcal{E}_{-q} \quad (12)$$

characterize the interaction of the atom and the probe field. The atom is assumed to be prepared in an initial incoherent mixture of Zeeman sublevels $|M\rangle$ of the ground-state hyperfine level F, with the population distributed independently of M. For the regime of stationary probe field $\boldsymbol{\mathcal{E}}$ with the atom in its steady state, the total scattering rate of probe field photons from the atom is given by

$$\mathcal{R} = \sum_{ee'}\Gamma_{ee'}\rho_{e'e} = \mathcal{R}_g + \mathcal{R}_r, \quad (13)$$

where $\mathcal{R}_g = \sum_{ee'}\gamma_{ee'}^{(g)}\rho_{e'e}$ and $\mathcal{R}_r = \sum_{ee'}\gamma_{ee'}^{(r)}\rho_{e'e}$ are the scattering rates into guided and radiation modes respectively. Note that $\Gamma_{ee'}$, $\gamma_{ee'}^{(g)}$ and $\gamma_{ee'}^{(r)}$ denote the decay rates of the excited state manifold which we discussed previously. The population of the excited state manifold is denoted by $\rho_{e'e}$ and can be obtained from the solution of the steady-state density matrix equations [32].

We would like to know scattering rates into the nanofiber guided modes as functions of propagation direction and polarization. We consider the quasilinear polarized HE_{11} guided modes with the index $\xi = x$ and y for the major polarization axis along the x and y directions, respectively. Then, the scattering rate into the fundamental mode with propagation direction $f = \pm$ and a given polarization $\xi = x$ or y is given by

$$\mathcal{R}_{f\xi} = \sum_{ee'}\gamma_{ee'}^{(f\xi)}\rho_{e'e}. \quad (14)$$

Here we have introduced the notation

$$\gamma_{ee'}^{(f\xi)} = 2\pi\sum_g G_{\omega_0 f\xi eg}G_{\omega_0 f\xi e'g}^*. \quad (15)$$

Note that $G_{\omega_0 f\xi eg}$ is the coefficient for the coupling between the resonant guided mode (ω_0, f, ξ) and the atomic transition $|e\rangle \leftrightarrow |g\rangle$. The coupling coefficient has a general expression

$$G_{\omega f\xi eg} = \sqrt{\frac{\omega\beta'}{4\pi\epsilon_0\hbar}}\left(\mathbf{d}_{eg} \cdot \mathbf{e}^{(\omega f\xi)}\right)e^{if\beta z}, \quad (16)$$

in the case of the quasi-linearly polarized HE_{11} mode, where $\mathbf{e}^{(\omega f\xi)}$ is the normalized mode profile function (see Appendix A). Additionally, we introduce the notation

$$\gamma_{ee'}^{(f)} = \sum_{\xi=x,y}\gamma_{ee'}^{(f\xi)} \quad (17)$$

for the the spontaneous emission coefficients into the guided modes with direction f. For simplicity, we make the abbreviations $\gamma_{ee'}^{(fw)} = \gamma_{ee'}^{(+)}$ and $\gamma_{ee'}^{(bw)} = \gamma_{ee'}^{(-)}$, and note that the relation $\gamma_{ee'}^{(g)} = \gamma_{ee'}^{(fw)} + \gamma_{ee'}^{(bw)}$ holds. For the scattering rate into the guided modes with a direction f, we use the notation

$$\mathcal{R}_f = \sum_{\xi=x,y}\mathcal{R}_{f\xi}, \quad (18)$$

with the abbreviations $\mathcal{R}_{fw} = \mathcal{R}_+$ and $\mathcal{R}_{bw} = \mathcal{R}_-$. Note that we can decompose the scattering rate as $\mathcal{R}_g = \mathcal{R}_{fw} + \mathcal{R}_{bw}$. The total output guided mode field is then given by the interference between the input probe field and the forward scattered field, with conservation of energy giving the loss rate

$$\mathcal{R}_{loss} = \mathcal{R}_r + \mathcal{R}_{bw}. \quad (19)$$

The steady state regime density-matrix equations are solved and used to find the coefficients $\eta_{fw} = \hbar\omega\mathcal{R}_{fw}/P_z$ and $\eta_{bw} = \hbar\omega\mathcal{R}_{bw}/P_z$ which give the

efficiency of scattering into forward and backward propagating guided modes, respectively, for a given mode power P_z. More generally, we define the efficiency coefficients for a given propagation direction f and polarization ξ: $\eta_{f\xi} = \hbar\omega\mathcal{R}_{f\xi}/P_z$. For our numerical calculations, we use a fiber radius $a = 250$ nm and a mode power $P_z = 10$ fW, which is much lower than the saturation power of 4.4 pW.

Figures 8 and 9 show the scattering efficiency coefficients as functions of the normalized radial distance r/a for x- and y-polarized probe fields, respectively. Note that a common feature of these results is that, in general (except for η_{fy} in the case of Fig. 8), the scattering efficiency coefficients reduce with increasing radial distance r. This reduction is due to the evanescent-wave profiles of the guided-mode functions outside the fiber, which affect the scattering rates $\mathcal{R}_{f\xi}$ via the Rabi frequencies Ω_{eg} and the spontaneous emission coefficients $\gamma_{ee'}^{(f\xi)}$.
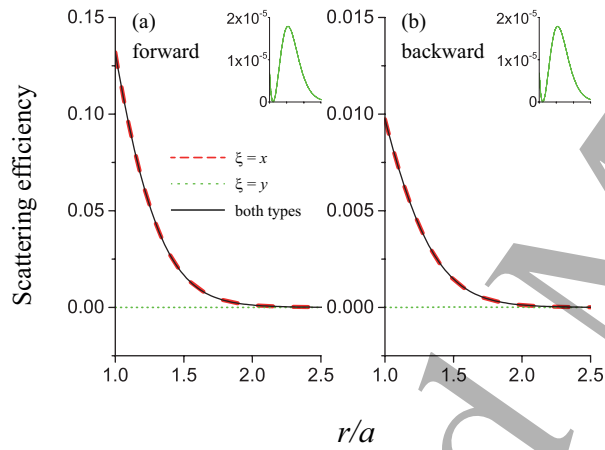

Figure 8. (Color online) Radial-distance dependencies of the scattering efficiency coefficients for quasi x-polarized guided probe field. η_{fw} and η_{bw} for scattering into forward and backward guided modes, respectively, are shown by the solid black lines in parts (a) and (b), respectively, at zero detuning and for the parameters given in the text. $\eta_{f\xi}$ with $\xi = x$ (dashed red lines) and $\xi = y$ (dotted green lines) for the modes with x and y polarizations, respectively, are also shown. From Fam Le Kien and A. Rauschenbeutel [70].

For the case of quasilinear mode polarization along the x-axis, comparison of Figs. 8(a) and (b) show that forward scattering is about an order of magnitude stronger in the forward direction compared with the backward direction. In addition, it may be seen that the main component scattered into both forward and backward propagating modes is the x-polarized component, i.e., the component with the same polarization as the probe field. On the other hand, the scattering efficiency of the y-polarized component (shown in the insets by dotted green lines) is seen to be independent of scattering direction and

is up to four orders of magnitude smaller than the efficiency for the x-polarized component (dashed red lines). The direction-independence of the y-polarized component is due to the vanishing amplitude of the longitudinal component of the quasi y-polarized guided mode at the position on the x axis considered here. We also note that the atypical increase of η_{fy} for r/a between ~ 1.1 to ~ 1.5 due to interference between different atomic transition channels.
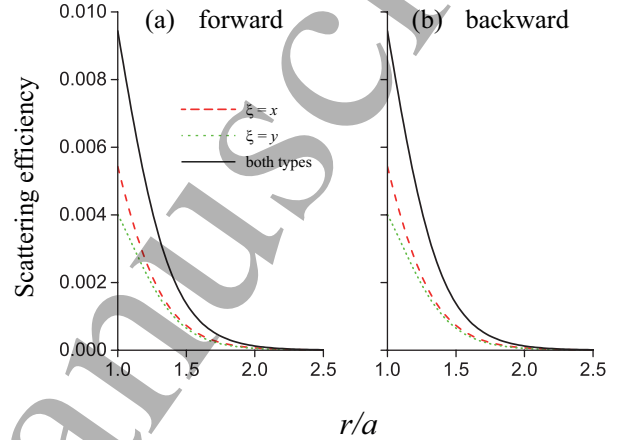
Figure 9. (Color online) Same as Fig. 8 but for the case where the probe field is quasi y-polarized. From Fam Le Kien and A. Rauschenbeutel [70].

The scattering efficiency coefficients for a probe field with quasi y-polarization are shown in Fig. 9. In this case, Figs. 9(a) and (b) are identical, showing that rates for both individual components, $\mathcal{R}_{fx}$ and $\mathcal{R}_{fy}$ and the total rate $\mathcal{R}_f = \mathcal{R}_{fx} + \mathcal{R}_{fy}$ for a given direction f are independent of the scattering direction. This is due to the zero longitudinal component of the probe field for the position considered here. It is interesting to note that both x (dashed red lines) and y (dotted green lines) components are present in the scattered fields, and, furthermore, the x-component is slightly larger even though the input probe field is y-polarized. This arises from the differences in the quasi x- and y-polarized guided modes at the chosen position, along with the properties of the atomic dipole matrix elements and the atomic steady-state density matrix.

2.2.3. Directional spontaneous emission from a two-level atom We will now consider the case of a two-level atom near to a nanofiber in order to gain a better understanding of the forward/backward scattering asymmetry. In this case, the spontaneous emission rate into positive-direction propagating guided modes ($f = +$) and negative-direction propagating guided modes ($f = -$) is given by

$$\gamma^{(f)} = \gamma^{(fx)} + \gamma^{(fy)}, \tag{20}$$

Nanofiber quantum photonics   10

where [31]

$$\gamma^{(f\xi)} = \frac{\omega_0 \beta_0'}{2\epsilon_0 \hbar} |\mathbf{d} \cdot \mathbf{e}^{(\omega_0 f\xi)}|^2 \tag{21}$$

is the rate of spontaneous emission into the guided modes with the propagation direction $f = +, -$ and the polarization $\xi = x, y$. We note that the dipole matrix-element vector $\mathbf{d}$ is, in general, a complex vector. We note that $\gamma^{(f\xi)}$ and, consequently, $\gamma^{(f)}$ depend on the magnitude, the orientation, and the polarization of the dipole matrix-element vector $\mathbf{d}$. Furthermore the rate Γ_f of scattering into the guided modes with a given propagation direction f is related to the corresponding spontaneous emission rate $\gamma^{(f)}$ as $\Gamma_f = \rho_{ee}\gamma^{(f)}$.

To proceed, we will take the atom to be situated on the positive x-axis, with the z-axis being the fiber axis as before. Then, we obtain the expressions for the profile functions

$$\mathbf{e}^{(\omega_0 fx)} = \sqrt{2} \, (i|e_r|, 0, f|e_z|) \tag{22}$$

and

$$\mathbf{e}^{(\omega_0 fy)} = \sqrt{2} \, (0, i|e_\varphi|, 0) \tag{23}$$

in the cases of quasi x- and y-polarized guided modes, respectively (see Appendix, Eqs. (A.21)). It is clear from Eqs. (21) and (23) that the rate $\gamma^{(fy)}$ of spontaneous emission into the guided modes with the y polarization does not depend on the emission direction f. Meanwhile, it follows from Eqs. (21) and (22) that the rate $\gamma^{(fx)}$ of spontaneous emission into the guided modes with the x polarization does not depend on the emission direction f if the dipole components d_z and d_x have the same phase, that is, if the component of the atomic dipole in the zx plane is linearly polarized. However, the rates $\gamma^{(fx)}$ and $\gamma^{(f)}$ may depend on f if both components d_z and d_x are nonzero and have different phases, that is, if there is an ellipticity of the polarization of the atomic dipole matrix-element vector $\mathbf{d}$ in the zx plane.

Let us now consider such a case. In particular, we will consider the case of a circularly polarized atomic dipole in the zx plane, leading to the choice of the y-axis as the natural quantization axis. The quantization coordinate system is $\{x_Q, y_Q, z_Q\}$, where

$$x_Q = z, \qquad y_Q = x, \qquad z_Q = y. \tag{24}$$

In this coordinate system, the dipole matrix element $\mathbf{d}$ of the atom has only a single nonzero spherical tensor component $d_q = -q(d_{x_Q} + iqd_{y_Q})/\sqrt{2}$, where $q = M_e - M_g = \pm 1$ corresponds to the transition type $\sigma_\pm$. An example of such a two-level atom is a cesium atom with the cycling transition between the Zeeman levels $|F' = 5, M' = \pm 5\rangle$ and $|F = 4, M = \pm 4\rangle$ of the excited state $6P_{3/2}$ and the ground state $6S_{1/2}$, respectively. The initial state can be prepared by optical pumping with the use of a circularly polarized field freely propagating along the y direction. In

the Cartesian coordinate system $\{x, y, z\}$, the dipole matrix-element vector is

$$\mathbf{d} = \frac{d_q}{\sqrt{2}}(i, 0, -q). \tag{25}$$

The above expression shows that, in the Cartesian coordinate system $\{x, y, z\}$, the dipole matrix-element vector $\mathbf{d}$ has two nonzero components, d_z and $d_x = -iqd_z$, which are different in phase from each other by $\pi/2$. This is a consequence of the fact that the polarization of the atomic dipole is circular in the zx plane. From Eq. (25), we find

$$\mathbf{d} \cdot \mathbf{e}^{(\omega_0 f\xi)} = \frac{d_q}{\sqrt{2}}(ie_x^{(\omega_0 f\xi)} - qe_z^{(\omega_0 f\xi)}). \tag{26}$$

For the y-polarized guided modes, Eq. (23) yields $e_x^{(\omega_0 fy)} = e_z^{(\omega_0 fy)} = 0$. This leads to $\mathbf{d} \cdot \mathbf{e}^{(\omega_0 fy)} = 0$ and, hence, $\gamma^{(fy)} = 0$. For the x-polarized guided modes, Eq. (22) yields $e_x^{(\omega_0 fx)} = i\sqrt{2}|e_r|$ and $e_z^{(\omega_0 fx)} = f\sqrt{2}|e_z|$. This leads to

$$\mathbf{d} \cdot \mathbf{e}^{(\omega_0 fx)} = -d_q(|e_r| + fq|e_z|). \tag{27}$$

Hence, we find

$$\gamma^{(f)} = \gamma^{(fx)} = \frac{\omega_0 \beta_0' d_q^2}{2\epsilon_0 \hbar}(|e_r| + fq|e_z|)^2. \tag{28}$$

From the above analysis, it is clear that in this case $\gamma^{(f)}$ depends on the emission direction $f = \pm$ and also on the transition type $\sigma_\pm$ characterized by the number $q = M_e - M_g = \pm 1$. Moreover, when we set $f = +$ and $f = -$ in Eq. (28) and then calculate the ratio between the results, we find

$$\left.\frac{\gamma^{(+)}}{\gamma^{(-)}}\right|_{q=1} = \left.\frac{\gamma^{(-)}}{\gamma^{(+)}}\right|_{q=-1} = \left(\frac{|e_r| + |e_z|}{|e_r| - |e_z|}\right)^2. \tag{29}$$

This shows that in general, the spontaneous emission of the two-level atom into the guided modes of the nanofiber may have different rates for different directions $f = \pm$. We emphasize that the occurrence of $\gamma^{(+)} \neq \gamma^{(-)}$ is due to the existence of the longitudinal component e_z of the guided-mode profile function, the existence of the components d_z and d_x of the atomic dipole matrix element, the ellipticity of the polarization of the x-polarized guided mode in the zx plane, and the ellipticity of the polarization of the atomic dipole in the zx plane. We note that the ratio $\gamma^{(+)}/\gamma^{(-)}$ is simply determined by the ratio between the radial and axial components e_r and e_z, respectively, of the guided-mode profile function. In Fig. 10, we plot the dependence of the ratio $\gamma^{(+)}/\gamma^{(-)}$ on the radial position r of the atom. The figure shows that $\gamma^{(+)}/\gamma^{(-)}$ decreases slowly with increasing r and can be as large as about 13.3 for an atom on the fiber surface ($r/a = 1$).
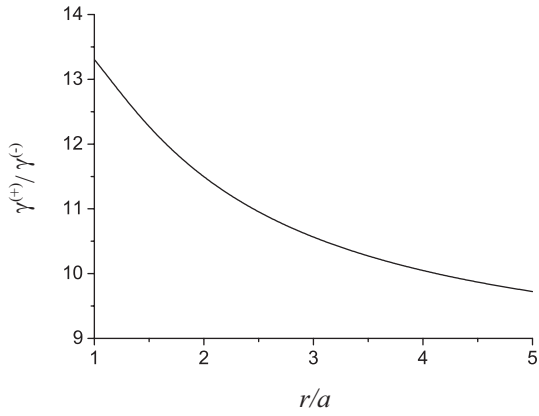
Figure 10. Ratio between the spontaneous emission rates from a two-level atom into the guided modes in the directions $+\hat{\mathbf{z}}$ and $-\hat{\mathbf{z}}$, respectively. The two levels of the atom considered here are $|F' = 5, M' = 5\rangle$ and $|F = 4, M = 4\rangle$ of the D_2 line of atomic cesium with respect to the quantization axis $\hat{\mathbf{z}}_Q = \hat{\mathbf{y}}$. The atom is positioned on the positive side of the x axis. Other parameters are as in Fig. 8. From Fam Le Kien and A. Rauschenbeutel [70].

2.2.4.   Trapping atoms using guided modes of a nanofiber Optical trapping of neutral atoms is one of the crucial techniques for storing and processing quantum information. In particular, manipulation of individual neutral atoms in microscopic dipole traps is a promising approach.   Several techniques have been developed in order to produce optical dipole traps [71] with a microscopic trapping volume. Among these are strongly focused free-space optical traps [72], optical lattices [73], traps based on evanescent light fields [74], and plasmonically enhanced optical trapping potentials [19, 20].

The tight confinement of the nanofiber guided field and the strong intensity gradient of the guided field in the evanescent region surrounding the nanofiber enables optical dipole trapping of atoms at relatively low powers compared to focussed beams in free space. Various trapping schemes have been theoretically formulated and experimentally demonstrated.   In optical dipole trapping, red-detuned (blue-detuned) light far from resonance provides an attractive (repulsive) potential which is proportional to the intensity of the light. The evanescent tail of the HE_{11} fundamental guided field provides a steep intensity gradient but there is no local minimum to create a trap.

Balykin *et al* proposed a method to use a single red-detuned guided mode field to balance the centrifugal force experienced by an atom with a velocity component perpendicular to the nanofiber axis [75].   Another way to produce a local minimum is to employ a two color trap in which red-detuned and blue-detuned light fields in the nanofiber fundamental mode create a trapping minimum close to the nanofiber
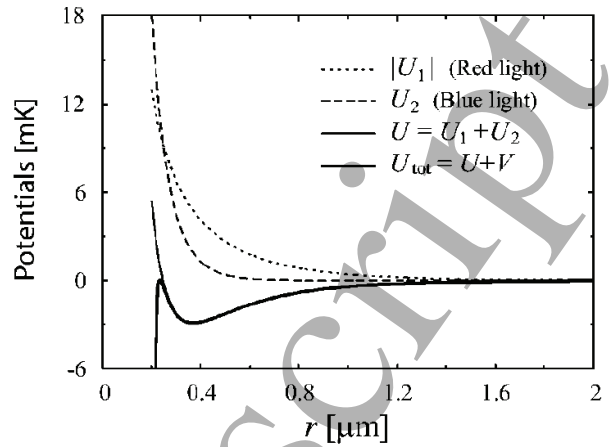

Figure 11.   The total trapping potential U_{tot} and its constituents, for a two-color trap of a ground-state cesium atom outside a nanofiber with two circularly polarized input light fields.   The absolute value of the red-detuned component U_1 (dotted line) subtracts from the blue-detuned component U_2 (dashed line) to give the net optical potential U (thin solid line). This is modified by the van der Waals surface interaction, giving the total potential U_{tot} (thick solid line). The radius of the fiber is $a = 200$ nm. The laser wavelengths are $\lambda_1 = 1.06$ μm and $\lambda_2 = 700$ nm. The laser powers are $P_1 = 30$ mW and $P_2 = 29$ mW. From Ref. [29].

surface due to the differing evanescent decay lengths of the two wavelengths of light. In particular, due to the presence of the attractive van der Waals force near the fiber surface, blue-detuned light is essential to keep the atoms away from the fiber surface. Kien *et al* have proposed and investigated an atom trap and waveguide using a two-color evanescent light field around a nanofiber [29]. It was shown that by choosing a proper power ratio for the two colors, a stable trapping potential can be realized around the nanofiber in the form of a cylindrical shell or two straight lines parallel to the fiber axis in the cases of circularly and linearly polarized input light, respectively.

A detailed theoretical formulation for the trapping potential using the guided modes of a nanofiber is presented in Appendix C. The total atomic trap potential U_{tot} consists of the optical potential U and the surface-induced potential V, that is,

$$U_{\mathrm{tot}} = U + V. \tag{30}$$

The time-averaged optical potential of the induced dipole moment $\mathbf{d}$ interacting with the driving electric field $\mathbf{E}$ is given by

$$U = -\frac{1}{2}\overline{\mathbf{d}(t) \cdot \mathbf{E}(t)} = -\frac{1}{4}|\mathcal{E}|^2 \mathrm{Re}[\alpha] \tag{31}$$

where $|\mathcal{E}|^2$ is proportional to the intensity of the optical field and $\mathrm{Re}[\alpha]$ is the real part of the complex polarizability of the atom.

A typical calculated trapping potential is shown in Fig. 11. The ground-state cesium atom has two strong

Nanofiber quantum photonics   12

transitions, at 852 nm (D_2 line) and 894 nm (D_1 line). To trap the atom red- and blue-detuned light fields with wavelengths $\lambda_1 = 1.06$ μm and $\lambda_2 = 700$ nm, respectively, are used. It may be seen that a trapping minimum is formed within 200 nm of the fiber surface with a trap depth of few mK. The two-color guided mode trap has been experimentally demonstrated first by Vetsch *et al* [37] and then followed by many groups [38, 76, 77, 78, 54, 47].
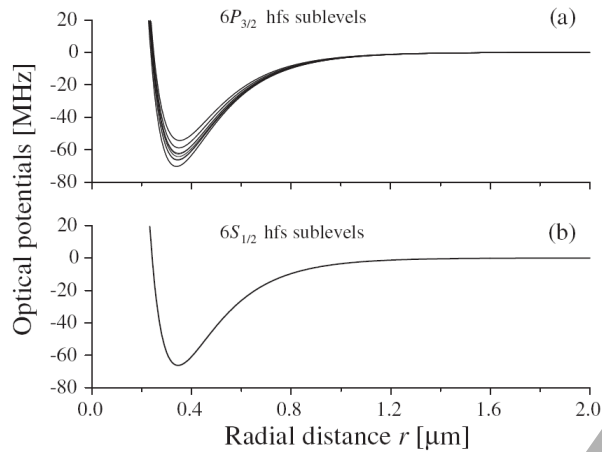

Figure 12. The light shifts (optical potentials) of cesium atoms in a two-color evanescent field around a nanofiber. The panels (a) and (b) show the potentials for the excited-state manifold $6P_{3/2}$ and the ground-state manifold $6S_{1/2}$, respectively. The radius of the fiber is $a = 200$ nm. The two laser beams are tuned to the wavelengths $\lambda_1 = \lambda_R = 934.5$ nm and $\lambda_2 = \lambda_B = 685.5$ nm, with the powers $P_1 = 11.5$ mW and $P_2 = 48.5$ mW, respectively. Only the results for the transitions involving the excited-state sublevels that are split from $F = 5$ are shown. From Ref. [30].

A major issue in these types of microscopic traps is that the excited state can experience an ac Stark shift of different sign and magnitude compared with the ground state, leading to change in the resonant frequency of the atoms in the dipole trap. Therefore, due to the high spatial gradient of the trapping fields, the resonant frequency of trapped atoms can vary substantially with their position in the trap, leading to dephasing and creating an obstacle for various quantum optics experiments.

Kien *et al* have investigated the light shifts, of the ground and excited states of atomic cesium in a two-color evanescent field around a nanofiber [30]. They showed that by tuning one trapping field to around 934.5 nm in wavelength (central red-detuned magic wavelength) and the other field to around 685.5 nm in wavelength (central blue-detuned magic wavelength), the light shifts of the $6S_{1/2}$ to $6P_{3/2}$ transitions can be minimized. The simultaneous use of the red- and blue-detuned magic wavelengths can allow state-insensitive two-color trapping and guiding of cesium atoms along the nanofiber. Figure 12

shows the optical potentials of cesium atoms in a two-color magic-wavelength trap around a nanofiber. One can see that the excited- and ground-state optical potentials have similar shapes. The deep minima for the potentials are located close to each other in space, indicating the possibility of state-insensitive two-color trapping of cesium atoms around the nanofiber. Such a state-independent trapping scheme can allow the simultaneous operation of trapping and probing. A state-insensitive and compensated two-color nanofiber trap was first demonstrated by Goban *et al* [38, 76].

3. Fabrication and characterization of nanofibers

Techniques for the fabrication of optical nanofibers are now well known and used in many laboratories throughout the world. The essential method is to heat a standard optical fiber to soften the silica sufficiently that it may be pulled and tapered [24, 25, 79, 80, 81, 82, 83, 84, 85]. The first creation of subwavelength diameter fibers for guiding of light is typically attributed to Tong. *et al* [24]. Other important early efforts include that of Brambilla *et al* and Clohessy *et al* in creating low-loss, sub-micron tapers [79, 86]. Additionally, Sumetsky *et al* produced sub-micron fiber tapers in order to determine how thin a silica fiber could be and still guide light [87, 88].

In this section we will briefly review the fabrication and measurement of optical nanofibers, with a focus on the widely used "flame brush" technique as well as recent methods to characterize the shape and dimensions of nanofiber tapers.

3.1. Experimental fiber tapering

A schematic of a tapered fiber is shown in Fig. 13(a). If a silica fiber with initial radius R_0 is heated to its softening point with a constant hot-zone of length L and then pulled through a distance $2z_0$, a uniform waist region of reduced radius $R(z_0)$ and length L is formed at the center which tapers up smoothly on either side to the original radius R_0. Assuming that silica which passes outside the hot-zone quickly hardens, volume conservation allows us to derive the shape of the tapered region which is found to be exponential, i.e. [89]

$$R(z) = R_0 \exp(-z/L). \tag{32}$$

If the hot-zone can be varied, it may be shown that essentially arbitrary (although monotonically decreasing) taper shapes can be realized [89]. Commonly used taper shapes include exponential tapers - useful for creating tapers which reduce to sub-micron dimensions over a short distance, and linear tapers, which
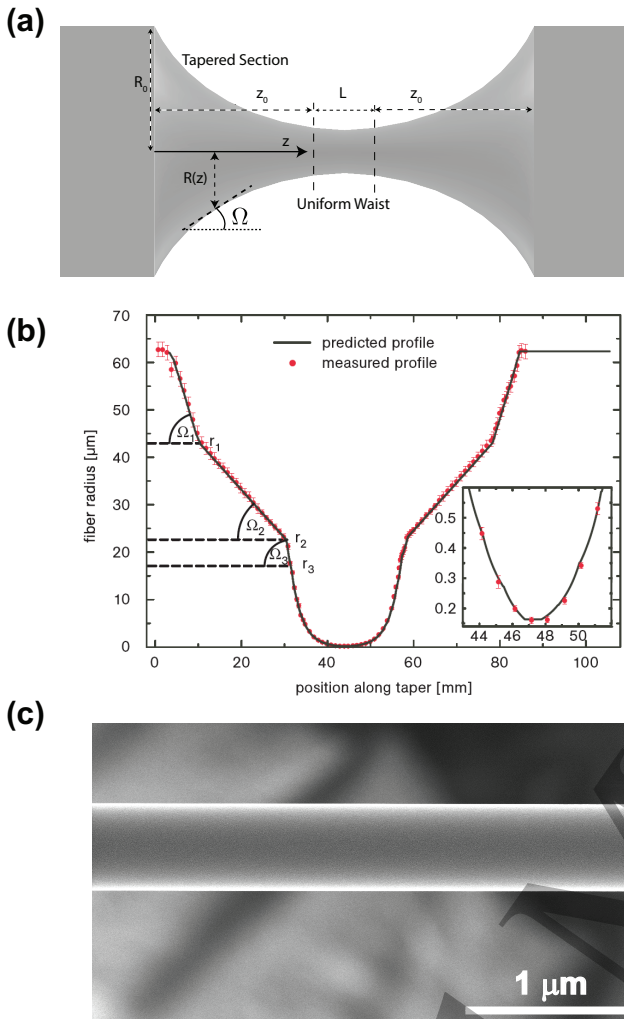
Figure 13. (a) Depiction of a fiber taper showing the definition of the local fiber taper angle Ω. (b) Example of a measured fiber taper profile from [80]. In this example, three different hot-zone lengths were used. (c) SEM image of a typical nanofiber sample with a diameter of around 530 nm. ((b) is included with permission from [80].)

can be useful for producing adiabatic tapers for multiple modes [90]. Measured and theoretically predicted diameters for a multi-stage, linear taper produced by Stiebeiner *et al* are shown in Fig. 13(b) [80]. The scanning electron microscope (SEM) image of a typical nanofiber sample with a diameter of around 530 nm is shown in Fig. 13(c).

Experimentally, the most common method to realize tapering with adjustable hot-zone length is by sweeping a clean flame back and forth along the fiber axis [83]. The effective hot-zone length is set by the width of the sweep, allowing the tapering angle to be adjusted. Other methods to create a hot-zone include ceramic heaters [85] and CO_2 lasers [91]. A broad discussion of such methods may be found in Ref. [83].

3.2. *Guided light transmission and the adiabatic criterion*

We now consider how a fiber taper of the type described above transmits the fundamental mode. Adiabatic mode transformation is a commonly used technique to achieve high transmission in nonuniform optical waveguides [93]. The key idea is to change the fiber diameter slowly along the propagation direction of the light such that all the optical power remains in a single eigenmode, while the coupling to other modes is suppressed. However, from the viewpoint of practical application a finite length of the taper is essential. This leads to the adiabatic criterion for the tapering angle.

When two orthogonal guided modes with wave number β_1 and β_2 propagate in an optical fiber, their fields beat with a spatial period $z_B = 2\pi/|\beta_1 - \beta_2|$. For the purposes of the present analysis, we will assume that β_1 is the propagation constant of the fundamental mode HE_{11} and that β_2 is the propagation constant of the next higher order mode with the same symmetry as the fundamental mode. In order to achieve adiabatic mode transfer, the characteristic taper length $z_T = R/\tan(\Omega)$ should be larger than z_B, where R and Ω are the local radius and taper angle (see Fig. 13(a)), respectively. From this intuitive length scale argument one can find that the criterion for adiabatic tapering of an optical fiber is given by

$$|\Omega| \ll \frac{R}{z_B} = \frac{R|\beta_1 - \beta_2|}{2\pi}. \tag{33}$$

The first presentation of this criterion is attributed to Stewart and Love [92] and is discussed in more detail in Synder and Love's textbook [93] where it is referred to as the *slowness condition*. In the same textbook, a more rigorous treatment is given in terms of coupled mode theory. Nonetheless, the heuristic adiabatic criterion Eq. 33 is typically used in the tapered fiber community and produces excellent results in terms of allowing the design and realization of high quality tapered nanofibers with transmission of $> 99\%$ [81, 82, 84].

As shown in Fig. 14(a), the value of $n_{\mathrm{eff}} = \beta/k$ for each mode depends on the radius of the fiber. In this case, the maximum angle satisfying the adiabatic criterion will also change with fiber radius, as shown in Fig. 14(b). It is important to note that in the region where the core begins to vanish, the fiber mode transitions from a core-guided mode with weak confinement due to the silica clad, to a clad guided mode strongly confined by the silica-vacuum interface (vacuum clad fiber). This transition region, known as the *core-mode cutoff*, is the most critical region for adiabatic tapers, and the region where the adiabatic tapering angle takes its smallest value. As the vacuum clad fiber becomes thinner, the fiber approaches the single-mode condition, and the adiabatic taper angle
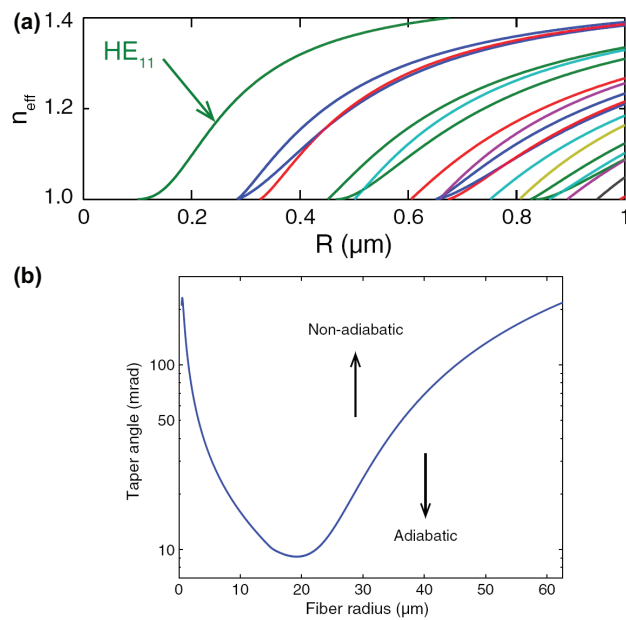
Figure 14. (a) Effective refractive index of fiber guided modes as a function of fiber radius R. (b) Adiabatic taper angle as a function of fiber radius. The calculations are performed for an commercial optical fiber (SM800) from Fibercore at a wavelength of 780 nm. Figures are adapted from [82] with permission.)

rapidly becomes larger as the amplitude of the higher order modes vanishes.

We note that the adiabatic criterion constrains the local taper angle, but *not* its rate of change. Therefore, the taper angle may change suddenly without causing loss, so long as the new angle also satisfies the adiabatic criterion. This fact conveniently allows the fabrication of high transmission fiber tapers using hot-zones which change discontinuously over a number of stages. For example, a relatively long hot-zone length can be used to taper through the core-mode cutoff region, after which smaller hot-zones can be used to quickly reduce the taper size without inducing losses. Although fabrication of an optimally short adiabatic taper requires a continuously varying hot-zone length [84, 89], performing the taper in several stages offers a simple strategy which is often sufficient for most purposes.

3.3. Nanofiber diameter measurement

Optical nanofibers are typically characterized by their length and their radius. Although their length is well defined by the sweep length in the fabrication process, it is often necessary to measure the radius precisely in order for reliable comparison with theory to be made. Measurement in a scanning electron microscope allows simple determination of the nanofiber radius, but it is often a destructive measurement, requiring the mounting of the nanofiber in a special apparatus, and
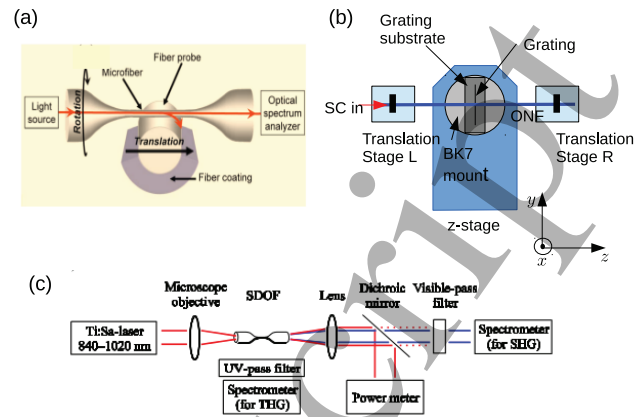

Figure 15. Methods of non-destructive nanofiber diameter measurement. (a) (Adapted with permission from [95].) Experimental setup for probing of nanofiber diameter with a microfiber. In this case, measurement of whispering gallery modes was utilized to estimate the nanofiber diameter. (b) (Adapted with permission from [97].) Experimental setup for measurement of nanofiber diameter using a composite photonic crystal cavity. SC, ONF and SA stand for super continuum source, optical nanofiber and spectrum analyzer respectively. (c) (Adapted with permission from [100].) Experimental setup for measurement of nanofiber diameter using harmonic generation.

relatively high probability of exposing the nanofiber to contaminants during the mounting process.

For the above reasons, *in situ* methods to optically measure the nanofiber radii have been developed in recent years. Below we briefly summarize these methods and compare their merits and demerits.

One of the first optical methods for probing fiber shape at the nano-scale was by Birks and co-workers [94]. Here, the use of the whispering gallery modes (WGMs) of the tapered fiber cross section for the fiber under measurement were coupled to using a second fiber taper (see Fig. 15(a)). It was shown that this allowed sensitive determination of the taper diameter to 1 part in 10,000. Sumetsky and co-workers used related WGM methods to probe the diameter of microfibers and nanofibers with angstrom levels of accuracy [95, 96].

Another method which used a resonator to determine the diameter of a nanofiber was that of Keloth *et al* [97]. In this case, the resonator was formed by bringing a nanostructured grating with a central defect region into optical contact with a nanofiber creating a defect mode cavity for the nanofiber fundamental mode (see Fig. 15(b)). Because the effective index modulation seen by the mode depends sensitively on the nanofiber diameter, the resonance wavelength of the composite cavity has the same sensitive dependence, allowing a one-to-one correspondence between cavity resonance wavelength and nanofiber diameter to be determined. This method reaches nanometer sensitivity, and requires no

post-processing of data since the nanofiber diameter may simply be read off from the cavity resonance wavelength once an initial calibration has been performed.

Madsen *et al* used a method which involved bringing the nanofiber to be measured into contact with another probe fiber taper [98], experimentally similar to Refs. [94, 95, 96]. However, in the case of Madsen *et al*, transmission through the nanofiber under measurement was recorded as light was scattered by the measuring fiber taper. Because the drop in transmission depends on the nanofiber diameter at the point where the measuring taper touches it, the nanofiber diameter may be calculated from the transmission drop. With a similar experimental setup, Fatemi *et al* analyzed the light coupled from a nanofiber taper into a microfiber probe taper analyzing the transmission into the probe fiber and using detailed analysis of intermodal beating to achieve sub angstrom accuracy in their diameter measurements of the nanofiber [99].

Other methods rather different to those described above have also been published recently. Wiedmann *et al* used second and third harmonic generation in the nanofiber region to sensitively estimate the nanofiber diameter [100] (see Fig. 15(c)). The sensitivity to nanofiber diameter in this case resulted from the phase matching required for harmonic generation which requires that the fundamental wavelength and the generated harmonic wavelength both experience the same effective refractive index - a condition which is only satisfied at a certain fiber diameter. Also recently, Xu *et al* demonstrated a real-time monitoring of the micro/nanofiber waist diameter by measuring the transmission drops caused due to the cutoffs of higher order modes [101]. Most recently, Lai *et al* used Rayleigh backscattering of light due to intrinsic roughness of the nanofiber surface combined with a detailed backscattering model to estimate the radius of fiber tapers [102]. These methods have the advantage that they do not require bringing the nanofiber into contact with another object. However, they also require detailed analysis in terms of theoretical modelling and data processing.

As tapered fibers, become increasingly used in different fields, non-destructive measurement methods will become increasing important. As reviewed in this subsection, a range of methods now exist for in-situ measurement of tapered fiber diameter, with most methods having sufficient accuracy (of order a few percent or better) to make them competitive with scanning electron microscope methods.

4. Interfacing neutral atoms

In this section, we review the experimental demonstrations for interfacing laser-cooled atoms with nanofiber guided modes. This includes spectroscopy and photon correlation measurement of atomic fluorescence coupled into the nanofiber guided modes, trapping atoms using nanofiber guided modes, scattering of the guided field by atoms under various settings leading to Bragg reflection and non-reciprocal light transmission and EIT and photon storage experiments.

4.1. Efficient channeling of atomic emission into guided modes
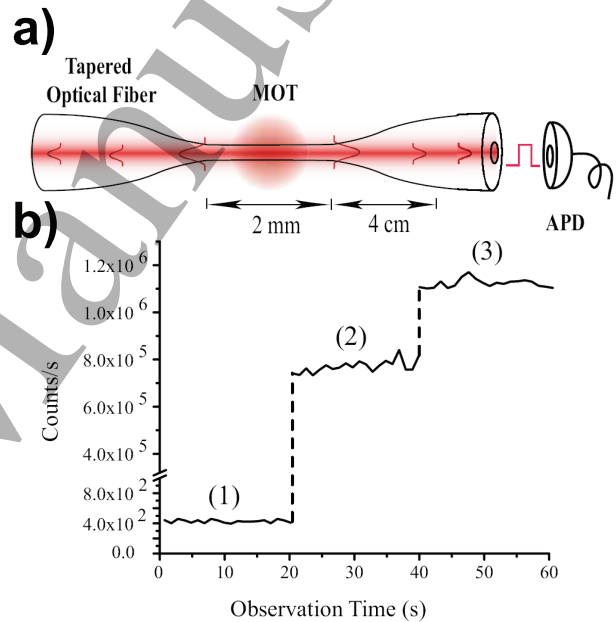
Figure 16. (Color online) (a) Schematic diagram of the experiment. Optical nanofiber is located at the waist of a tapered optical fiber. The laser cooled atoms in a MOT is overlapped with the nanofiber. APD denotes avalanche photodiode. (b)Photon counts measured through the optical nanofiber under three different conditions; (1) the MOT laser beams and B-fields are switched off, (2) the MOT laser beams are switched on, and (3) the MOT laser beams and B-fields are switched on. From Ref. [33].

As discussed in Section 2, the spontaneous emission of atoms can be strongly modified around a nanofiber and a significant amount of atomic fluorescence can be coupled into the guided modes of the nanofiber [31, 64]. The coupling efficiency depends on the fiber diameter and the position of atoms relative to the fiber surface. The optimum coupling efficiency can be realized for a condition of $k_0 a = 1.45$, where k_0 is the free-space propagation constant and a is the radius of the nanofiber. This corresponds to a fiber diameter of 400 nm for the D2-transition of Cs-atoms.

Nanofiber quantum photonics   16

Under this condition a total coupling efficiency of 22% can be realized close to the nanofiber surface. This corresponds to 11% coupling into either direction of the nanofiber guided modes. This opens the possibility to detect few atom fluorescence through the fiber guided modes. The coupling efficiency decreases exponentially with atom-fiber separation. In particular, the total coupling efficiency decreases to 6% at one radius away from the fiber surface. In order to realize an interaction time longer than the atomic spontaneous emission lifetime of 30 ns, laser cooled atoms are typically used.

4.1.1. Spectroscopy of laser-cooled atoms Nayak *et al* have demonstrated coupling of atomic fluorescence into nanofiber guided modes and spectroscopy of a small number of laser cooled atoms in the vicinity of the surface of a nanofiber [33]. A brief schematic of the experiment is shown in Fig. 16(a). The nanofiber was located at the waist of a tapered single-mode optical fiber. A cloud of laser-cooled Cs-atoms in a magneto optical trap (MOT) was overlapped with the nanofiber and the fluorescence of the atoms around the nanofiber was measured at the end of the tapered fiber using an avalanche photodiode. The diameter of the nanofiber was 400 nm over a length of 2 mm and the transmission of the tapered fiber was 87% which was further reduced to 40% after installation. The number density of the MOT was 2×10^{10} atoms/cm^3 and the temperature of the atom cloud was 200 μK. The MOT cloud was overlapped with the nanofiber by using an offset B-field in three perpendicular directions while observing the MOT and fiber position outside the chamber using CCD cameras in two orthogonal directions. After overlapping the MOT with the nanofiber, the MOT density was reduced by 3 times and the cloud temperature increased to 400 μK. It is interesting to note that the MOT (400 μK) and the nanofiber (300 K) had temperatures which differed by six orders of magnitude and yet were still able to co-exist.

After overlapping the MOT with the nanofiber, the atom fluorescence was readily observed through the nanofiber guided modes. Typical photon count measurements made through the nanofiber are plotted in Fig. 16(b). The photon counts are plotted for three conditions: (1) both MOT laser beams and B-fields are switched off, (2) MOT laser beams are switched on, and (3) both MOT laser beams and B-fields are switched on. A fluorescence photon count rate of 3×10^5 counts/s was observed from MOT atoms above a scattering background of 8×10^5 counts/s from the MOT beams. Assuming an effective observation region of 200 nm around the nanofiber, from the MOT dimensions and density, they estimated an effective atom number of 5 in the observation region. Assuming an average

coupling efficiency of 6% they estimated an observable fluorescence photon count rate of 6×10^5 counts/s which reasonably agreed with the observed value.

Morrissey *et al* have used a similar technique to characterize the MOT cloud [103]. They measured the MOT size and shape by monitoring the MOT fluorescence through the nanofiber guided modes. They also investigated the loading rate and lifetime of the MOT. Russell *et al* implemented such a technique to measure the temperature of the atom cloud. They induced an oscillation of the MOT cloud by modulating the magnetic field and then compared the frequency response of the modulation of the cloud position [104] monitored by measuring the fluorescence through the nanofiber. From this measurement they could estimate the cloud temperature both above and below the Doppler limit. Russell *et al* have also performed release - recapture temperature measurements of laser-cooled atoms using an optical nanofiber in a MOT [105].
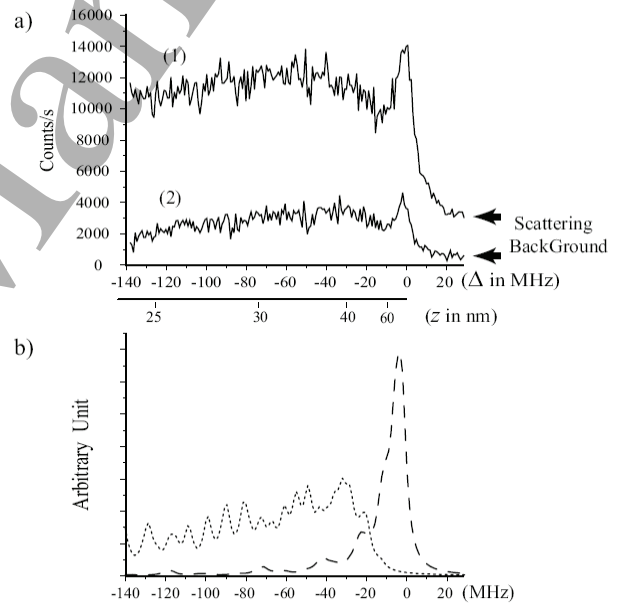
Figure 17.   (a) Excitation spectra of the laser cooled atoms measured through the nanofiber guided modes for two excitation intensities; (1) 3.2 mW/cm^2, and (2) 0.32 mW/cm^2. The detuning Δ is measured relative to atomic resonance. The detuning axis is also represented as the atom-surface separation z, which is calibrated assuming vdW interaction. (b) Theoretically calculated spectra for the photoassociative transitions (dashed curve) and the bound to bound transitions (dotted curve). From Ref. [33].

In order to eliminate the scattering background from the MOT beam and to investigate the laser induced fluorescence spectrum of atoms around the nanofiber, Nayak *et al* implemented a fluorescence measurement scheme using a probe beam [33]. In this measurement scheme, the MOT beams were switched

off periodically for 10 μs in every 200 μs. During the dark period of 10 μs the fluoresecence measurements were performed by exciting the atoms using a probe beam introduced perpendicular to the nanofiber in a standing wave configuration. By scanning the probe beam frequency across the resonance of $6S_{1/2}, F = 4 \rightarrow 6P_{3/2}, F' = 5$ transition, the fluorescence excitation spectra of atoms were measured through the nanofiber guided modes [33]. The observed spectra are displayed in Fig. 17(a) for two probe intensities. The observed line shape is drastically different from the usual atomic line shape. The spectrum shows a long tail in the red detuned side and consists of two peaks. One peak is almost on the atomic resonance and shows a small red tail. The other peak is located around a detuning of Δ =-30$\sim$-50 MHz and shows a long red tail up to Δ=-140 MHz.

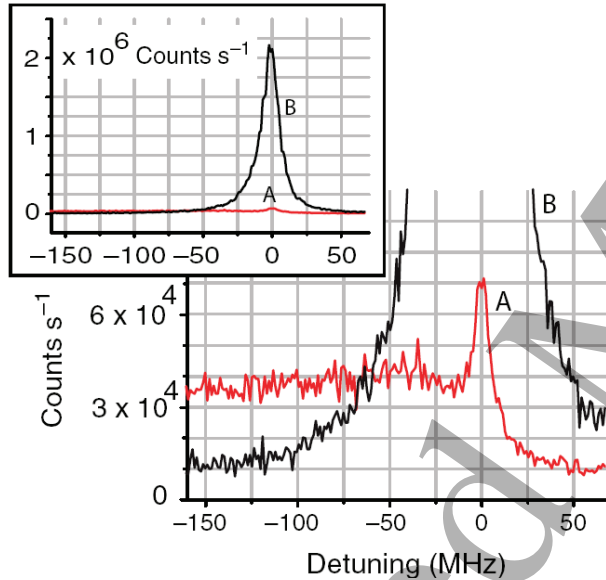**Figure 18.** (Color online) Fluorescence excitation spectra of laser cooled atoms, measured through the nanofiber guided modes for the closed-cycle transition, $6S_{1/2}, F = 4 \rightarrow 6P_{3/2}, F' = 5$. The detuning is measured with respect to the atomic resonance. Traces A and B denote the spectra measured before and after the violet laser irradiation, respectively. From Ref. [35].

Regarding the photon counts, the signal-to-noise ratio was greatly improved by using this method. At resonance a maximum fluorescence count rate of 1.2×10^4 counts/s was observed above a scattering background of 2.5×10^3 counts/s. From the scattering counts due to the probe beam they estimated a scattering probability of 3.7×10^{-8}. However, the fluorescence count rate was also reduced by 20 times compared to the direct observation of MOT fluorescence. This was attributed to loss of atoms in the observation region due to adsorption of atoms on the nanofiber surface.

The observed line shape was attributed to the van der Waals (vdW) interaction between the Cs-atom and the nanofiber surface. Due to the interaction with the surface, the atomic resonance can be red-shifted by $\Delta \nu_{vdW} \approx \nu/(k_0 z)^3$, where z is the distance of atom from the surface. As shown in Fig. 17(a), from the above relation, they calibrated the detuning axis as the atom position from the surface, using a parameter $\nu \approx 0.8$ MHz for Cs-atom and glass surface.

The spectrum was further investigated by calculating the eigenstates of the center-of-mass motion of the atom in the close vicinity of the nanofiber. The details of the calculations are reported in Ref. [106, 107]. The eigenstates are essentially analogous to molecular vibrational states where the molecule consists of the nanofiber and the Cs-atom. Simulations were carried out for two types of transitions. One is for the transitions from free ground atomic states to the bound vibrational states of the excited vdW potential (photoassociative transition) as shown by dashed curve in Fig. 17(b). The other is for transitions from bound ground vibrational states to bound excited vibrational states (bound to bound transition) as shown by dashed curve in Fig. 17(b). Thus they assigned the observed red shaded peak on the atomic line to a photoassociation process and the other broad spectrum to the bound-to-bound vibrational transitions for atoms in the vdW potential.

In their subsequent publications Nayak *et al* reported a dramatic change in the excitation spectrum after irradiating the nanofiber with a violet laser of wavelength 407 nm [35, 108]. The measured spectra are shown in Fig. 18. The trace A denotes the spectrum measured before irradiation by the violet laser and is similar to the one discussed in Fig. 17. Trace B denotes the spectrum measured after irradiation by the violet laser. The irradiation condition was as follows: the nanofiber region was irradiated with 150 mW/cm² intensity violet laser while the MOT was overlapped on the nanofiber and the spectrum was measured after switching off the violet laser. A dramatic change in the spectrum may clearly be seen. The broad spectrum in the red detuned side disappeared and the sharp peak near resonance was enhanced by 30 times. Although the spectrum was still found to be slightly asymmetric, it became narrower similar to the spectrum of an atom in free space and the FWHM was measured to be 15 MHz.

Although the exact mechanism of the effect due to the violet laser was not conclusively determined, it was understood that the violet laser modified the surface of the nanofiber in such a way that atoms were far less likely to fall into the surface potential. As a result the red side tail due to the bound to
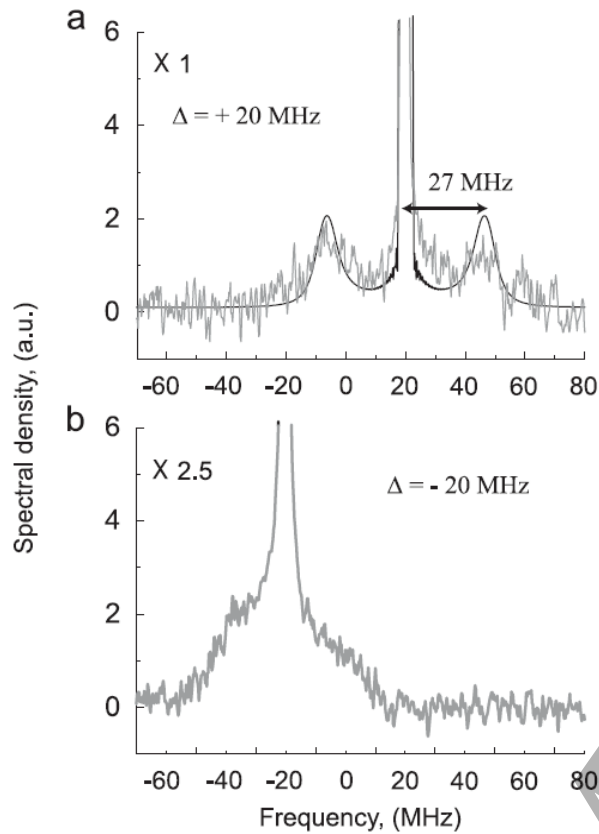
Nanofiber quantum photonics   18

Figure 19. Emission spectra (gray curves) of laser cooled atoms measured through the nanofiber guided modes. The spectra are derived from the Fourier transform of the photon correlation signals for two different detunings of the excitation laser frequency, (a) $\Delta = +20$ MHz and (b) $\Delta = -20$ MHz. The resolution of this measurement is 250 kHz. The frequency axes denote the detuning from the atomic resonance $6S_{1/2}, F = 4 \rightarrow 6P_{3/2}, F' = 5$. The black curve in (a) is the theoretical fit. From Ref. [108].

bound transition was strongly suppressed and the atoms around the nanofiber behaved as free atoms. This was further evident from the observed single atom behavior in photon correlation experiments (discussed in subsubsection 4.2.2) [35]. Single atom behavior was observed only under the same conditions as that which give trace B in Fig. 18. In additional experiments, Das *et al* have measured the fluorescence emission spectrum under the same condition. They employed a combined heterodyne and photon correlation technique to measure the fluorescence emission spectrum of atoms around the nanofiber. Under the same conditions which gave trace B in Fig. 18, they observed clear Mollow triplet-like behavior [109].

Further details of the effect of a violet laser irradiation on the nanofiber-MOT system were reported in Ref. [108]. It was found that the violet laser irradiation was effective only in the presence of the MOT.

This suggested that the photoionization of the MOT atoms modifies the nanofiber surface. After switching off the violet laser the spectrum gradually changed from a condition similar to that seen in trace B of Fig. 18. The red tail gradually increased and finally settled to a condition similar to that seen in trace A of Fig. 18. The rate of change was found to be proportional to the background atom density and did not depend on whether the MOT was overlapped with nanofiber. Therefore, it was understood that hot atoms from the background gas stick to the nanofiber surface, modifying the surface condition. The fluorescence emission spectrum under an intermediate condition was also measured to check for free and bound atom behaviors. Free and bound atoms were excited by choosing a blue and red detuned excitation, respectively. Figure 19(a) and (b) shows the fluorescence emission spectrum measured for an excitation detuning of $\Delta = +20$ MHz and $\Delta = -20$ MHz, respectively. As seen in the figure, clear Mollow triplet behavior was observed for an excitation detuning of $\Delta = +20$ MHz indicating free atom like behavior. However the Mollow triplet behavior was completely washed out for the excitation at $\Delta = -20$ MHz. This was taken as evidence for molecular behavior due to formation of atom surface bound states.

Many groups are working on a similar setup where a cloud of laser-cooled atoms is overlapped with the nanofiber. However, there has not been any further study on the topic of atoms sticking to the nanofiber surface. Some groups have reported that the nanofiber transmission drops due to such atom-surface adsorption effects. However, it was reported that transmission could be recovered by heating up the nanofiber by sending around a few μW to a few mW of laser power through the guided modes [110, 111].

4.1.2. Photon statistics and single atom detection Nayak *et al* have demonstrated that single atoms can be detected using an optical nanofiber by measuring the photon correlation of the fluorescence signal measured through the nanofiber guided modes [35]. The fiber guided fluorescence signal was split into two channels using a 3 dB fiber coupler and the photon correlations between the two channels were measured using a time-correlated photon counter. In order to reduce the atom number in the observation region the MOT density was reduced by decreasing the Cs atom dispenser current (I_D) and the excitation laser was shone perpendicular to the nanofiber and focused to $100 \ \mu$m to excite only a small region of the MOT cloud.

Observed photon correlation signals are shown in Fig. 20(a). The figure shows the coincidences of photon events observed in the two channels as a function of the delay time between them. Antibunching of fluorescence photons at zero time-
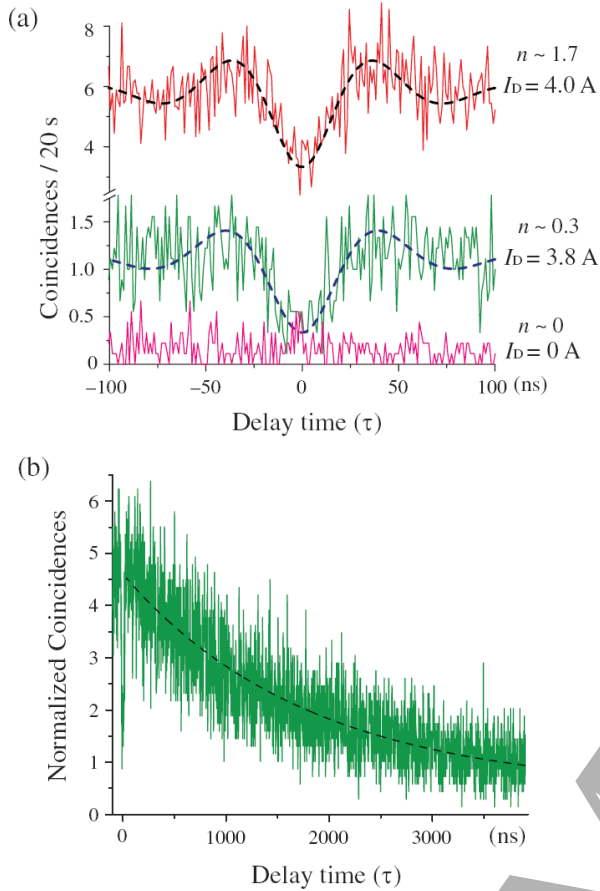
Figure 20. (Color online) (a) Photon correlations of fluorescence signal from the atoms around the nanofiber. τ denotes the delay time between the two channels. The green and red traces show the photon coincidences measured for dispenser currents I_D=3.8 A and 4.0 A, respectively. The pink curve shows the photon coincidences of the background light measured without atoms. The dashed curves denote the theoretically calculated photon coincidences for average atom number $n \simeq 0.3$ and 1.7, respectively. (b) The green curve shows the normalized correlation for longer timescale, measured through the nanofiber, for $I_D = 3.8$ A. The black dashed curve is the exponential fit to the data. From Ref. [35].

delay may clearly be seen, and Rabi oscillation behavior was observed in the wings. They assumed a Poissonian distribution of atom number and hence the observed coincidences could be fitted using the relation, $g_n^{(2)}(\tau) = \frac{1}{n}g^{(2)}(\tau) + 1$, where n is the average atom number, $g_n^{(2)}(\tau)$ and $g^{(2)}(\tau)$ are the normalized correlation functions for n atoms and a single atom, respectively. Fitting the experimental observations using the above relation yielded an average atom number $n = 0.3$ and 1.7 for Cs atom dispenser currents $I_D = 3.8$ A and 4 A, respectively. As shown in Fig. 20(b), the normalized coincidences for longer timescales show an exponential decay with a time constant of 1.8 μs. The observed antibunching of

fluorescence photons in Fig. 20(a) confirms that single atoms can be detected using an optical nanofiber. The observed decay in the correlation at much longer timescales as shown in Fig. 20(b) was attributed to the dwell time of the single atom in the observation volume. Assuming an atom temperature of 100 μK, the dwell time of 1.8 μs corresponds to an atom transit-length of about 200 nm.

Grover *et al* have further investigated the temperature measurement of an atomic cloud around a nanofiber by measuring photon correlations [110]. They measured the temporal width of the photon correlation function due to the atomic transit time and used it to determine the most probable atomic velocity and, hence the temperature. They confirmed the results with standard time-of-flight temperature measurements and trajectory simulations.
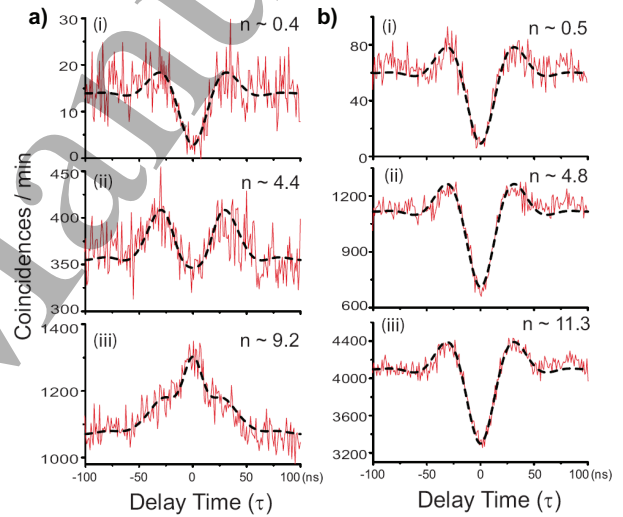
Figure 21. (Color online) Second-order correlations (red solid curves) between fluorescence photons emitted into the nanofiber, when the excitation laser is in a traveling wave configuration. The panels (a) and (b) show the measured correlations for one-end and opposite-end observation schemes, respectively, for three different dispenser currents (i) 3.8 A, (ii) 4.6 A, and (iii) 5.0 A. The black dashed curves show the theoretical fittings and the estimated average atom numbers are denoted by n. From Ref. [36].

Nayak *et al* have further reported a detailed investigation of photon correlations in resonance fluorescence from a few atoms into the guided modes of a nanofiber [36]. Because the nanofiber method inherently implies single-mode observation of atomic fluorescence, the photon correlations must evolve as interplay between first and second order correlations when the atom number varies [112]. They demonstrated that the photon correlations measured at one end of the nanofiber varied from antibunching to bunching with increasing atom number and the photon correlations measured at opposite ends were always

antibunching-like regardless of the number of atoms.

Prior to the experimental demonstration, Kien *et al* reported a detailed theoretical analysis of photon correlations in multi-atom resonance fluorescence measured through a nanofiber [112]. Based on the formalism developed in [112], the second-order correlation function can be written as

$$G_n^{(2)}(\tau) \propto n g^{(2)}(\tau) + n^2 \{\mu_0 + \mu|g^{(1)}(\tau)|^2 \delta_{f_a,f_b}$$
$$+\mu'|g^{(1')}(\tau)|^2 \delta_{f_a,-f_b}\} \tag{34}$$

where n is the average atom number, f_a and f_b denote the observation directions, and τ denotes the delay time. In deriving the above formula, a Poissonian distribution for the atom number in the observation region was assumed. $g^{(2)}(\tau) \propto \langle A_j^\dagger(a)A_j^\dagger(b)A_j(b)A_j(a)\rangle$ is the second-order correlation function for emission from a single atom and has antibunching behaviour at $\tau = 0$, while $g^{(1)}(\tau) \propto \langle A_j^\dagger(a)A_j(a)\rangle$ and $g^{(1')}(\tau) \propto \langle A_j^\dagger(a)A_j^\dagger(b)\rangle$ are the first-order correlation functions which have bunching and antibunching behavior, respectively at $\tau = 0$. Here a and b denote the detector positions and A_j is the operator for the amplitude of the flux of photons emitted from the jth atom into the guided modes. It may be noted that the $g^{(2)}(\tau)$ term scales as n while the other terms scales as n^2. This implies that the first-order correlations will dominate with increasing atom number. Additionally, it should be noted that the $g^{(1)}$ term contributes only to same direction (one-end) correlation, while the $g^{(1')}$ term contributes only to opposite direction (opposite-end) correlation. The correlation function differs from that for freespace observation through the coefficients μ_0, μ, and μ', which are determined by the mode profile function of the guided modes.
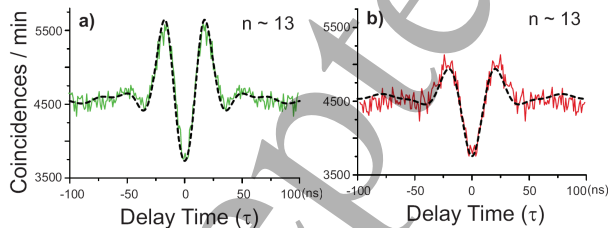

Figure 22. (Color online) The measured correlations between fluorescence photons emitted to opposite-ends of the nanofiber guided modes (solid curves) for two excitation schemes: (a) standing wave and (b) traveling wave. The black dashed curves are the theoretical fittings. The estimated average atom number is $n \sim 13$. From Ref. [36].

The experimentally observed photon correlations for the traveling-wave excitation scheme for the one-end and opposite-end measurements are shown in Fig. 21(a) and (b) respectively. It may be clearly seen that at lower dispenser current, i.e. when the average atom number is less than 1, the two types of observation schemes show clear antibunching of fluorescence photons. However, for higher dispenser current of I_D =5.0 A, the average atom number is $\sim$10 and there is a drastic difference between the two types of correlations. The one-end correlation shows a bunching behavior and the opposite-end correlation shows the antibunching behavior. The bunching behavior in the one-end correlation is well understood from the contribution of the $g^{(1)}$term. The observations are fitted using Eq.(34) yielding the corresponding atom numbers as indicated. The coefficients μ_0 =0.36 and μ=0.22, used for fitting also corresponded well to the theoretical value. However for the opposite-end correlation, the contribution of the $g^{(1')}$ term was not observed and they had to use μ=0 to fit the observations.

Furthermore, it was demonstrated that the excitation geometry is crucial to observe the $g^{(1')}$ term in opposite-end correlations [36]. The opposite-end correlations at higher atom number are compared in Fig. 22(a) and (b), for standing and travelling wave excitation respectively. It can be seen that the wings are higher for the standing-wave scheme than for the traveling-wave scheme. This suggests that the $g^{(1')}$ term in opposite-end correlations can be observed by standing-wave excitation. This was attributed to the effect of the spatial dependence of the phase of the excitation beam and the transverse spread of the atom-position distribution in the observation region around the nanofiber.

4.2. Trapping atoms on a nanofiber

Out of the various proposals for trapping atoms around a nanofiber, only the two-color guided mode trap has been experimentally realized so far, and the method has been widely adapted. A conceptual description, along with a detailed theoretical formulation of the trapping potential, are discussed in Section 2 and Appendix C, respectively.

The experimental realization of two-color nanofiber trapping was first demonstrated by Vetsch *et al* [37, 113, 114]. They trapped cesium atoms using a 500 nm diameter nanofiber. A schematic of the experiment is shown in Fig. 23(a). Blue-detuned light at 780 nm with a power of 25 mW was launched into the fiber in a travelling wave configuration and the red-detuned light at 1064 nm with a power of 2 x 2.2 mW was launched in a standing wave configuration to create a linear array of trapping sites on the nanofiber. In order to achieve maximum azimuthal confinement the states of polarization of the dipole laser beams at the nanofiber waist were aligned perpendicular to each other. The state of polarization was verified by ob-
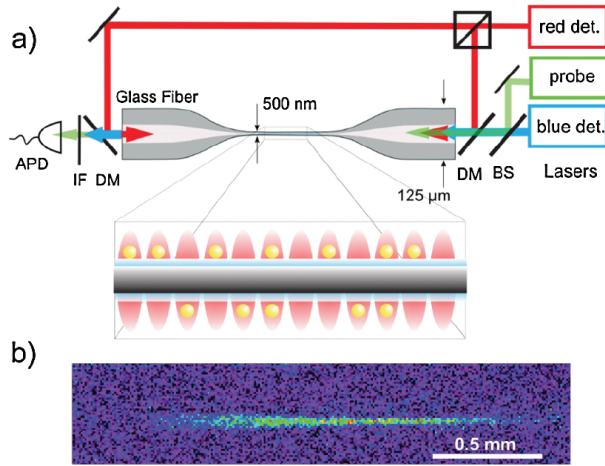
Figure 23. (Color online) (a) Schematic diagram of the experimental setup for the two-color nanofiber trap. The blue- and red-detuned lasers used for creating the trapping potential are launched into the tapered fiber in traveling and standing wave configurations, respectively. A weak resonant laser was used for probing the atoms via the evanescent field. (b) The fluorescence image of the trapped atomic ensemble. From Ref. [37].

serving the angular distribution of the Rayleigh scattered light from the nanofiber perpendicular to its axis. Cesium atoms were first collected and laser-cooled in a MOT overlapped with the nanofiber and then the nanofiber trap was loaded during an optical molasses phase. A fluorescence image of the trapped atoms is shown in Fig. 23(b).

The trapped atoms were probed by measuring the absorption spectrum of weak probe light launched into the fiber. A typical absorption spectrum is shown in Fig. 24(a). A dramatic increase in the optical depth (OD) due to the trapping of atoms may readily be seen. Fitting yielded an OD of 13(2) for a detuning of 13 MHz and FWHM of 20 MHz. The shift and broadening were attributed to the state dependent light shift of the transition frequency induced by the trapping laser fields. The number of atoms was determined from the saturation measurement shown in Fig. 24(b). At high saturation the ensemble of trapped atoms absorbed 7.5 nW of the probe. Comparing this with the power radiated by a single saturated Cs-atom of 3.8 pW, yielded the number of trapped atoms to be 2000. From this analysis, they inferred an average absorbance per atom of 0.65%. Additionally, the trap lifetime was measured to be 50 ms, which was much smaller than the lifetime expected from background gas collisions.

A detailed investigation of the reduced trap lifetime in such a guided mode trap was addressed in Ref. [114]. Various types of heating mechanisms were experimentally investigated. It was inferred that the phase fluctuations of the standing wave trapping

field is the dominant heating process that probably leads to the limited lifetime. In a later publication, Wuttke *et al* reported that mechanical oscillations of the nanofiber in the form of high-Q torsional modes can optomechanically couple to the nanofiber guided field leading to phase and polarization fluctuations [115]. They pointed out that this may be another factor contributing to the reduced lifetime of atoms in the guided mode trap.

Reitz *et al* have further studied the ground state coherence properties of the atoms in such guided mode traps [116]. They used microwave radiation to coherently drive the clock transition. From the measured Ramsey fringes and spin echo signals they inferred a reversible dephasing time of $T_2^* = 0.6$ ms and an irreversible dephasing time of $T_2' = 3.7$ ms. From theoretical modeling, they inferred that the coherence times T_2^* and T_2' are mainly limited by the finite initial temperature of the atomic ensemble and the heating rate, respectively. However, the observed coherence times have opened possibilities to implement such an atom-nanofiber interface for various applications in quantum photonics.

Goban *et al* demonstrated a state-insensitive and compensated two-color nanofiber trap of Cs-atoms [38, 76]. They implemented pairs of counterpropagating red- and blue-detuned trapping beams at wavelengths of $\lambda_R = 937$ nm and $\lambda_R = 686$ nm, that is, close to the red-detuned and blue-detuned magic wavelengths, respectively. The polarization states of the trapping fields were chosen to be parallel to each other. Differential scalar light shifts were eliminated by the use of magic wavelengths, and the inhomogeneous Zeeman broadening due to the vector light shift was suppressed by 250 times due to the use of the counterpropagating configuration. In order to avoid mismatch in the standing waves of red and blue-detuned light, a large detuning between the counterpropagating blue-detuned beams was used leading to an effective moving standing wave. They measured an absorption linewidth $\Gamma/2\pi = 5.7 \pm 0.1$ MHz for the trapped Cs-atom $6S_{1/2}, F = 4 \rightarrow 6P_{3/2}, F' = 5$ transition, where $\Gamma_0/2\pi = 5.2$ MHz in free space. They inferred an optical depth per atom of 0.08 from the measured OD of 66. A trap lifetime of 12 ± 1 ms was measured, which was further extended to 140 ± 11 ms by polarization gradient cooling.

Several other groups have also implemented such two-color nanofiber traps [77, 78, 54, 47]. Apart from the HE_{11} mode trapping schemes there are several interesting proposals for using higher order modes of nanofibers for trapping atoms [117, 118]. Moreover, proposals exist for trapping using illumination of the nanofiber from the side [119]. A similar idea of side illumination trapping has been implemented for the
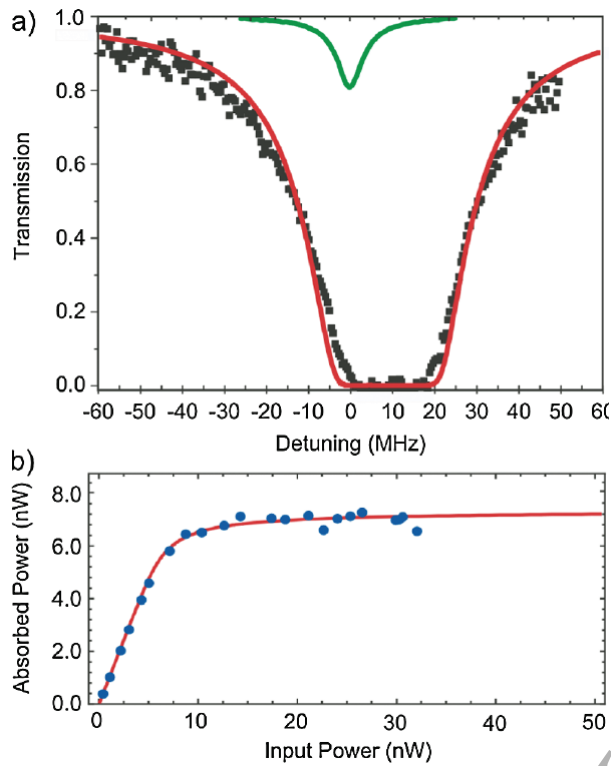
Figure 24. (Color online) (a) Absorption spectrum (black squares) for atoms trapped around a nanofiber. The spectrum is measured by monitoring the transmission of a weak probe field through the nanofiber after loading the trap. For reference, the spectrum of the MOT cloud (green line) measured through the nanofiber is plotted. The red line is a theoretical fit. (b) Saturation measurement (blue circles) for estimating the number of trapped atoms. The red line is a theoretical fit. From Ref. [37].

optical tweezer based trapping of single atoms on nanofiber and nanobeam cavities [12].

4.3. Scattering of the guided field by atoms around nanofiber

Due to the subwavelength confinement of light in the nanofiber guided modes, a single atom in the vicinity of the nanofiber can be excited within the atomic absorption cross-section. As a result the single atom can significantly scatter the guided field. Kien *et al* have investigated the scattering of an evanescent light field by a single cesium atom outside a nanofiber [32]. They showed that the confinement of the field and the presence of the longitudinal field component substantially affect the scattering process. They have estimated that, the transmittance of the field can be substantially reduced to 48% due to scattering into radiation modes (with the efficiency as high as 44%) and backward guided modes (with the efficiency as high as 8%).
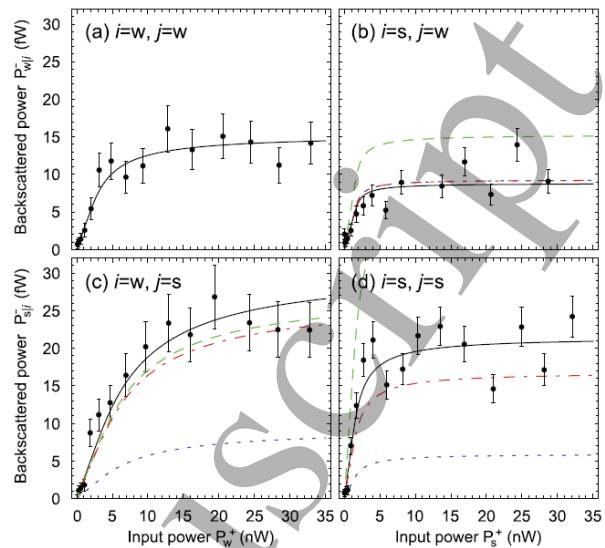
Figure 25. (Color online) Backscattering properties of an array of atoms trapped in a two color trap around the nanofiber. The black dots show the measured backscattered power per trapped atom as a function of P_i^+. The four panels show the data for different polarizer-analyzer settings as indicated. Each data point is the average of 80 experimental runs. The solid black lines are fits obtained by an ab initio model that includes the multilevel structure of the atoms and the full vectorial properties of the guided field. The dash-dotted red, dashed green, and dotted blue lines are calculated using the ab initio, the intensity-only, and the polarization-only models, respectively. From Ref. [121].

The scattering of the guided field by laser-cooled atoms around the nanofiber was first demonstrated by Sagué *et al* [34]. They measured the transmission spectrum of a weak probe field guided through the nanofiber overlapped with a laser-cooled atom cloud. They demonstrated that for an average atom number of 2 atoms in the vicinity of nanofiber, 20% of the guided light can be scattered at the on-resonance condition. They have further analyzed the spectral profiles measured for different probe powers, considering the light-induced dipole forces, van der Waals interaction, and enhancement of the spontaneous emission rate of the atoms around the nanofiber. Additionally, Kumar *et al* have measured the transient absorption of the guided mode field in order to estimate the temperature of the atoms around the nanofiber. Temperature variations from 160 μk to 850 μk, for a probe power ranging from 0 to 50 nW, have been observed [120].

Vetsch *et al* have demonstrated scattering of fiber guided light by atoms trapped in two diametrically opposite linear arrays around the nanofiber as shown in Fig. 24 [37, 113]. Similar measurements were also reported by Goban *et al* in a state-insensitive and compensated nanofiber trap [38]. There, they also measured the reflection spectrum by varying the number of trapped atoms. A broadening of the

reflection spectrum was observed with increasing atom number which they attributed to the randomness of the atomic distribution.

Reitz *et al* have reported a detailed analysis of backscattering properties of an array of atoms trapped in a two color trap around the nanofiber [121]. The array of atoms are trapped in two lines at azimuthally opposite directions on the nanofiber. The polarization along the axis containing the atoms is the strong-coupling axis (SCA) and that orthogonal to this axis is the weak-coupling axis (WCA). They have measured the saturation and polarization properties of the backscattered light for polarization of the excitation guided field aligned to SCA and WCA. The observations are shown in Fig. 25. Backscattering was observed for arbitrary input polarization and the backscattered power at saturation was found to be 3 orders of magnitude smaller than the input power. For the input polarization along the SCA, saturation occurs at lower input powers. A crucial observation was that significant backscattered power was found for the crossed polarizer-analyzer setting, which revealed the presence of an inelastic scattering mechanism that changes both the polarization of the scattered light and the internal state of the atom. The observations could only be understood by an ab initio model that included the multilevel structure of the atoms and the full vectorial properties of the guided field. The fitting to the data are shown by the black curves in Fig. 25.
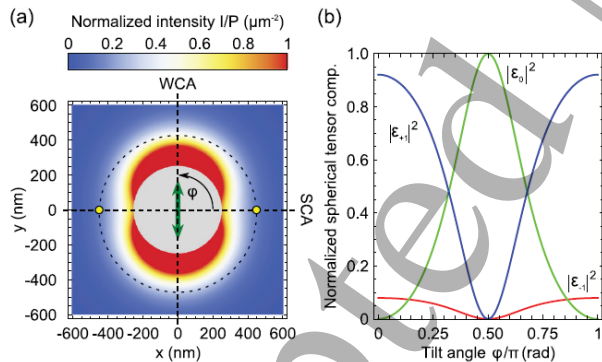

Figure 26. (Color online) (a) Density plot of the intensity profile of a quasilinearly polarized HE_{11} mode propagating in the $+z$ direction, calculated for $\lambda = 852$ nm. The trapped atoms are indicated by the yellow dots. The WCA and SCA are indicated by two dashed lines. Here the main polarization axis (green double arrow) coincides with the WCA ($\phi = \pi/2$). (b) Modulus squared of the normalized spherical tensor components $(\varepsilon_{-1}, \varepsilon_0, \varepsilon_{+1})/|\varepsilon|$ of the field for the right-hand-side atom as a function of ϕ, plotted in red, green, and blue, respectively. The components ε_{-1} and ε_{+1} have to be interchanged for the left-hand-side atom. From Ref. [121].

The complexity of the polarization of the guided mode which is strongly nonparaxial can be understood as being due to the tight confinement of the guided

field. As a result of the steep gradient of the transverse components, the evanescent region locally exhibits a significant longitudinal polarization component that is $\pi/2$-phase shifted with respect to the transversal components, as discussed earlier in Section 2. The total intensity and the longitudinal field component and thus the polarization vary azimuthally. The intensity profile of a quasilinearly polarized nanofiber guided field is shown in Fig. 26(a) [121]. Its main transversal polarization component and the plane containing the atoms enclose an angle ϕ. Figure 26(b) shows the modulus square of the normalized spherical tensor components as a function of ϕ, of the probe field propagating in $+z$ direction, at the position of the atom assuming the quantization axis along y-axis. If the polarization is aligned along the WCA ($\phi = \pi/2$), the intensity is minimum and the field is purely linear at the position of the atoms and drives π transitions. If the polarization is aligned along the SCA ($\phi = 0, \pi$), the intensity is maximum at the position of the atoms and the polarization is almost circular. The field then essentially drives the $\sigma^-(\sigma^+)$ transitions for atoms located at $x < 0(x > 0)$. If the probe field propagates in the reverse direction ($-z$ direction) then the polarization is reversed at the atom position.

Such an understanding of the complex polarization of the guided field has led to a series of interesting experiments demonstrating the chiral light-matter coupling on the nanofiber [55, 56, 122, 123, 124]. Below we review the experiments performed with an array of atoms trapped on the nanofiber.

Mitsch *et al* have demonstrated optical state preparation and manipulation by exploiting the polarization properties of the guided field [122]. They used atoms trapped in two diametrically opposite linear arrays around the nanofiber and, by using a single optical mode, the two atomic ensembles were simultaneously optically pumped to opposite Zeeman states. Moreover, using the state-dependent light shifts, they demonstrated independent coherent manipulation of the two ensembles. Using such precise control of quantum state, Mitsch *et al* have also demonstrated directional spontaneous emission from an array of trapped atoms on a nanofiber [55]. They were able to tune the spontaneous emission into the counterpropagating guided modes from symmetric to strongly asymmetric, where more than 90% of the fluorescence could be launched into one or the other direction.

Sayrin *et al*, have further extended the idea to demonstrate non-reciprocal light transmission through a array of atoms trapped on the nanofiber thus realizing an optical isolator controlled by the internal state of atoms [56]. They used a spin polarized linear array of atoms trapped on the nanofiber and measured
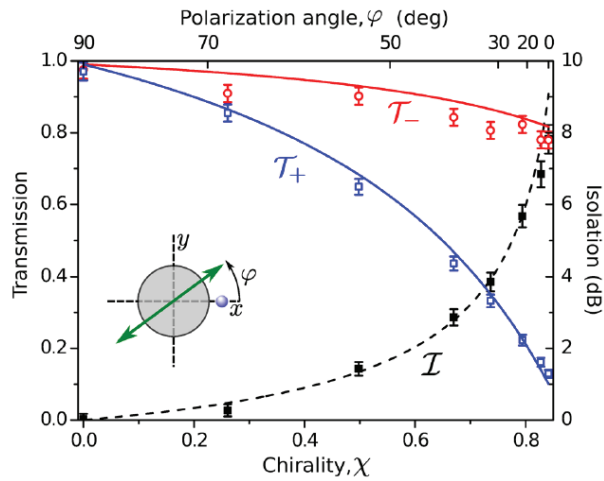
Figure 27. (Color online) Nonreciprocal transmission of photons interacting with an ensemble of spin-polarized atoms trapped around a nanofiber. Transmissions T_- (red circles) and T_+ (blue circles) and isolation I (black squares) as a function of the chirality χ, calculated at the position of the atoms. The lines overlaid on the data are the result of a numerical calculation with $\langle N \rangle \sim 27$. The error bars indicate the 1σ statistical error based on counting statistics. Inset: Cross section of the optical nanofiber (gray disk) including the trapped atoms (blue sphere) and the main polarization axis of the guided field (green double arrow). The angle between the main polarization axis of the guided field and the x axis is denoted as ϕ. From Ref. [56].

the transmission of a quasilinearly polarized weak probe field propagating in the forward and backward direction. The results of forward and backward transmission are plotted in Fig. 27 as a function of polarization. When the polarization is aligned along the atom position ($\phi = 0$), the chirality takes maximum value $\chi = 0.84$ and there is a strong nonreciprocal transmission $T_+ = 0.13 \pm 0.01$ and $T_- = 0.78 \pm 0.02$ demonstrating an isolation of $I = 7.8$ dB. When the polarization is aligned to the perpendicular axis ($\phi = \pi/2$), there is no chirality ($\chi = 0$) leading to equal transmission in both directions.

Based on such experimental advances, Kien *et al* have re-investigated the scattering problem in a more general formalism, considering the complex polarization properties of nanofiber guided modes and complex transition structure of the atom. They have shown that the scattering of the guided field by an atom can be asymmetric with respect to the forward and backward directions and depends on the polarization of the probe field [70]. Such anisotropy in scattering of light is a result of the complex transition structure of the atom and the existence of a longitudinal component of the guided-mode. Further Kien *et al* have investigated the propagation of nanofiber guided light through an array of atoms [125]. They have shown that when the array period is

far from the Bragg resonance, the backward scattering is weak. Conversely, if the period satisfies the Bragg resonance condition, most of the guided probe light can be reflected back into the backward propagating guided mode over a broad region of field detunings even though there is an irreversible decay channel into the radiation modes.
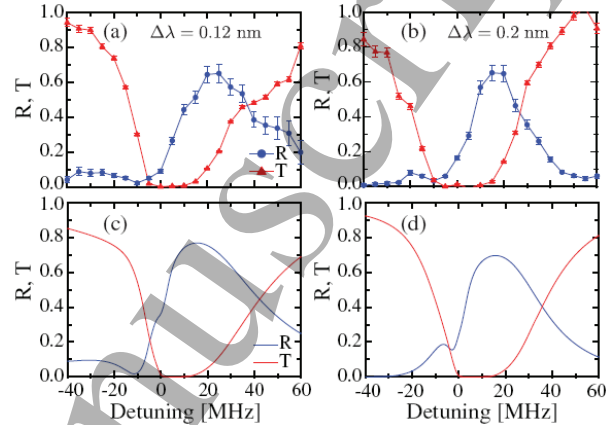
Figure 28. (Color online) Reflection and transmission spectra for a probe quasilinearly polarized along the y direction (atoms are trapped along x direction). (a) and (b) Experimental results and (c) and (d) the simulated spectra for $\Delta\lambda = 0.12$ nm and $\Delta\lambda = 0.2$ nm, respectively. From Ref. [47].

Sorensen *et al* [46] and Corzo *et al* [47] have experimentally demonstrated coherent Bragg scattering of the guided field by an array of atoms trapped on the nanofiber. Sorensen *et al* have used a two color (red (standing wave) and blue detuned (traveling wave) wavelength of 1057 nm and 780 nm) nanofiber trap to trap atoms and used near resonant light (detuning of -176 MHz) in standing wave configuration to structure the atomic array to satisfy the Bragg resonance condition [46].

On the other hand Corzo *et al* have used a laser with detunings of $\Delta\lambda = 0.12$ and 0.2 nm from the resonance as the red detuned standing wave laser for trapping the atoms on the nanofiber [47]. This satisfies the slightly detuned Bragg resonance condition. The reflection and transmission spectra of the resulting atomic Bragg mirror is shown in Fig. 28. It may be seen that for both the detunings of the trapping laser, a broad reflection band was observed with a peak reflectance of around 0.65 on the blue detuning side. The reflection spectra for a detuning of $\Delta\lambda = 0.2$ nm is slightly narrower and shifted towards the low frequency side. The observations agreed well with numerical simulations.

Dawkin *et al* have demonstrated a dispersive interface for nanofiber guided light using an ensemble of 1000 atoms trapped in the vicinity of an optical nanofiber [126]. This method relies on the
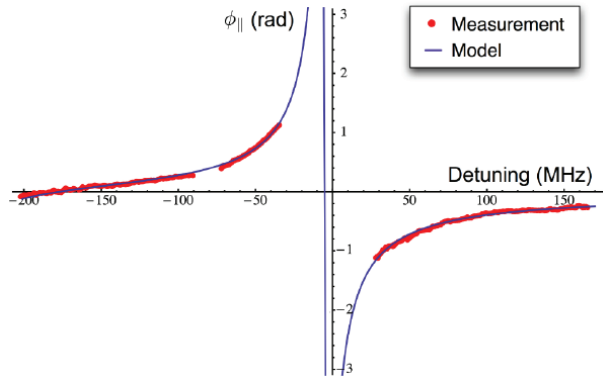
Figure 29. (Color online) Phase shift $\phi_\parallel$ of the eigenmode parallel to the atom trapping axis, induced by 1000 atoms and measured as a function of the detuning from the free-space transition frequency. From Ref. [126].

azimuthally asymmetric coupling of the ensemble with the evanescent field of an off-resonant probe beam, transmitted through the nanofiber. They used a polarization spectroscopy method to estimate the phase shift induced by the atoms. The measured phase shift $\phi_\parallel$ for the eigenmode parallel to the atom trapping axis is shown in Fig. 29 as a function of detuning of the probe field from the atomic resonance. One can see that the phase shift approaches 1 rad around a detuning of six times the natural linewidth corresponding to a phase shift per atom of ~ 1 mrad. Furthermore, they have implemented such a dispersive technique to nondestructively determine the number of atoms. Solano *et al* have implemented such a dispersive and nondestructive technique to measure the transient response of the atomic motion in the trap and measured the trapping frequency of the nanofiber trap [127].

There are also theoretical proposals for using the guided field to control the motion of atoms around the nanofiber. Kien *et al* have shown that there can be negative azimuthal force on particles around the nanofiber [128]. Sadgrove *et al* have proposed a tractor beam effect for ultracold atoms in the vicinity of a few-mode nanowaveguide [129]. Atoms trapped near the waveguide can be transported in a direction opposite to the guided mode propagation direction. There are also proposals and demonstrations for using higher order modes to increase the fluorescence collection and probe absorption [130].

4.4. Quantum nonlinear optics with an atomic ensemble

Strong light-matter interaction around the nanofiber opens new possibilities for quantum non-linear optics and single photon manipulation. As discussed earlier
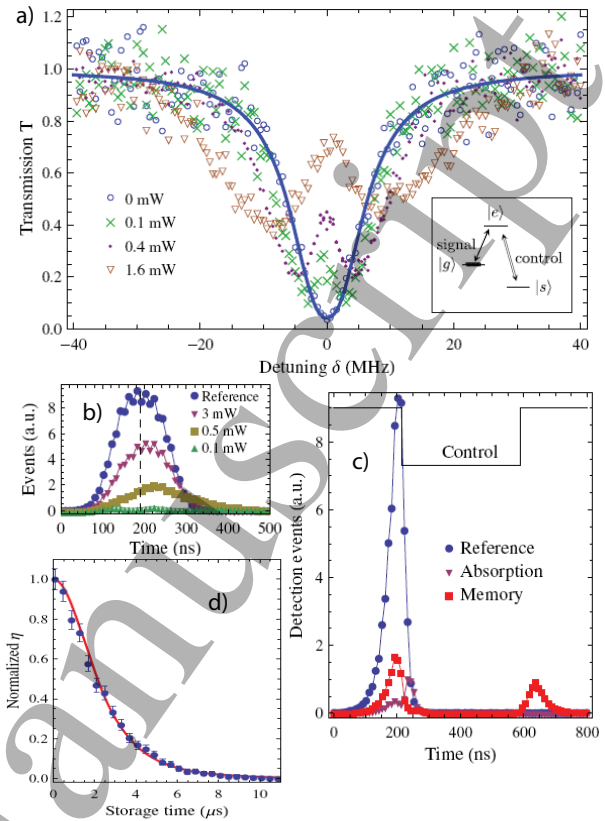
Figure 30. (Color online) (a) The transmission spectra of the signal field for different powers of the control field. A level scheme is shown in the inset. The Λ system for EIT involves the two ground states $\|g\rangle = \{6S_{1/2}; F = 4\}$ and $\|s\rangle = \{6S_{1/2}; F = 3\}$, and one excited state, $\|e\rangle = \{6S_{3/2}; F = 4\}$. The atoms are initially prepared in $\|g\rangle$. The control field is set resonant to $\|s\rangle \rightarrow \|e\rangle$ transition. While the signal frequency is scanned across $\|g\rangle \rightarrow \|e\rangle$ transition. Slow light (b) and storage (c) at the single photon level. (b) Time traces of the transmitted pulses for different control powers. The reference is measured without atoms. (c) Storage and retrieval. The purple and blue points show the transmitted pulse with and without atoms, respectively, in the absence of control field. The black line indicates the timing sequence of the control field for the photon storage experiment. The red data correspond to the memory sequence, showing leakage and retrieval. (d) Memory lifetime. Normalized retrieval efficiency η as a function of the storage time. From Ref. [44].

in this section, the spontaneous emission of atoms can be strongly modified around the nanofiber and a significant amount of atomic fluorescence can be coupled to the nanofiber. The efficient coupling of atomic fluorescence enables the detection of single atoms around the nanofiber. Additionally, a single atom on the nanofiber can efficiently scatter guided photons. The strong confinement of the guided field and long interaction length along the nanofiber enables the realization of an optically dense system around the nanofiber. Another key feature is the long-range coherent interaction between atoms on the nanofiber which leads to collective effects [131]. Kien *et al* have
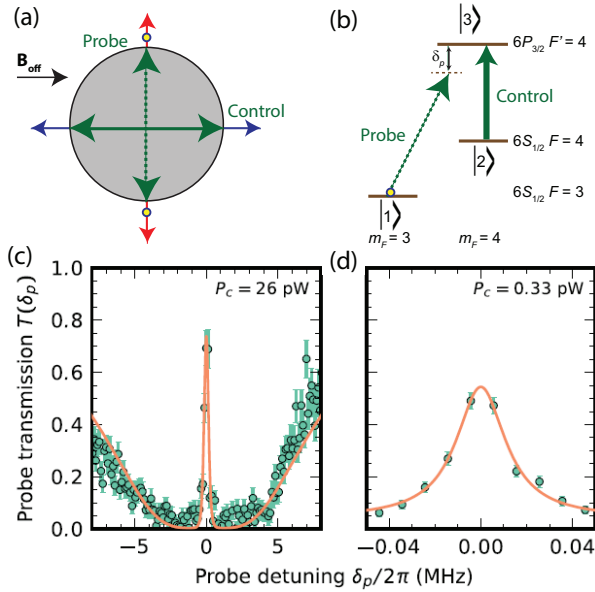
Figure 31. (Color online) (a) Schematic illustration of the cross-section of the nanofiber, showing the orientations of the principal axes of quasi-linear polarizations of the nanofiber-guided fields. The quantization axis is in the direction of B_{off}. (b) Schematic diagram showing the relevant Zeeman sublevels of the trapped cesium atoms used for the EIT experiment. The transitions driven by the laser fields are indicated. (c) and (d) Transmission spectrum of the guided probe field under EIT conditions. (c) A narrow transmission window is observed on an optically dense background. The width of the transmission window is clearly smaller than the natural linewidth. The control power is $P_c = 26$ pW, and the probe power is $P_p = 2.9$ pW. (d) For $P_c = 0.33$ pW, a transmission window that is about 10 times narrower is observed. Here, $P_p = 1.7$ pW. From Ref. [45].

Figure 32. (Color online) (a) Time traces of probe pulses transmitted through the TOF under EIT conditions for different control powers. The solid lines are Gaussian fits to the data. A delay of the pulses with respect to a reference pulse (dark green) is clearly visible demonstrating slow fiber-guided light. (b) Time traces showing the storage of light in a nanofiber-trapped ensemble of cold atoms. A pulse of duration $\tau = 0.2$ μs that contains 0.8 photons on average is launched into the TOF. The light pulse is stopped inside the atomic medium by reducing control power to zero (blue line). After 1 μs, control power is increased to its initial value, and the pulse is retrieved. From Ref. [45].

shown that due to the collective effect the coupling efficiency can be significantly enhanced [132]. Also as discussed earlier in this section, by atomic state preparation one can realize directional spontaneous emission into the guided mode and coherent Bragg reflection of photons. Due to such unique quantum optical properties of the nanofiber system, it is ideally suited for single photon manipulation in a fiber based system. Kien *et al* have established theoretical studies for atomic memory and heralded single photon generation on a nanofiber system by using electro-magnetically induced transparency (EIT) [133, 134, 135, 136, 137].

Storage of fiber guided single photons has been experimentally demonstrated using a cloud of laser-cooled atoms around the nanofiber [44] and also with trapped atoms on the nanofiber [45]. Gouraud *et al* have used a cloud of laser-cooled atoms to demonstrate EIT and photon storage [44]. They used a cigar shaped MOT around the nanofiber to realize an interaction length of 5 mm and an optical depth of OD=3. From absorption measurements, they estimated an effective

atom number of 2000±500. The signal to be stored was guided inside the nanofiber while the control field was introduced from the outside of the nanofiber, at an angle of 13° relative to the nanofiber axis, with a polarization perpendicular to the signal field.

Figure 30(a) shows the measured transmission spectra of the signal as a function of its detuning δ from resonance, for different values of the control power. One can see that when the control field is applied, a transparency window appears. The transparency close to 75% is measured for a control power of 1.6 mW. The slow-light effect of a weak laser pulse at single photon level, resulting from pulse propagation under EIT condition is shown in Fig. 30(b). When the control power was decreased, smaller transparency but larger delays were obtained due to the narrower transparency window. For a 0.5 mW control the signal pulse was delayed by 60 ns corresponding to a 3000-fold reduction in group velocity. Figure 30(c) demonstrates the storage results for a signal pulse with a mean photon number per pulse equal to 0.6 ± 0.1. The memory effect was observed when the stored signal

was retrieved after around 650 ns with an efficiency of 10±0.5%. Figure 30(d) shows the retrieval efficiency as a function of the storage duration. The storage time is limited to a few μs, which was understood to be due to the motional dephasing caused by the non-zero atom temperature.

Sayrin *et al* have demonstrated storage of fiber-guided light in a nanofiber-trapped ensemble of cold atoms [45]. The atoms are trapped on the nanofiber by using two-color guided mode trapping. Figure 31(a) shows the cross-sectional view of the nanofiber, illustrating the orientations of the principal axes of quasi-linear polarizations of the nanofiber-guided fields. The signal and the control fields were both launched into the guided mode. The polarization of the signal and control fields was quasilinear and aligned parallel and perpendicular to the trapping axis, respectively. Figure 31(b) shows the relevant Zeeman sublevels of the trapped cesium atoms. The transitions driven by the laser fields are indicated. The quantization axis is in the direction of B_{off}.

The transmission spectrum of the signal field is shown in Fig. 31(c) for a probe (signal) and control power of 2.9 pW and 26 pW respectively. One can see strong absorption of the signal field and a narrow EIT peak. The OD was measured to be 5.9±0.2 and the EIT transmission window has a width of 300 kHz and a peak transmission of 70%. As shown in Fig. 31(d) a much narrower EIT peak with a width of 26 kHz and peak transmission of 60% was observed by reducing the control power to 0.33 pW while the signal power was 1.7 pW. The slowing of the signal pulse for different control power is shown in Fig. 32(a). A delay of 22±1 μs and transmission of $13.6 \pm 0.5\%$ is measured for a control power of 0.33 pW. From the length of $\sim$1 mm of the trapped atomic sample, they estimated a group velocity of 50 m/s. The results for storage and retrieval of a signal pulse is shown in Fig. 32(b). One can see that the signal pulse is retrieved after 2 μs with an overall storage and retrieval efficiency of $3.0 \pm 0.4\%$.

Additionally, there have been nanofiber based demonstrations of Autler-Towns splitting and multi-level cascaded EIT using nanofibers [138, 139].

5. Interfacing solid-state quantum emitters

In the previous section, it was shown that nanofibers can be used to collect single photons from single atoms which are near to the nanofiber surface. However, in many cases, solid-state quantum emitters, such as semiconductor quantum dots and color-centers in diamond, may offer a more convenient source of single photons. In this context, integrating solid-state emitters to optical nanofibers may open new capabilities to generate single photons.

Some practical aspects of using solid-state emitters are that the emitter may be operated under ambient condition without the need for sophisticated laser-cooling techniques (as discussed for atoms) and the emitter may be placed directly on the surface of the nanofiber to increase the channeling efficiency. However some technical issues must be considered. One issue is that the host containing the emitter must be small enough in the form of a nanocrystal (NC). Additionally, it is essential to develop experimental techniques to deposit such a tiny NCs (dimension: 10 - 50 nm) containing a single quantum emitter on the nanofiber (diameter: 300 nm - 600 nm) without affecting the transmission of the nanofiber. Another issue to consider is that unlike naturally occurring atoms, the solid-state emitters are not identical and may have broad emission lines. Also they may have non-radiative decay leading to limited quantum efficiency.

In this section, we will review the use of nanofibers as an interface for collecting single photons with a high efficiency from solid-state quantum emitters including quantum dots (QDs) and nitrogen vacancy centers in nano-diamonds (NV/ND).

5.1. Interfacing single quantum dots with nanofibers

5.1.1. Spectroscopy and photon statistics of a single quantum dot Fujiwara *et al* demonstrated the efficient channeling of fluorescence photons from single QDs into single-mode optical fibers using optical nanofibers [39]. They used a dip coating technique to deposit single QDs on the nanofiber surface. The deposition procedure was as follows: nanofibers were dipped in a solution of QDs dissolved in toluene depositing QDs directly on the nanofiber surface. The nanofiber transmission dropped by less than 10% due to this deposition process.

The QDs were excited through a microscope objective lens (NA=0.8) at a laser wavelength of 543.5 nm. The fluorescence was collected by the same objective lens. An effective confocal pinhole was realized by coupling the fluorescence to a single-mode fiber (core size = 10 μm). The fluorescence collected by the objective lens was detected by an avalanche photo diode (APD) - APD1. The fluorescence channeled into the nanofiber guided modes was detected by another APD - APD2. Photon correlation measurements were performed using both the APDs.

Figures 33(a) and (b) show fluorescence scanning images of a single QD on a nanofiber measured through the objective lens and the nanofiber guided modes, respectively. The detected photon count rate (25 kcps in Fig. 33(b)) through the nanofiber guided modes was larger than that (18 kcps in Fig. 33(a)) detected through the objective lens. The total photon count rate detected from both ends of the nanofiber was 50 kcps.
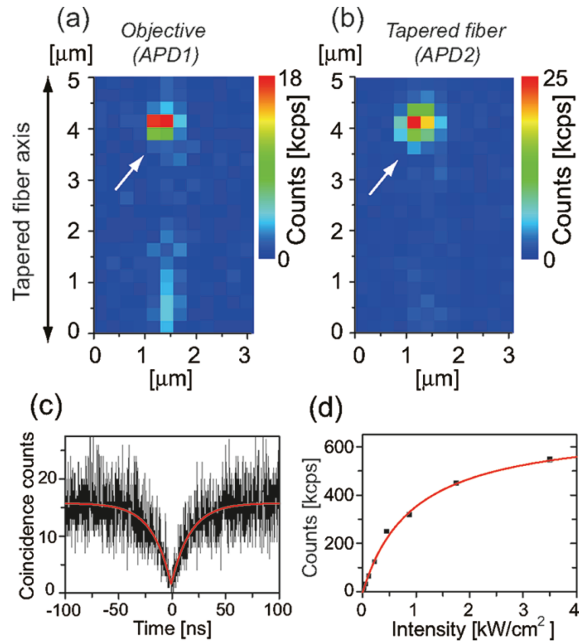
Figure 33. (a) and (b) show the fluorescence scanning images of single QDs on the nanofiber measured through objective lens and nanofiber guided modes, respectively. (c) shows the measured photon correlation for a single QD between objective lens and nanofiber guides modes (d) shows photon count rate versus excitation laser intensity. Adapted from [39].

The measured photon correlation for a single QD is shown in Fig. 33(c). It may be seen that anti-bunching occurs with a dip value of 0.096, demonstrating the presence of a single QD. The total decay time (τ) of the excited-state of this QD was determined to be 35.4 ns. They made measurements for three single QDs on the nanofiber and found the mean value of τ to be 29.6±2.1 ns. The photon count rate versus excitation laser intensity shown in Fig. 33(d) shows clear saturation behavior. Using a similar method, they measured the saturated photon count rates (n_∞) for three single QDs and found the mean value of n_∞ to be 592±90 kcps. They estimated the total channeling efficiency (both sides of the nanofiber) of fluorescence photons from the single QD into the nanofiber guided modes (η) using the following equation:

$$\eta = \frac{2n_\infty\tau}{\eta_{APD}\eta_F} \tag{35}$$

where η_{APD} is the APD quantum efficiency ($\eta_{APD} = 68\%$ at 600 nm) and η_F is the measured transmission efficiency from the nanofiber region to APD2 ($\eta_F = 70\%$). Using this method, η was estimated to be 7.4±1.2%. Here it should be mentioned that the quantum efficiency of the single QDs was implicitly assumed to be 100%.

Yalla *et al* reported a systematic and detailed approach to integrate single QDs to the nanofiber.

First of all they demonstrated a sophisticated technique for systematic and reproducible deposition of single QDs along an optical nanofiber with a precision of 5 μm using a sub-pico-liter needle-dispenser combined with an inverted microscope system [40]. Furthermore, they presented a detailed analysis of the fluorescence photon emission characteristics for single QDs on the nanofiber.

The main part of the experimental setup consisted of an inverted microscope, an optical nanofiber, and a sub-pico-liter needle-dispenser as shown in Fig. 34(a). The diameter of the nanofiber was around 400 nm and was uniform for 2 mm along the fiber axis. The transmission through the tapered fiber was around 90%.
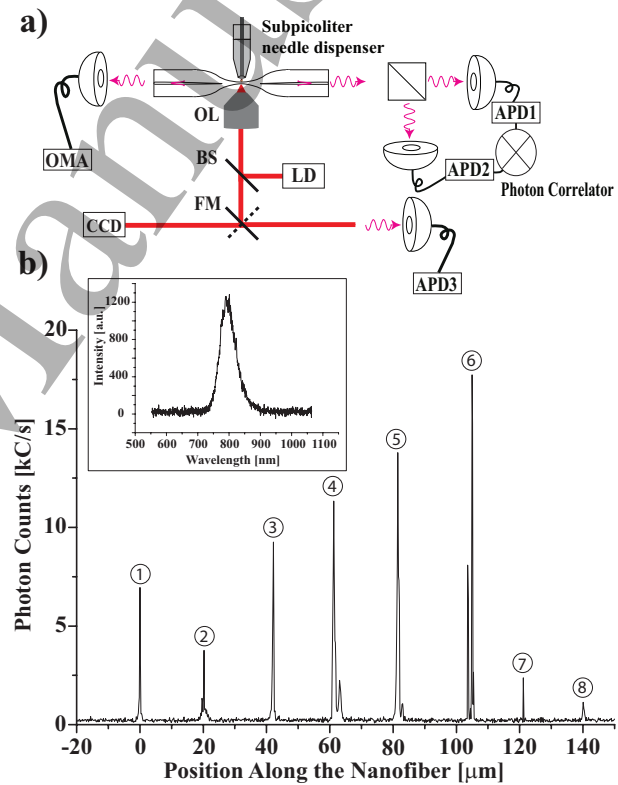
Figure 34. (a) Schematic diagram of the experiment. OL, BS, FM, LD, APD, and OMA denote objective lens, beam splitter, flipper mirror, laser diode, avalanche photodiode, and optical multichannel analyzer, respectively. (b) The fluorescence photon counts observed by scanning the excitation laser focus point along the nanofiber. Sharp emission peaks are clearly seen along the nanofiber with a spacing of 20 ± 5 μm, in good correspondence with the QD placement on the nanofiber. The inset shows a typical measured emission spectrum for a single QD on a nanofiber. The center wavelength is at 796 nm and the spectral width is 52 nm FWHM. Adapted from [40].

The core-shell type colloidal QD solution was diluted by pure water to give the optimum concentration for single QD deposition using the sub-pico-liter needle-dispenser. The dispenser consisted of a tapered

glass-tube which contained diluted QD solution and a needle having a tip of diameter 17 μm. Once the needle tip passed through the tapered glass-tube, it carried a small amount of solution containing QDs at its tip. In order to deposit small number of QDs on the nanofiber, the needle-tip position was adjusted so that the QD solution at its tip just touched the nanofiber. This was confirmed by sending laser light through the nanofiber and observing the scattered light due to the needle tip touching the nanofiber surface through the microscope. Using this technique, QDs were deposited periodically on the nanofiber by shifting the nanofiber along the fiber axis.

Figure 34(b) shows typically observed fluorescence photon counts as measured by scanning the excitation laser focus spot along the nanofiber. The observed sharp peaks in the photon count rate, with a spacing of 20 ± 5 μm, corresponded well with the positions of QD deposition on the nanofiber. For convenience of presentation, the deposited positions are numbered 1 to 8. Out of the eight positions, single QD behavior was observed at all positions except for the positions 4 and 6, which was confirmed by the photon counting and photon correlation measurements discussed below. Therefore this technique demonstrated a high probability for successful deposition of single QDs on the nanofiber. Moreover after the 8 depositions, the nanofiber transmission was reduced by 10%, suggesting an average loss per deposition of $\sim 1\%$.

The inset of Fig. 34(b) shows a typical emission spectrum for the deposited QD at one of the positions (position 3). The center wavelength is 796 nm and the spectral width is 52 nm FWHM. Although the measured width is narrower than the ensemble average value of 82 nm for the QDs [140], it is still relatively broad. The mechanism of the broadening may be understood as being due to spectral diffusion and exciton-phonon interactions which have been discussed in several publications for similar QDs [141, 142].

The QDs were excited using a cw diode-laser at a wavelength of 640 nm through a microscope objective lens. The fluorescence photons emitted from QDs were channeled to the guided mode of the nanofiber and were detected through the single-mode optical fiber. At one end of the single-mode fiber, the fluorescence light beam is split into two using a 50:50 non-polarizing beam splitter, and the split beams are re-coupled into multi-mode fibers and detected by fiber-coupled APDs as shown in Fig. 34(a). The photon correlations were derived from the arrival times of photons at both APDs recorded using a two-channel single-photon-counter. At the other end of the fiber, the fluorescence emission spectrum was measured using an optical-multichannel-analyzer (OMA) as shown in Fig. 34(a).

The results for the photon counting and photon correlation measurements for a typical position (position 3) are displayed in Fig. 35(a) and (b), respectively. Regarding the photon counts in Fig. 35(a), single step on/off-behavior was clearly observed. This on/off behavior was due to the blinking of the QDs, a well known phenomenon in solid-state single photon emitters [143, 144, 145, 146]. Single-step blinking is assumed to indicate a single QD within the laser excitation region. The typical normalized correlations clearly show anti-bunching behavior as seen in Fig. 35(b). The correlation value at the anti-bunching dip was 0.035. Therefore the number of QDs for this position was estimated to be one[147].
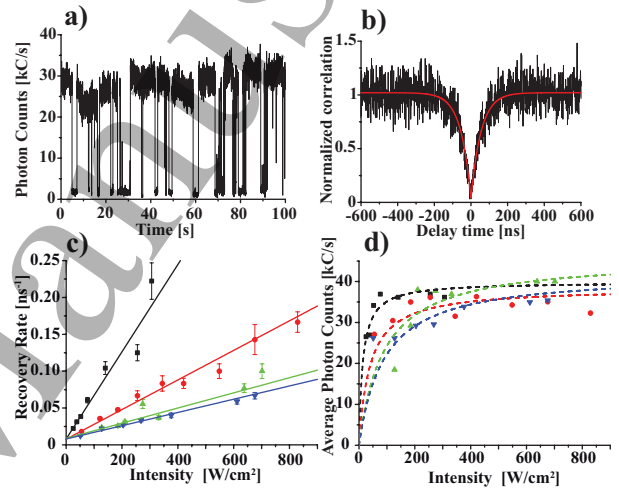
Figure 35. (a) and (b) show typical photon counts as a function of time and the typical normalized photon correlations $g_N^{(2)}(\tau)$ for a single QD, respectively. The red curve shows the exponential fitting of the normalized photon correlations. (c) shows the observed anti-bunching recovery rates $(1/T)$ for different excitation laser intensities for one/two dots on a nanofiber. The solid lines show the linear fits to the data. (d) shows the typical observed fluorescence photon-count rate for different excitation intensities for single QDs on a nanofiber. The observed photon counts are fitted (dashed curves) using Eq. (38). Adapted from [40].

The observed photon statistics were analyzed by using a rate-equation model for an incoherently pumped two-level system. Based on this model the observed photon count rate $n(t)$ into one side of the nanofiber guided modes is expressed by

$$n(t) = \eta_{APD}\eta_F \frac{\eta_q \eta}{2\tau} \frac{\alpha I}{\alpha I + 1/\tau}\{1 - \exp(-\frac{t}{T})\} \qquad (36)$$

where $1/T (= \alpha I + 1/\tau)$ is the intensity-dependent recovery rate of the antibunching signal which is essentially a population evolution of the excited state, αI is the excitation rate at laser intensity I, $1/\tau$ is the total decay rate of the excited state, η_{APD} is the quantum efficiency of APD, η_F is the

transmission efficiency, η is the channeling efficiency of the fluorescence photons into the guided modes, and η_q is the quantum efficiency of a QD. The quantum efficiency of a QD is expressed by

$$\eta_q = (1/\tau_r)/(1/\tau) \qquad (37)$$

where $1/\tau_r$ is the radiative decay rate of the excited state.

The measured anti-bunching signals at different excitation intensities were fitted by an exponential function to estimate the recovery rates $(1/T)$. In Fig. 35(c), the observed recovery rates for single QDs are plotted versus excitation laser intensity. The linear dependence may readily be seen. The data points were fitted by the least-mean square method, and the fitted results are shown by solid lines. The intercept at zero-intensity and the slope gave an estimate of $1/\tau$ and α, respectively. The decay times (τ) were distributed in the range of 150 ± 50 ns for the investigated QDs.

The average photon-count rate into the nanofiber guided modes integrated over timescales much longer than τ can be expressed as follows:

$$\langle n(t) \rangle = \eta_{APD}\eta_F \frac{\eta_q\eta}{2\tau} \frac{\alpha I}{\alpha I + 1/\tau} = n_\infty \frac{\alpha I}{\alpha I + 1/\tau} \qquad (38)$$

where n_∞ is the saturated photon count rate. Figure 35(d) shows the fluorescence photon-count rates $(\langle n(t) \rangle)$ versus excitation intensity measured for different single QDs. Saturation behavior may readily be seen in all the plots. The measured results were fitted using Eq. (38) by fixing the parameters α and $1/\tau$ to the values determined from the intensity dependence of the anti-bunching recovery rates. The adjustable parameter was n_∞.

They estimated the factor $\eta_q\eta$ from the obtained parameters using the following relation

$$\eta_q\eta = \frac{2n_\infty\tau}{\eta_{APD}\eta_F} \qquad (39)$$

where η_{APD} was assumed to be 60% at 780 nm and $\eta_F = 31\%$ was the measured light-transmission efficiency from the nanofiber region to the APD-detector.

The measured $\eta_q\eta$-values showed a variation from 0.033 to 0.094. This variation mainly reflected the variation of the quantum efficiency of QDs, since the η-value can be assumed to be equal for QDs distributed along the nanofiber within the range of 150 μm. Regarding the quantum efficiency η_q, the value supplied by the manufacturer was 72% [140, 148, 149]. It should be noted that this value is an average value measured for a liquid sample which contains a very large number of QDs. The η_q-value for a single QD is expected to be distributed around the mean value. The obtained highest $\eta_q\eta$-value of 0.094 corresponds to a QD which has the highest quantum efficiency among the measured QDs. Assuming the highest possible

η_q-value of 100%, they estimated a lower limit for channeling efficiency to be $9.4 \pm 3.0\%$.

5.1.2. Measurement of channeling efficiency For applications in quantum information science, channeling the single photons from a single quantum emitter into a single-mode fiber would be crucial requirement. In this line, optical nanofibers can be particularly promising due to their ability to directly channel fluorescence photons into a single-mode fiber. It has been theoretically predicted that it is possible to channel fluorescence photons into the nanofiber guided-modes with an efficiency of more than 20% [31, 64], by placing the emitter on the surface of the nanofiber.

As described in the previous section, two groups have reported the photon-counting measurements from semiconductor QDs deposited on nanofibers [39, 40]. However the channeling efficiency (η) was not inferred conclusively. Yalla *et al* demonstrated a rather straightforward method to estimate the channeling efficiency by comparing the photon-count rates through the guided and radiation modes [43]. They obtained the maximum channeling efficiency to be $22.0 \pm 4.8\%$ at a fiber diameter of 350 nm at an emission wavelength of 780 nm.

The experiments were performed using a similar setup described in Fig. 34(a). Nanofibers with diameter ranging from 300-800 nm were used for the experiment. The QDs on the nanofiber, were excited by focusing a continuous wave laser at a wavelength of 640 nm, using a microscope objective lens (OL) (40X, NA= 0.6). Regarding the fluorescence photons channeled into the guided modes, in order to guarantee observation of coupling to just the fundamental mode (HE$_{11}$), a single-mode fiber with cut-off wavelength of 557 nm was fusion-spliced to the tapered fiber. The fluorescence photons through the guided modes were then detected with a fiber-coupled APD1 as shown in Fig. 34(a). Regarding the radiation modes, the fluorescence photons were collected by the OL, coupled into a multi-mode fiber, and detected by a fiber-coupled APD (APD3) as shown in Fig. 34(a). Photon-counting measurements for both guided and radiation modes and spectrum measurements were carried out simultaneously for each deposited QD.

The channeling efficiency η into the nanofiber guided modes can be expressed as follows:

$$\eta = \frac{n_g}{n_g + n_r} = \frac{1}{1 + n_r/n_g} \qquad (40)$$

where n_g and n_r are photon emission rates into the guided and radiation modes, respectively. Observable photon-count rates by APD1 and APD3 are expressed as follows:

$$n_g^{(obs)} = \frac{1}{2}\eta_{APD1}\kappa_g n_g, \ n_r^{(obs)} = \eta_{APD3}\kappa_r\eta_r n_r \qquad (41)$$

where κ_g and κ_r are light-transmission efficiencies for the paths of guided and radiation modes, respectively. The factor $1/2$ for $n_g^{(obs)}$ implies that fluorescence photons into the guided modes are detected at one end of the nanofiber. η_{APD1} and η_{APD3} are the quantum efficiencies of APD1 and APD3, respectively, and are assumed to be the same. η_r is an effective collection efficiency for the radiation modes. Thus, the ratio n_r/n_g can be written as follows:

$$\frac{n_r}{n_g} = \frac{n_r^{(obs)}}{n_g^{(obs)}} \times \frac{\kappa_g}{2\kappa_r\eta_r} = \frac{n_r^{(obs)}}{n_g^{(obs)}} \times \zeta \qquad (42)$$

where $\zeta = \kappa_g/2\kappa_r\eta_r$.

κ_g and κ_r-values were measured to be $49.6\pm2.1\%$ and $23.5\pm1.3\%$ respectively. The measurement procedures can be found in Ref [43]. The effective collection efficiency η_r for the radiation modes, depends on two factors. One is due to the numerical aperture (NA) of the OL. The collection efficiency of the OL is estimated to be 10% from the NA-value of 0.6. The other factor arises from the lensing effect of the nanofiber. The QDs were deposited on the upper surface of nanofiber and the OL collected the fluorescence photons from the lower side of nanofiber. Therefore, the nanofiber acts as a cylindrical lens and may enhance the collection efficiency of the OL. The calculation of enhancement factor due to this lensing effect is detailed in Ref. [150, 151]. Based on this formalism, the average enhancement factor was estimated by assuming a random azimuthal distribution of QDs on the upper surface of the nanofiber. For the fiber diameters used in this experiment, it was found that the average enhancement factor could be assumed to be constant with a value of 1.48 ± 0.03. This average enhancement factor was used to obtain the effective collection efficiency η_r. Using this method, they obtained the η_r-value to be $14.8\pm0.3\%$ and consequently the ζ-value to be 7.13 ± 0.84 by combining the values of κ_g, κ_r, and η_r.

Typical fluorescence photon-count rates from QDs on a 400 nm diameter nanofiber are shown in Fig. 36(a). The photon-count rates through the guided and radiation modes are denoted by black and red traces, respectively. It may readily be seen that the two traces exactly match each other apart from their amplitudes. A clear single step blinking behavior is observed, revealing that the number of deposited QDs was one. This was further confirmed by measuring the anti-bunching dip in the normalized photon-correlations, and the dip-value was measured to be $0.035 \ll 1$. As described in Ref. [43], they obtained $n_g^{(obs)}$ and $n_r^{(obs)}$ to be 44.3 ± 5.4 and 24.8 ± 3.7 kcps, respectively. Using the relation of Eq. (42), the ratio n_r/n_g was found to be 3.99 ± 1.55. Thus, using Eq. (40) η was found to be $20.0\pm6.2\%$.
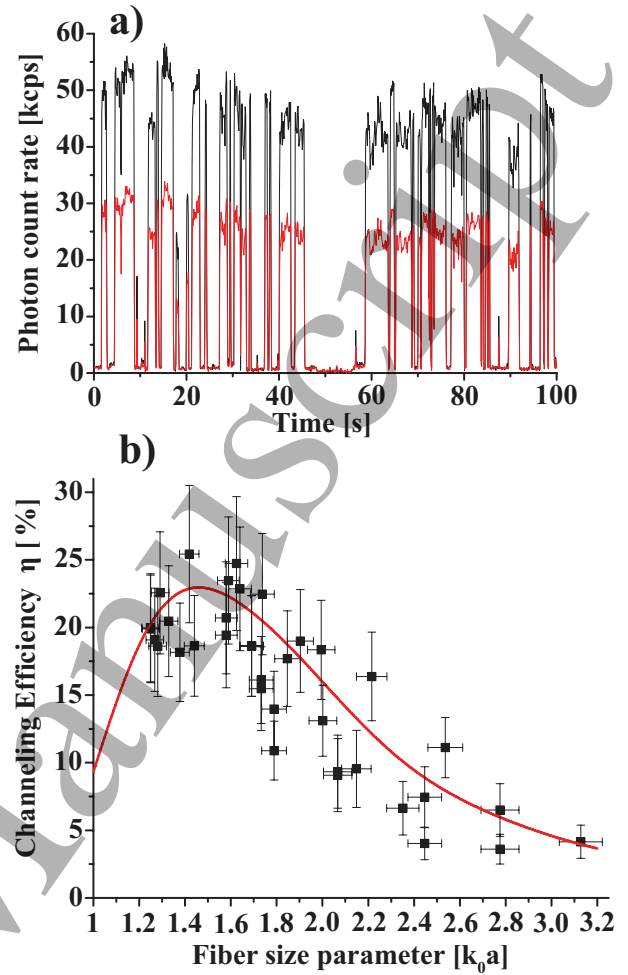
Figure 36. (a) Typical fluorescence photon-count rate from a single QD as a function of time. Black and red traces correspond to fluorescence photon-count rates observed through guided and radiation modes, respectively. (b) Channeling efficiency as a function of fiber size parameter ($k_0a = 2\pi a/\lambda$). The red curve shows the theoretical prediction. Measured values are marked by black squares with error bars. Adapted from [43].

Using the same procedure, η-values were obtained at various fiber diameters. The channeling efficiency η as a function of the fiber size parameter ($k_0a = 2\pi a/\lambda$) is shown in Fig. 36(b). For each deposited position, the size parameter was calculated from the measured fiber-diameter $2a$ and the observed emission-wavelength λ. The theoretical prediction for the channeling efficiency into the HE_{11}-mode is shown by the red trace. For the theoretical calculations the refractive-index of nanofiber material was assumed to be 1.45. All measured values are plotted versus the size parameter as black squares. Vertical error bars denote the fluctuation of photon counts at each deposited position. Horizontal error bars denote the ambiguity of the fiber-diameter measurements. The enhancement due to the nanofiber lens effect

creates an additional ambiguity. For the experimental analysis, the average enhancement factor was used assuming random azimuthal distribution of deposition, but the enhancement factor for each deposited position is expected to be different from the average value. Although experimental ambiguities still exist, the measured results reproduced the theoretical prediction within the experimental error. The estimated maximum channeling efficiency into the guided modes was found to be 22.0±4.8%, by averaging for data points around the fiber size parameter of 1.4, which corresponds to the fiber diameter of 350 nm for the emission wavelength of 780 nm.

5.2. Interfacing nitrogen vacancy centers in nano-diamonds with nanofibers

Schroder *et al* demonstrated the coupling of a single nitrogen vacancy in a nanodiamond (NV/ND) to an optical nanofiber [41]. They used a dip coating technique to deposit NV/NDs on the nanofiber. A schematic of the deposition technique is shown in Fig. 37(a). The deposition procedure is as follows: a thin glass rod was then dipped into an aqueous ND solution to create a small droplet of ND solution. The nanofiber region was dipped into this small droplet of ND solution. Scattered light was observed through a microscope objective lens while sending a laser through the nanofiber guided modes in order to confirm ND deposition, as shown in the top panel of Fig. 37(b).
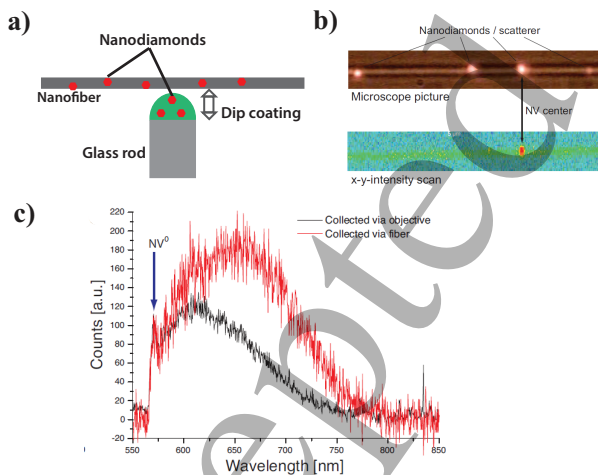
Figure 37. (a) Schematic of the dip coating technique to deposit NV/NDs on the nanofiber. (b) Top: Microscope image of the nanofiber, while sending a laser through the nanofiber guided modes. Bottom: fluorescence scan of the same region. (c) shows the emission spectrum of a single neutral NV/ND. The black and red traces correspond to the fluorescence observed through the objective lens and nanofiber guided modes, respectively. Adapted from [41].

The NDs were excited through a microscope

objective lens (NA = 0.8) with a laser wavelength of 532 nm. The fluorescence was collected through the same objective lens. Simultaneously the fluorescence channeled into guided modes of the nanofiber was measured at the ends of the single-mode fiber. To identify NV/NDs on the nanofiber, confocal fluorescence imaging was performed by scanning the position of the focused excitation laser spot. A typical scan is shown in the bottom panel of Fig. 37(b). To further confirm the presence of NV/NDs, the fluorescence emission spectrum was observed through the guided modes and objective lens. The measured emission spectra of a single NV/ND, observed through the nanofiber guided modes (red trace) and objective lens (black trace) are shown in Fig. 37(c). Sharp peaks in the spectra around 575 nm may be clearly seen, indicating the zero-phonon line of a neutral NV/ND. The broad peak in the red side corresponds to the phonon sideband.
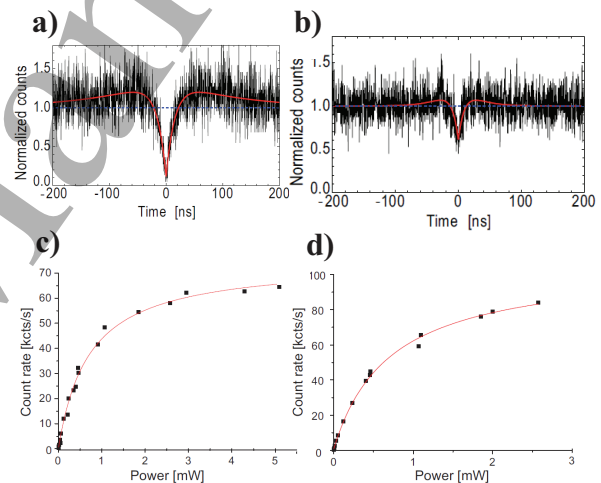
Figure 38. (a) shows the measured normalized photon correlations for a single neutral NV/ND measured through the objective lens, confirming the presence of a single NV/ND. (b) shows the photon correlation measurements between the two nanofiber ends, confirming the presence of a single NV/ND on the nanofiber. (c) and (d) show the measured fluorescence photon count rates from a single neutral NV/ND through the objective lens and one end of the nanofiber, respectively. Red solid lines are fitting results as described in Ref. [41]. Adapted from [41].

A typical photon correlation data for the single neutral NV/ND measured through the objective lens is shown in Fig. 38(a). The measured anti-bunching dip value was 0.11, indicating the presence of a single NV/ND. Photon correlations were also performed between the fluorescence signals from both ends of the nanofiber guided modes. A typical result is shown in Fig. 38(b), where the anti-bunching dip value of 0.61 indicated the presence of a single NV/ND. They also investigated the fluorescence

photon count rate dependence on the excitation laser power. Figure 38(c) and (d) show the fluorescence photon count rate at various excitation powers as measured through the objective lens and nanofiber guided modes, respectively. The observed saturated photon count rates through the objective lens and nanofiber guided modes (single end) were 74±2 kcps and 104±1 kcps, respectively.
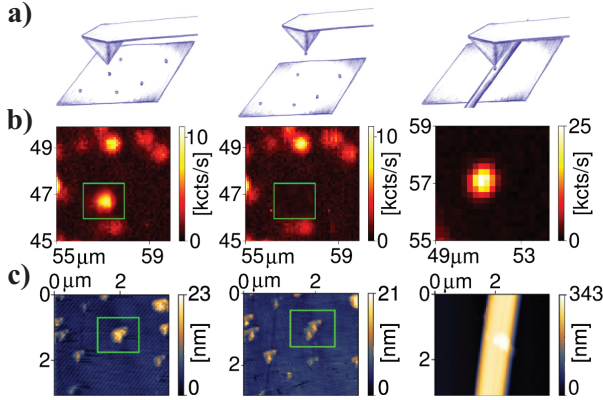
Figure 39. (a) Schematic of the technique for deterministic deposition of single NV/NDs on the nanofiber.(b) and (c) are typical florescence scans and AFM images of a single NV/ND before pick-up, after pick-up, and after depositing onto the nanofiber (from left to right), respectively. Adapted from [42].

Liebermeister *et al* demonstrated a sophisticated technique for deterministic deposition of a single NV/ND onto a nanofiber using a confocal microscope combined with an atomic force microscope (AFM) [42, 152]. A schematic of the deposition technique is shown in Fig. 39(a). They used the following three-step procedure: First, NV/NDs (mean diameter of 25 nm) were found on a fused silica substrate by performing the fluorescence imaging and confirming single photon emission from the NV/ND using a standard photon correlation technique. Second, the pre-characterized NV/ND was imaged with the AFM tip and consequently picked up by the AFM tip. Third, this NV/ND was deposited onto the nanofiber by placing the nanofiber on a clean substrate and touching it with the AFM tip. Typical confocal scans and AFM images of the above process are shown in Fig. 39(b) and (c), respectively. Finally, the nanofiber was removed from the substrate for further optical experiments.

The NV/ND deposited on the nanofiber was excited through a microscope objective lens (NA=0.75) with a laser at a wavelength of 532 nm. The fluorescence was collected with the same microscope objective lens and through the nanofiber guided modes. They measured photon correlations at various excitation laser powers through the objective lens as well as through the nanofiber guided modes. The

observed anti-bunching of the fluorescence photons confirmed the deterministic deposition of a single NV/ND. Moreover, by comparing the saturated fluorescence photon count rates for the nanofiber guided modes and the objective lens (free-space modes), they obtained lower and upper bounds for the channeling efficiency of 9.5±0.6% and 10.4±0.7%, respectively.

Some key requirements for implementing solid-state emitters as a single photon source are to realize narrower emission lines and higher quantum efficiencies. In recent years there have been significant research and developments in finding better solid-state emitters. One example is silicon vacancy (SiV) center in nanodiamonds, which can have a strong and narrow zero-phonon line at room temperature [153, 154]. On the other hand cooling the QDs or NDs to cryogenic temperatures will be essential. Recent reports on cooling NDs [155] and molecules [156] on a nanofiber to cryogenic temperatures have opened promising possibilities in this direction.

6. Cavity QED on a nanofiber

6.1. New prospects for cavity QED using nanofibers

Efficient quantum state transfer between single atoms and photons is a rudimentary requirement for the realization of quantum networks [4]. The interaction of a single atom with strongly confined photons in an optical cavity leading to cavity QED (cQED) effects, is a promising approach to realize a quantum interface. There has been extensive research and development on coupling single atoms to free-space Fabry-Perot (FP) cavities [8, 9, 10, 11]. Below, we briefly summarize the key parameters for cQED. The interaction dynamics is mainly governed by the competition between the coherent atom-photon coupling rate ($2g_0$ = single photon Rabi-frequency) and the incoherent decay rates i.e. atomic spontaneous emission rate (γ_0) and cavity decay rate (κ). The coupling rates are given by

$$g_0 = \sqrt{\frac{\mu^2 \omega_c}{2\hbar\epsilon_0 V_m}}; \kappa = \frac{\omega_c}{Q_m} = \frac{\pi c}{F L}; \gamma_0 = \frac{8\pi^2 \mu^2}{3\hbar\epsilon_0 \lambda^3} \quad (43)$$

where μ is the transition dipole moment, $\omega_c = \frac{2\pi c}{\lambda}$ is the atomic transition frequency that corresponds to wavelength λ, $\hbar$ is the reduced Planck's constant, ϵ is the free-space permittivity, c is the speed of light in vacuum, F is the finesse of the cavity mode, L is the optical length of the cavity, Q_m is the quality factor of the cavity mode and V_m is the cavity mode volume. The atom-field interaction can be strongly enhanced when the cavity is resonant to the atomic transition and the atom is placed at an antinode of the cavity

mode. The figure of merit of the atom-field coupling is defined by a cooperativity parameter (C), given by

$$C = \frac{(2g_0)^2}{\kappa\gamma_0} = \frac{3Q_m}{4\pi^2}\left(\frac{\lambda^3}{V_m}\right) \tag{44}$$

The spontaneous emission of the atom is strongly modified in the presence of a cavity, giving rise to the well known Purcell effect. The Purcell enhancement factor P is given by

$$P = \frac{\gamma_c}{\gamma_0} = \frac{\frac{(2g_0)^2}{\kappa} + \gamma_0}{\gamma_0} = C + 1 \tag{45}$$

where γ_c is the total decay rate of the atom in the prensence of cavity.

A crucial requirement to achieve strong interaction between single photons and single atoms, is that $C >> 1$ which requires large Q_m (or F) and small V_m comparable to λ^3. Even with $C >> 1$, there are two regimes with different dynamics: a) the Purcell regime, when $\kappa > 2g_0$, γ_0 and b) the strong-coupling regime, when $2g_0 > \kappa$, γ_0.

There have been various efforts to design microcavities to realize smaller mode volumes and high finesse. In the strong-coupling regime, quantum phenomena such as single-atom lasing and vacuum Rabi oscillations have been demonstrated using free-space FP cavities. Extremely high finesses of 40,000 to 400,000 are required to achieve the strong-coupling regime in a conventional free-space FP cavity. Although high quality mirrors with transmission and scattering loss less than 2 ppm have been reported, the overall cavity transmission may drop to 10-20% [11]. On the other hand, cavity QED experiments in the Purcell regime have been invetigated using various designs of nanophotonic cavities [15, 12, 13, 14, 18]. In particular, the designs have focused on applications like single photon generation, single photon switching and quantum nonlinear optics, where high transmission and fast response of the cavity is essential.

The typical design principle for nanophotonic cavities has focused on minimizing the mode volume and maximizing the Q-value (finesse). However by defining the cQED parameters in terms of mode volume, the transverse and longitudinal dimensions are grouped together. In fact, the mode volume is inversely proportional to energy density (photon flux) and can be written as a product of effective mode area (A_{eff}) at the atom position and optical length (L) of the cavity. As a result the atom-field coupling rate and the cooperativity can be written as

$$g_0 = \sqrt{\frac{c\gamma}{L} \times \frac{\sigma_{\text{Atom}}}{A_{\text{eff}}}} \tag{46}$$

$$C = \frac{4}{\pi}\left(\frac{\sigma_{\text{Atom}}}{A_{\text{eff}}}\right)F \tag{47}$$

where $\sigma_{\text{Atom}} = \frac{3\lambda^2}{2\pi}$ is the single atom absorption cross-section. From the above equations it may be seen that the transverse ($\frac{\sigma_{\text{Atom}}}{A_{\text{eff}}}$) and longitudinal ($F$) confinements can be treated independently and C is independent of the cavity length. In particular, this is a striking feature of cQED on a nanofiber.

In the context of a quantum network, efficient integration of the quantum interface to the existing fiber network will be a major technical requirement. In this context, optical nanofibers offer a flexible alternative platform. As discussed in Section 3, using the adiabatic tapering condition, efficient mode coupling to the nanofiber region can be realized. This will enable efficient integration to fiber networks. As discussed in the previous sections, the optical nanofiber has proven to be a promising platform for quantum optics experiments. In order to further extend the nanofiber method for implementing single atom based quantum nonlinear processes, the longitudinal confinement of the guided field in a nanofiber-based cavity will be essential.

In order to gain insight about the interaction dynamics in a nanofiber based cavity we follow the formalism developed in Ref. [48]. Based on this formalism, the cQED parameters are given by

$$g_0 = \sqrt{\frac{c\gamma_g}{L}} = \sqrt{\frac{c\gamma\eta}{L}} \tag{48}$$

$$C = \frac{(2g_0)^2}{\kappa\gamma_0} = \frac{4}{\pi}\eta\frac{\gamma}{\gamma_0}F = \frac{4}{\pi}\eta P^{(0)}F \tag{49}$$

where $\gamma = \gamma_g + \gamma_{\text{rad}}$ is the total decay rate, γ_g is the decay rate into the guided mode, γ_{rad} is the decay rate into the radiation mode, $P^{(0)}$ is the Purcell factor and η is the channeling efficiency of spontaneous emission of the atom near the bare nanofiber in the absence of the cavity. It should be noticed that C is independent of L. C mainly depends on the longitudinal confinement through F and the transverse confinement of the optical mode through η ($\propto 1/\omega_0^2$, where ω_0 is the effective mode waist). The effective mode waist of the nanofiber or other nanophotonic structures can be less than 1 μm which is one order smaller compared to the typical mode waist of 10 - 30 μm for free space FP cavities. This leads to two orders improvement in cooperativity for nanofiber cavities. In other words, high cooperativity can be achieved even for moderate finesse of 50 - 100. Furthermore, in the case of nanofiber cavities, it is possible to independently control the cavity length without affecting the transverse confinement. Therefore the cavity length can be controlled to reach the strong-coupling regime, since κ reduces faster than $2g_0$ as the cavity length increases. In fact, based on the achievable finesse range, one can select the cavity

length and fiber diameter to enable both regimes of cavity QED.

Additionally the spontaneous emission of atoms can be strongly modified near the nanofiber cavity and the channeling efficiency into the guided modes can be significantly enhanced. The Purcell factor (P) and channeling efficiency ($\eta^{(c)}$) for the nanofiber cavity can be written as

$$P = \frac{\gamma^{(c)}}{\gamma_0} = \frac{\gamma_g(1 + \frac{(2g_0)^2}{\kappa\gamma_g}) + \gamma_{\mathrm{rad}}}{\gamma_0} = P^{(0)} + C \qquad (50)$$

$$\eta^{(c)} = \frac{\gamma_g(1 + \frac{(2g_0)^2}{\kappa\gamma_g})}{\gamma_g(1 + \frac{(2g_0)^2}{\kappa\gamma_g}) + \gamma_{\mathrm{rad}}} = \frac{\eta(1 + \frac{4}{\pi}F)}{1 + \frac{4}{\pi}\eta F} \qquad (51)$$

where $\gamma^{(c)}$ is the total atomic decay rate in the presence of nanofiber cavity. It may be seen that the decay rate into the guided modes is enhanced by a factor $(1 + \frac{4F}{\pi})$. The expressions for the Purcell factor and channeling efficiency clearly show the separate effect of the nanofiber and the cavity. As discussed in previous sections, the channeling efficiency can be $\eta \simeq 0.2$ for a randomly polarized atom on the nanofiber surface. From this, the above equation can easily be used to estimate that for a moderate finesse of 30 the channeling efficiency into the guided modes can be enhanced to $> 90\%$. Such high channeling efficiency in a moderate finesse cavity is well-suited for a fiber-based single photon source.

6.2. Cavity formation on nanofibers

In the last decade various techniques have been proposed and developed to realize a nanofiber cavity. Nanofiber cavities can be broadly divided into two categories: one in which the cavity is fabricated directly on the nanofiber, and the other in which a fiber inline cavity includes a tapered fiber with a nanofiber waist. First we will discuss various methods to fabricate cavities directly on the nanofiber.

In order to fabricate a cavity structure on the nanofiber a crucial requirement is to realize efficient fiber Bragg grating (FBG) mirrors. To achieve this periodic index modulation of the nanofiber guided modes is essential. In conventional techniques for making FBGs on single-mode optical fibers, the core refractive index is modified by irradiating the fiber with a high power ultraviolet (UV) laser light. These techniques rely on the photosensitivity of the Ge/GeO$_2$ doped core of fibers. However, nanofibers are fabricated by tapering the single-mode optical fiber down to diameters much smaller than the core-mode cutoff diameter. As a result the core of the original single-mode fiber might be almost vanishing at the nanofiber region and the nanofiber is essentially made

of pure silica (cladding material of the original fiber). Hence, standard UV irradiation techniques may not be useful to make FBGs directly near the nanofiber region.
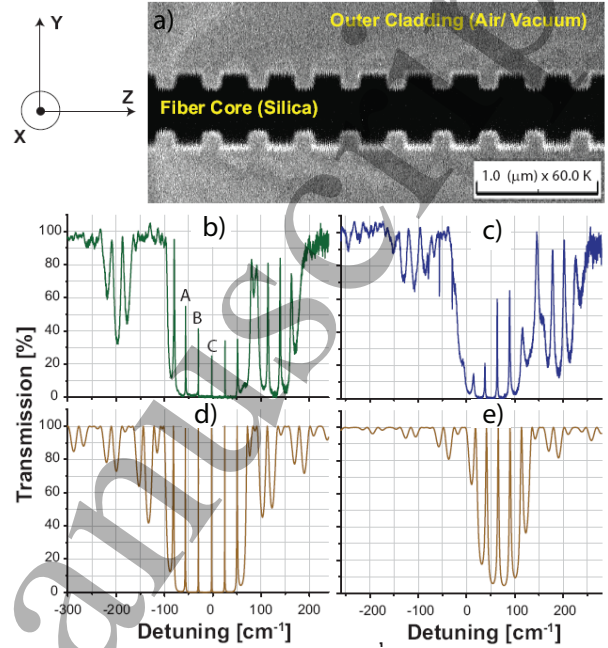
Figure 40. (Color online) (a)The SIM image of a typical part of NFBG, showing periodic nano-grooves drilled on the nanofiber using the FIB milling technique. (b) and (c) The experimentally measured transmission spectrum of a 100 μm nanofiber cavity for two orthogonal input polarizations x- and y-polarization, respectively. The orientations of the polarization axes are indicated in (a). (d) and (e) The theoretically calculated spectra for input polarizations perpendicular and parallel to the plane of the grooves, respectively. From Ref. [49].

Nayak *et al* have demonstrated fabrication of FBG mirrors and cavities on a nanofiber using focused ion beam (FIB) milling to produce periodic nano-grooves on the nanofiber [49]. Such periodic structures on the nanofiber induce strong modulation of the refractive index and act as FBG mirrors for the nanofiber guided modes. Using such FBG structures on the nanofiber they realized nanofiber cavities as described below.

The scanning ion microscope (SIM) image of a typical section of the fabricated nanofiber Bragg grating (NFBG) is shown in Fig. 40(a). The nanofiber diameter is $\sim$ 560 nm, each groove has a depth of $\sim$ 100 nm and width of $\sim$ 150 nm. The grating period is $\Lambda_G \sim 360$nm. Nayak *et al* fabricated two such NFBGs each consisting 120 periods and separated by 100 μm on the nanofiber axis to realize a nanofiber cavity.

Figures 40(b) and (c) show the measured transmission spectra of the nanofiber cavity for two orthogonal polarizations x- and y-polarization, respectively. The orientations of the polarization axes are as indicated in Fig. 40(a). The broad dip in the

center of the spectra correspond to the reflection bands of the NFBGs and the equispaced peaks appearing within the reflection band correspond to the cavity modes. The width of the reflection band for the x-pol is ~ 170 cm^{-1} (~ 12 nm) which is much broader than that of a typical FBG. The observed free spectral range (FSR) for the x-polarization is ~ 27 cm^{-1} (810 GHz). The cavity modes marked as A, B and C have a finesse of 42, 96 and 117 respectively and the corresponding transmission values are 55, 41 and 25% respectively. The finesse increases towards the center of the reflection band indicating the increase in the reflectivity of the NFBGs. A reflectivity of $\sim 97\%$ was estimated for the highest finesse value of $F = 117$ at around the center of the reflection band, assuming equal reflectivity for both the NFBGs. The Q-value for this mode is approximately 50,000. The reflection band for the y-pol is narrower and blue shifted relative to the x-pol which was understood as being due to the reduced effective index along the nano-grooves. The theoretical calculations almost reproduced the observed spectral shapes except for the transmission values for the cavity modes. The observed reflection side bands may correspond to additional Fourier components resulting from non-sinusoidal modulation of the refractive index.

Several other groups have produced similar cavities, although with shorter spacing between the Bragg mirrors. Schell *et al* reported a Q-factor of 250 for a structure with $N = 80$ periods in each Bragg mirror [157, 158]. Here, a defect cavity was used in which the cavity separation was negligible compared with the length of the Bragg mirrors. Li *et al* demonstrated a Q factor of nearly 800 for only 20 periods in each Bragg mirror with a spacing of 2.2 μm between Bragg mirrors [159].

Although FIB allows the creation of arbitrary cavity structures, it is time-consuming and requires that the nanofiber be mounted in special machinery. Additionally, there are various technical limitations in FIB fabrication such as contamination from the substrate or the ion beam itself and mechanical instability of the nanofiber due to charging up effects. Given these limitations, fabrication of nanofiber Bragg gratings using an optical method might be a better approach.

Nayak *et al* have demonstrated fabrication of photonic crystal cavities on nanofibers using femtosecond laser induced ablation [51, 160, 161, 162]. They have shown that thousands of periodic nano-craters are fabricated on an optical nanofiber following irradiation with just a single femtosecond laser pulse. A schematic of the fabrication setup is shown in Fig. 41(a). A femtosecond laser with a 400 nm center wavelength and 120 fs pulse width, was used for
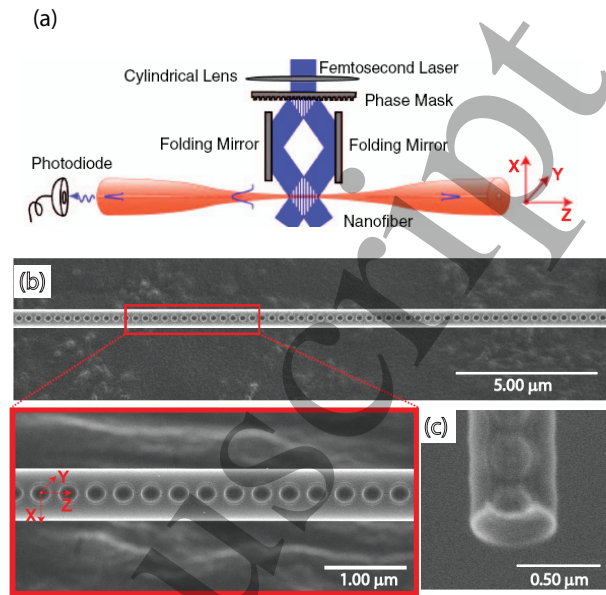
Figure 41. (Color online) (a) Schematic of the femtosecond laser fabrication setup. From Ref.[160]. (b) SEM image of a typical part of a sample fabricated using single-shot irradiation. The inset shows the enlarged view. The periodic nano-crater structures are observed on the shadow side of the nanofiber. (c) The cross-sectional image of the nanofiber sample at a typical nano-crater position measured by tilting the nanofiber at an angle of 33°. From Ref. [51].

the fabrication. A two-beam interference technique was used to create periodic intensity pattern on the nanofiber using a phase mask as the beam splitter and two folding mirrors. A cylindrical lens is used to line focus the femtosecond laser along the nanofiber. A zero-order block is used to avoid any residual zero order light in the interference region.

The SEM image of a typical segment of the fabricated nanofiber sample is shown in Fig. 41(b). It may be seen that periodic nano-craters are formed on the nanofiber. The period is 350 nm, which corresponds well to the interference pattern. It should be noted that the nano-craters were formed on the *shadow side* of the nanofiber. The inset shows an enlarged view of the sample. The nano-craters look circular in shape and the diameter of a typical nano-crater is around 210 nm. The cross-sectional image of the nanofiber at a typical nano-crater position is shown in Fig. 41(c). The image was measured by tilting the nanofiber at an angle of 33°. The nano-crater has a bowl-like shape and the depth is $\sim$120 nm.

For a typical sample, thousands of such periodic nano-craters are fabricated on a nanofiber with diameter around 450 - 550 nm. The diameter profile of the nano-crater array follows the Gaussian intensity profile of the femtosecond laser beam giving an apodized profile with diameter gradually varying

from 50 - 250 nm over a length of 1 mm. One key aspect of the technique is that the nano-craters occur on the fiber's underside relative to the incident beam. This fact, along with the essentially perfect positioning of the craters in the nanofiber's center demonstrates that the nanofiber itself acts as a cylindrical lens for the light pulse, focusing it to the center of the shadow side of the nanofiber. Moreover, the single-shot fabrication makes it immune to mechanical instabilities and other fabrication imperfections. Such periodic nano-craters on the nanofiber, act as a 1-D PhC and enable strong and broadband reflection while maintaining high transmission out of the stopband.

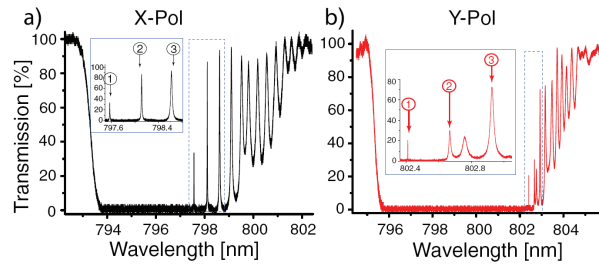**Figure 42.** (Color online) Transmission spectrum of an apodized PhC nanofiber cavity fabricated using femtosecond laser ablation technique, for (a) x-pol and (b) y-pol. The parts of the spectra, marked by blue boxes are enlarged and shown in the insets. From Ref. [160].

Figures 42(a) and (b) show the transmission spectra of an apodized PhC nanofiber cavity fabricated using the femtosecond laser ablation technique for x-pol and y-pol (as denoted in Fig. 41), respectively. The spectra for both the polarizations show wide stopband regions, where more than 98% of the input light is reflected and transmission drops to a few percent. The stopband for the x-pol extends from 793.7 to 798.8 nm. The stopband for the y-pol is much broader compared to that of the x-pol and is red-shifted. The stopband is well understood as the Bragg reflection from the periodic nanocraters on the nanofiber. The sharp peaks observed in the red-side of the stopbands are the cavity modes due to the apodized index variation.

The cavity modes for the x-pol marked as 1, 2 and 3 have a finesse of 71, 39 and 16 respectively with a corresponding transmission of 33, 87 and 93% respectively. The effective cavity length of ~ 0.54 mm is estimated from the mode spacing which corresponds well to the Gaussian width of the diameter profile of the nano-crater array. The cavity modes for the y-pol marked as 1, 2 and 3 have a finesse of 500, 27 and 11 respectively with corresponding transmissions of 21, 30 and 73% respectively. The transmission away from the stopband is around 100% ensuring that the fabrication does not induce significant loss and maintains the optical quality of the nanofiber. Additionally, we

note that the observed high-finesse cavity modes inside the stop band provide evidence of the quality of the fabrication.

Nayak *et al* have also demonstrated fabrication of a defect induced photonic crystal cavity on nanofiber by placing an absorber in the center of the femtosecond laser beam [160]. The typical cavity length realized was around 1.3 mm and cavity modes with finesse as high as 200 were measured.

The femtosecond laser ablation technique has also been used to create cavities with effective lengths an order of magnitude longer than those considered above. Keloth *et al* have reported the fabrication of a centimeter-scale cavity directly on a nanofiber [161]. A schematic of the cavity is shown in Fig. 43(a). They have fabricated two photonic crystal structures separated by 1.2 cm on a 1.7 cm long nanofiber using femtosecond laser ablation, thus forming a long nanofiber cavity. A crucial technical requirement for this approach was to fabricate long nanofibers with highly uniform waist and maintaining high transmission. The nanofiber used in this experiment had a diameter of 500 ± 2 nm over the entire length of 1.7 cm and the total transmission of the tapered fiber was $> 99\%$. They showed that such a cavity is suitable for operation in both the Purcell and strong-coupling regimes of cavity QED.

The cavity QED parameters for the cavity are summarized in Fig. 43(b). Assuming a single atom trapped 200 nm away from the fiber surface they estimated $2g_0 \simeq 52$ MHz, shown by the red dashed line in Fig. 43(b). The κ and on-resonance transmission (T_0) values for different modes are shown by green and blue circles respectively. The κ values for the cavity modes with finesse in the range of 200 to 400, are smaller than the estimated $2g_0$. Therefore they can enable the strong-coupling regime of cavity QED, with high cooperativity of 10 – 20. Moreover the on-resonance transmission values for such cavity modes can be as high as 40% to 60%, suggesting a one-pass intracavity transmission of 99.5%. The cavity modes with finesse below 200, are suitable for applications in the Purcell regime, such as fiber-based single-photon sources and quantum nonlinear optics. They can enable cooperativity in the range of 3–10 and show high transmission over 60% to 85%.

In the above methods the nanofiber Bragg mirror cavities are realized by periodic modulation of the core refractive index. In principle similar effects can be realized by modulating the cladding refractive index. Sadgrove *et al* have demonstrated a photonic crystal nanofiber created by bringing an optical nanofiber into optical contact with a nanostructure grating [163]. They call such a device a *composite photonic crystal nanofiber*. This method has been used to realize a so-
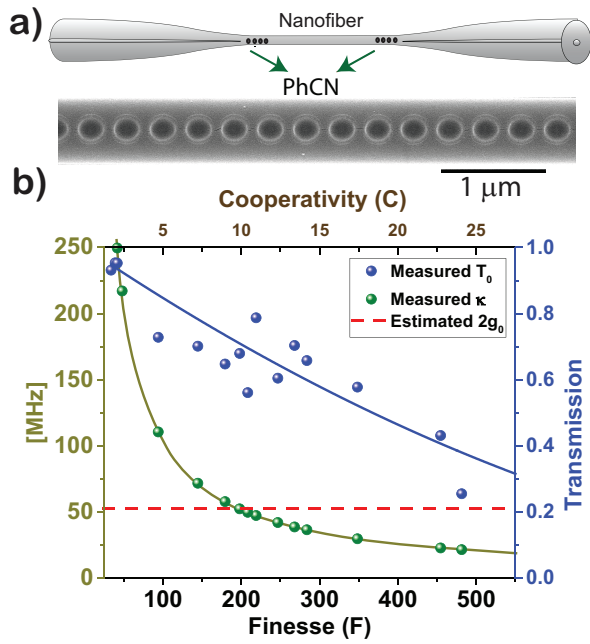
Figure 43. (Color online) (a) Schematic diagram of the nanofiber cavity. (b) The green and blue circles show the measured cavity linewidths (κ) and on-resonance transmission (T_0), respectively, vs the finesse (F) values for the typical cavity modes. The red dashed line shows the estimated single photon Rabi frequency ($2g_0$). The corresponding single atom cooperativity (C) is shown in the top axis. From Ref. [161].
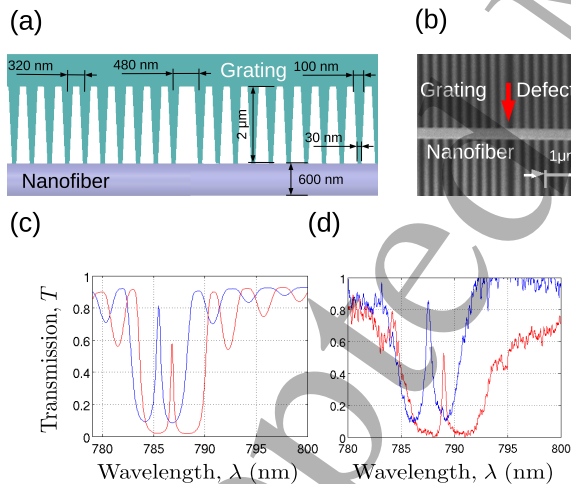

Figure 44. (Color online) (a) Schematic depiction of a composite photonic crystal nanofiber cavity. (b) Scanning electron microscope image of an experimentally realized composite photonic crystal cavity device. (c,d) Experimentally measured and theoretically predicted transmission spectra respectively for the composite photonic crystal cavity discussed in the text. In both cases, the blue line shows the x-polarized mode and the red line shows the y-polarized mode. From Ref. [52].

called "defect" cavity in which the periodicity of the

grating is disrupted at the grating center to create a relatively small mode volume cavity [52]. The device is depicted schematically in Fig. 44(a) and a scanning electron microscope image is shown in Fig. 44(b). The grating creates a periodic index modulation which is experienced by the fundamental mode in the nanofiber. This leads to Bragg reflection of the fundamental mode at the Bragg resonant frequency determined by the grating period and the effective refractive index of the nanofiber/grating combination.

Figures 44(c) and (d) show the transmission as a function of wavelength for x-polarized (blue line) and y-polarized (red line) nanofiber fundamental modes from FDTD simulations and experimental measurements respectively. It may be seen that for either polarization a broad stop-band is created and a single narrow cavity mode appears at the center of the stop-band. This is a clear signature of photonic crystal cavity formation. The simulation and experimental observations were found to be in good correspondence. The separation between the x- and y-mode resonance peaks are 1.3 nm (simulations) and 1.4 nm (experiments). The minimum transmission values for the stopbands of x- and y-polarizations and the peak transmission value for x-mode agreed with the simulation values within the experimental error, while the experimental transmission value of y-mode was found to be less than the simulation value by 16%. Regarding the quality factors (Q-factors) the simulation (measured) values for x- and y-mode were 1410 (1270 ± 20) and 2590 (2310 ± 80), respectively [52]. The simulation (measured) x- and y-mode transmissions were 81% (85 ± 6) and 59% (50 ± 4). From the simulations they estimated an effective cavity length of $L \sim 33\,\mu$m. Using this value for cavity length, they estimated a finesse of 28 for the measured y-mode.

We note that the composite method can be useful in settings where enhanced photoluminescence from solid state quantum emitters is required. A key advantage is that due to the composite nature of the setup the emitter can be quasi-deterministically positioned to the cavity center. Additionally, as mentioned earlier, one application uses the sensitivity of the Bragg resonance wavelength to the exact fiber diameter to make sensitive measurements of nanofiber diameters [97]. A proposal has also been made to use the composite method to realize a sophisticated atom trapping scheme in which the grating structure is illuminated to produce arrays of trapping sites whose positions coincide with antinodes of the cavity mode induced by the grating [164].

A different approach for realizing a cavity on a nanofiber is to use a fiber-inline cavity which includes a tapered fiber with a nanofiber waist. A fiber-inline cavity can be realized by splicing commercial
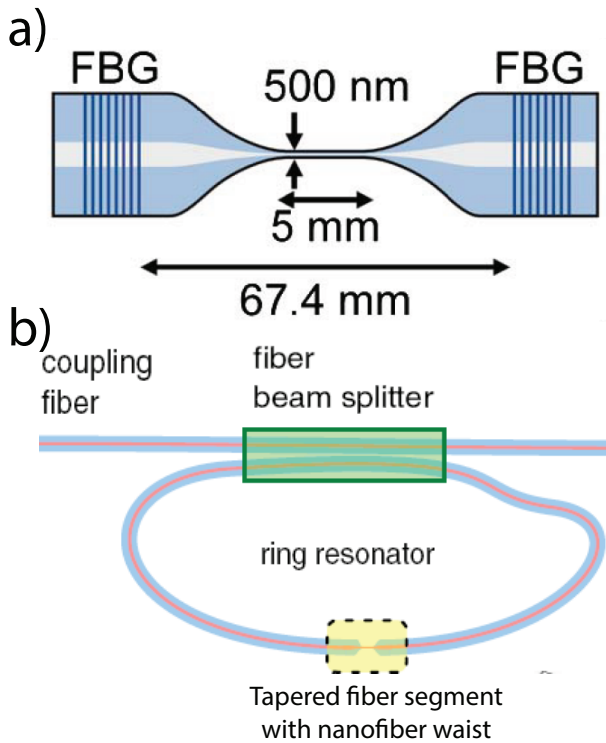
Figure 45. (Color online) (a) Schematic depiction of a FBG based fiber-inline nanofiber cavity. From Ref. [50]. (b) Schematic depiction of a fiber ring cavity with a nanofiber segment. From Ref. [53].

fiber Bragg gratings (FBGs) to the tapered fiber. A schematic diagram of the cavity is shown in Fig. 45(a). Wuttke *et al* have demonstrated such a FBG based cavity with a cavity length of 10.2 cm [50]. A typical finesse of 85 is realized in such settings and the cavity transmission was limited to 11% owing to the loss in the tapering region. Kato *et al* have implemented a similar cavity to demonstrate strong-coupling regime of cavity QED with single trapped atoms [54].

Another approach is to use a fiber-inline ring cavity with nanofiber segment. This can be realized by splicing the tapered fiber to a fiber splitter. The schematic diagram of the cavity is shown in Fig. 45(b). Jones *et al* have demonstrated a fiber ring resonator comprised of a relatively long loop of standard single-mode fiber with a nanofiber segment [165]. The cavity finesse was limited to 4. Later Schneeweiss *et al* improved this technique to realize a finesse of 75 for a cavity length of 2.35 m [53]. Rudell *et al* have implemented such a cavity to demonstrate strong-coupling with multiple emitters [111].

The cavity QED parameters for different types of nanofiber cavities are summarized in Table 1. The $2g_0$ and C values are estimated using Eqs. (48) and (49), respectively. For the estimation we have taken $\eta = 0.04$ assuming the D2-line transition for a single Cs-atom,

trapped 200 nm from the surface of a nanofiber with 500 nm diameter. It should be noted that solid state emitters can be placed on the fiber surface which will further enhance the $2g_0$ and C values by 2.5 and 5 times, respectively.

It may be seen from Table 1 that for the composite nanofiber cavity the effective cavity length is around a few tens of microns, and the estimated finesse is around 28. The κ values can be as high as 100 GHz while the cooperativity can still be 5-10 for an emitter on the surface. Moreover a high transmission value of 50-60% can be realized for the cavity mode. Similar short cavities can also be realized using FIB fabrication [157, 159]. However the reported Q-values are not as high as the composite cavity. The FIB fabricated cavity mentioned in the second row of Table 1, has a cavity length of a few hundred microns. But the finesse is 4 times better than composite cavity leading to 4 times higher cooperativity. Such cavities are suitable for solid state quantum emitters and fast generation of single photons.

For cavity lengths on the order of a few mm, as realized by femtosecond laser ablation, a high cooperativity of >25 can be realized with κ values of several hundreds of MHz. Such cavities are suitable for quantum nonlinear optics in the "Purcell" regime, with single atoms trapped 200 nm from fiber surface. The cavity with length on the order of one cm is particularly interesting as it can support both the Purcell and strong-coupling regimes of cavity QED with high cooperativity and high transmission. The FBG based cavities have lengths of a few tens of centimeters. Such cavities allow the strong-coupling regime of cavity QED to be achieved in a relatively simpler settings, without the need for sophisticated nanofabrication techniques. However, the cooperativity and cavity transmission are reduced, due to the inclusion of the tapered section. The ring cavities have even longer lengths of a few meters. As a result, the finesse is further reduced and hence the cooperativity reduces to below 1, which means that multiple emitters are necessary to achieve strong atom-photon coupling.

6.3. Demonstration of Purcell enhancement using a nanofiber cavity

Purcell enhancement of the spontaneous emission from a single QD into the nanofiber guided modes was first demonstrated using the composite photonic crystal nanofiber cavity discussed in the preceding section [52]. The experiments were performed by depositing colloidal quantum dots (QDs) with an 800 nm center-wavelength on the nanofiber by brushing a droplet of QD solution on the nanofiber surface. QD number was estimated from blinking statistics and by performing photon correlation measurements using a Hanbury-

Table 1. Summary of nanofiber cavity.

No.	Type of cavity	L (mm)	F	Q	κ (MHz)	$2g_0$ (MHz)	C	T (%)
1	Composite Method [52]	0.033	28	2.2×10^3	162×10^3	1.1×10^3	1.43	50-60
2	FIB Fabricated [49]	0.18	117	49.5×10^3	7.1×10^3	470	6	25
3	Femto Ablation (short) [160]	1.27	500	1.5×10^6	236	177	25.5	21
4	Femto Ablation (Long) [161]	14.4	175	5.9×10^6	59.5	52.5	9	65
5	Femto Ablation (Long) [161]	14.4	314	10.6×10^6	33.2	52.5	16	46
6	Two FBG Cavity [50]	102	85	20.4×10^6	17.3	19.7	4.3	11
7	Ring Cavity [53]	3407	75	300×10^6	1.17	2.4	0.95	

BrownTwiss setup. The details of these techniques are discussed in Section 5. The QDs were excited by using a 640 nm wavelength laser of power 35 μW focused by an objective lens. Using a nanopositioning stage, the QD was positioned in the center of the excitation spot to better than ±1 μm by monitoring the QD fluorescence. The defect position of the grating was aligned to within ±1.5 μm of the excitation spot center. The enhancement of QD emission was measured through the nanofiber after making optical contact between the grating and the nanofiber in order to form the composite cavity.

Figure 46(a) shows the photoluminescence spectrum for 3-5 quantum dots (as estimated from observation of blinking in the raw photoluminescence measurements) deposited on the nanofiber and near the cavity center, measured at the output of the nanofiber. Two enhancement peaks are clearly visible with $\lambda_{\text{res}} = 787.3$ nm and $\lambda_{\text{res}} = 788.5$ nm corresponding to the x- and y-polarizations respectively. The x-mode FWHM was 0.5 ± 0.2 nm and that of the y-mode was 0.4 ± 0.1 nm [52].

The enhancement factor (EF) E for a given polarization is defined as the ratio of the on-resonant photoluminescence in the presence of a cavity to the photoluminescence at the same wavelength in the absence of the cavity. Experimentally, the value in the absence of the cavity was estimated by measuring the off-resonant photoluminescence. Specifically,

$$E = \gamma_g^{(c)}/3\langle\gamma_g^{(0)}\rangle, \tag{52}$$

where $\gamma_g^{(c)}$ is the decay rate into the guided modes of the CPCC, and $\langle\gamma_g^{(0)}\rangle$ is the polarization averaged decay rate into the bare nanofiber guided modes. Note that all the polarizations contribute to the background PL intensity, but only the x- or y-polarization contributes to the enhancement peak. The decay rate in the CPCC may be written $\gamma_g^{(c)} = (\gamma_g^{(c)}/\Gamma)(\Gamma/\Gamma_0)\Gamma_0$, where the first bracketed term is the channeling efficiency η_c, the second bracketed term is the Purcell factor P, Γ is the total decay rate of the QE, and Γ_0 is the free-space decay rate of the QE. Note that the enhancement factor is not in general equal to the Purcell factor. As
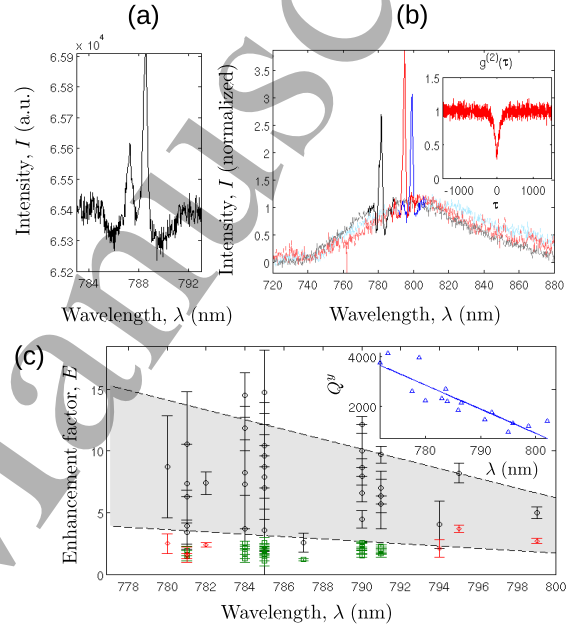
Figure 46. (Color online) (a) Photoluminescence measurements from several quantum dots coupled to a composite photonic crystal cavity device. The left-hand (right hand) peak shows the x-polarized (y-polarized) mode. (b) Photoluminescence measurements for three different single quantum dots coupled a composite photonic crystal cavity. In each case, a sharp enhancement peak was seen on top of the broad emission background. (c) EFs for single QDs in the composite photonic crystal cavity and cavity Q-factors. Red diamonds and green squares with error bars show measured EFs, while black circles show corrected EFs. Measured Q-factors for the y-mode cavity peaks are shown in the inset, with the solid line showing a linear fit to the data. From Ref. [52].

seen in Fig. 46(a), the experimentally determined ratio between the enhancement peak heights and wavelength separation between x- and y-polarization modes was found to exhibit good correspondence with the simulation values.

Figure 46(b) shows examples of Purcell enhancement peaks in the photoluminescence of three different *single* quantum dots deposited on nanofibers of different radii and near the cavity center. The inset shows a typical antibunching signal confirming the presence of a single quantum dot. The different radii of the

nanofibers lead to different values of n_{eff} for the fiber mode and therefore different resonant frequencies of the composite photonic crystal cavity. Additionally, since the exact position of the quantum dots in the cavity is effectively random with respect to the cavity antinodes, the amplitude of the enhancement peak is different in each case. Although the x- and y-mode peaks were not resolved at the OMA resolution (1.5 nm) used in the measurement, the observed PL intensity peak was asigned to the y-polarized dipole component since the y-mode peak is larger (see Fig. 46(a)). The measured EFs were 2.7 ± 0.2, 3.9 ± 0.3, and 3.0 ± 0.2 at $\lambda_{\text{res}} = 782.0$ nm, 795.0 nm, and 799.0 nm (black, red and blue curves respectively) [52].

Enhancement results for a number of different conditions, along with numerically estimated y-polarization Q-factors, are shown in Fig. 46(c). For a QD randomly placed with respect to the cavity antinodes and the QD azimuthal position randomly distributed between $0°$ and $90°$, the EF was expected to lie within the gray shaded region. The simulated EF was found to increase as λ_{res} became shorter due to the associated rise in the Q-factor (blue triangles in the inset of Fig. 46(c)).

The red and green points in Fig. 46(c) show the measured EF as a function of λ_{res} for 11 different single QDs with estimated error bars, for resolutions of 1.5 nm and 3.3 nm respectively. Most of the measured points lie below the shaded region because the resolution limit of the OMA did not allow the true peak amplitude to be measured leading to an underestimate of the EF.

The true EF was estimated by performing an effective deconvolution with the instrument response function of the OMA, as explained in Ref. [52]. The black circles in Fig. 46(c) show the estimated true EFs. It should be noted that essentially all the points lie inside the shaded region within the experimental errors.

The good agreement between numerical simulations and experiments allowed the use of numerical results to estimate the experimental Purcell factor. As in Ref. [52], they perform two different estimates. The maximum measured EF as seen in Fig. 46(c) is $E = 15 \pm 3$ for a wavelength of $\lambda_{\text{res}} = 785$ nm. From the simulation results this value of EF corresponds to a Purcell factor for a y-polarized dipole emitter F_{P}^y and the channeling efficiency into the nanofiber guided modes η_c^y of 7 and 0.65 respectively.

The second estimate was made as follows [52]: In the Purcell regime the Purcell factor may be approximated as $F_{\text{P}} \approx (4/\pi)PF_c$, where $P = \gamma_g^{(0)}/\Gamma_0$ and where F_c is the cavity finesse. Taking $P = 0.2$ at $\lambda_{\text{res}} = 785$ nm, as calculated by simulations, and $F_c = 28 \pm 1$ as calculated from the experimentally measured

y-mode FWHM, the simulation value for cavity length and assuming a nanofiber effective refractive index of 1.19, they found a value $F_{\text{P}}^y = 6.9 \pm 0.2$ [52]. This is in good agreement with the simulation results discussed in the previous paragraph.

Purcell enhancement of a quantum emitter coupled to a nanofiber cavity was also realized by Schell *et al* in reference [157] using an FIB fabricated, defect mode nanofiber cavity as discussed in the previous subsection. In that work, EFs of up to 3 were measured.

6.4. Demonstration of the strong-coupling regime using a nanofiber cavity

We now consider the use of nanofiber cavities to achieve the strong coupling regime of cavity QED. Unlike the results in the previous subsection, the strong coupling regime has so far been demonstrated in relatively long cavities (cavity lengths of 10-200 centimeters) using either standard fiber Bragg gratings with a nanofiber region spliced in between [54] or a ring cavity [111]. We review these results below.

First, Kato and Aoki used the above-mentioned FBG cavity system to reach the strong coupling regime for a single atom trapped near an optical nanofiber [54]. They realized a cavity of 33 cm by splicing commercial FBGs to a tapered optical fiber with nanofiber waist of 400 nm diameter. Using such a cavity they realized a finesse of 40 for a cavity mode with linewidth 6.4 MHz. Further they implemented a two-color magic wavelength trap for laser-cooled Cs atoms using guided modes of the nanofiber. The atoms were trapped around 170 nm from the nanofiber surface in a potential of depth 210 μK. By controlling the density of laser cooled atoms around the nanofiber they realized a trapped atom number down to the single atom level.

In order to probe the atom-cavity coupling they measured the transmission spectrum using a weak probe field. However the single atom events were probabilistic and atoms were trapped at random positions within the cavity relative to the cavity antinodes. For this reason, they used a two step probing technique and post-processing data analysis to determine the atom-cavity coupling. After the loading sequence they sent two probe pulses with power < 1 pW and pulse width of several milliseconds. The first probe pulse (detection probe) was resonant to the atom and the second probe pulse had a variable detuning (spectroscopy probe). When the cavity is resonant with the atom and the atom is positioned at the antinode the resonant probe pulse transmission will strongly reduce due to the normal mode splitting. Therefore the transmission of the detection probe determined the coupling condition for the spectroscopy

probe.

Using data post-processing, based on the attenuation of the detection probe, they delineated six regimes i)-vi) corresponding to the strength of coupling to the cavity, as shown in the left pannel of Fig. 47(a). The corresponding transmission spectra are shown in the right pannel of Fig. 47(a). The observed absorption spectrum in each regime has different behavior. In the strongest probe attenuation regime vi), clear splitting associated with the strong coupling regime of cavity QED was observed. In this regime the atom-photon coupling parameter was found to be 7.8 MHz. In order to confirm the observed splitting was due to a single atom, they measured the spectrum for different trap loading times. By reducing the trap loading time the probability of the events reduced but the splitting remained the same. From this they concluded that the observed normal mode splitting was due to single atoms. They measured a trap lifetime of 11 ms under these settings.

Second, Ruddell *et al* used a 1.4 meter length fiber ring cavity with a nanofiber portion to realize strong coupling of multiple atoms to a nanofiber cavity [111]. The ring cavity mode resonant with the atomic resonance was found to have a finesse of 35 and a linewidth of 2.17 MHz. They achieved thermal tuning of the cavity by sending an off-resonant laser at 780 nm through the nanofiber and used this technique to stabilize the cavity mode to the atom resonance. By overlapping a laser-cooled atom cloud with the nanofiber cavity they probed the transmission spectrum of the atom-cavity system. The measured transmission spectra for different probe powers are shown in Fig. 47(b). For low probe powers they observed a large splitting ($\sim$ 20 MHz) of the cavity resonance. They attributed the splitting to the collective enhancement by an ensemble of atoms interacting with the cavity mode, as the average single-atom-cavity coupling rate was not high enough to cause the splitting alone in this setting. For higher probe powers the splitting was reduced and after a certain power threshold was exceeded, the response became the same as that of an empty cavity Fig. 47(b)(iv). From this saturation behavior they estimated an effective atom-photon coupling rate of 0.6 MHz and a net cooperativity of 1.5 for an effective atom number of 64.

The two realizations of strong coupling of Cs atoms to a nanofiber cavity discussed above involve cavities with large length which are typically suited to strong coupling applications. From the preceding section, we may expect higher cooperativities and couplings both in the strong and Purcell regime if atoms are coupled to cavities with cavities fabricated in the nanofiber region itself.
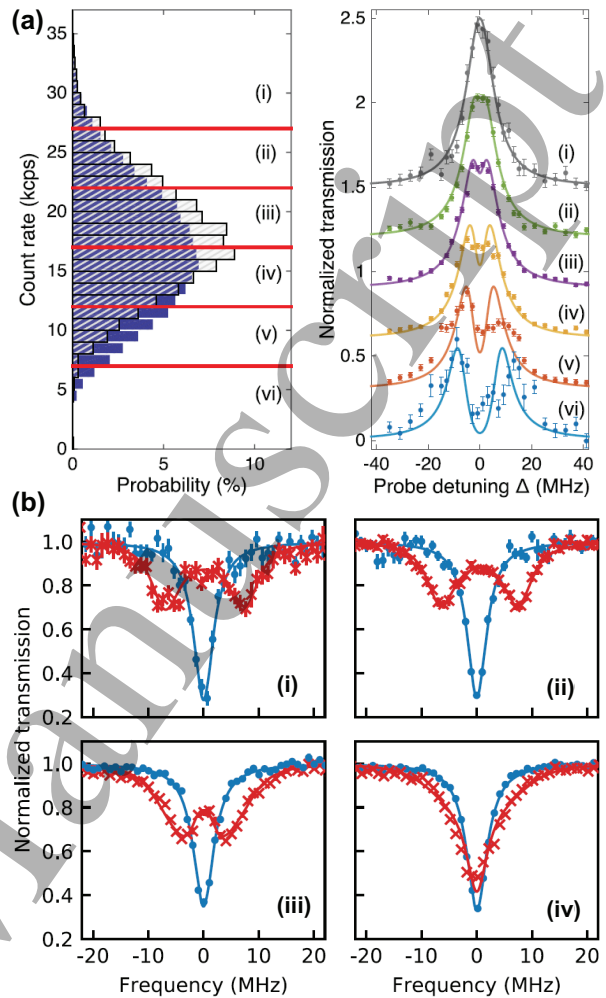
Figure 47. (Color online) (a) (Adapted from Ref. [54] with permission). Left Pannel: Histogram of the transmission intensity of the detection probe with (blue) and without (gray) the optical molasses. Right Pannel: Transmission spectra through the nanofiber Bragg cavity for the regimes (i)-(vi) as discussed in the text. (b) (Adapted from Ref. [111] with permission). In each case, red lines show transmission spectra through the nanofiber ring cavity in the presence of atoms, while blue lines show the transmission spectra for the same condition but without atoms. The panels correspond to probe powers of (i) 30 pW, (ii) 60 pW, (iii) 750 pW, and (iv) 2.3 nW.

7. Summary and outlook

For more than one decade, optical nanofiber technology has experienced significant development and wide ranging popularity in various fields including quantum optics. This is principally due to the technical simplicity, scientific elegance and practical significance of the technique. In particular, optical nanofibers have opened promising new avenues for quantum photonics.

Detailed theoretical investigations, promptly followed by (or motivated by) experimental demonstrations have formed a strong foundation for understand-

ing the atom-photon interaction around the nanofiber. High quality nanofibers are now routinely fabricated in various groups using fiber tapering technology. Integrating laser-cooled atoms and various solid-state emitters with nanofibers is also well established. Single quantum emitters on nanofibers have been well investigated using photon correlation and laser spectroscopy techniques. Fabrication of high quality nanofiber cavities of various types has also been achieved.

In the context of quantum photonics the key issues are single photon generation, storage and manipulation. The measurement of channeling efficiency into nanofiber guided modes and demonstration of Purcell enhancement using a nanofiber cavity are essential rudimentary steps towards efficient single photon generation. Further developments are necessary to realize solid-state emitters with narrow emission lines and high quantum efficiency. Extension of nanofiber-based cavity QED experiments with an efficient solid-state emitter under a cryogenic environment is an essential requirement for fiber-inline single photon sources.

The demonstration of EIT-based single photon storage in nanofiber-trapped atoms is a major step toward quantum nonlinear optics with multiple emitters. However, the storage time and retrieval efficiencies are far below the practical requirements. The storage and retrieval efficiencies can be further improved by implementing nanofiber cavities. However, a major challenge is to improve the coherence properties of the trapped atomic ensemble.

On the other hand, demonstration of the strong-coupling regime with trapped single-atoms in a nanofiber cavity has opened a promising approach for quantum nonlinear optics with single emitters. However, the observed single atom events are quite rare. Deterministic preparation of single atoms trapped at the antinode of the nanofiber cavity is an essential requirement for this approach. In this direction, an optical tweezer based side-illuminated nanofiber trap may provide a better solution.

Based on the above developments, it is possible to demonstrate a single photon switch and two-qubit quantum gates to create atom-photon and photon-photon entanglement in a nanofiber based system. In order to extend such a system as a quantum node, demonstration of atom-atom entanglement connecting two quantum nodes is essential. Additionally, atom-atom entanglement distributed over multiple atoms in the same quantum node will further enhance the capabilities of the node.

In this context, nanofiber mediated long-range dipole-dipole interaction between atoms may offer promising possibilities to implement collective superradiance and many-body effects. The recent demonstration of Bragg reflection from nanofiber trapped atoms

and collective strong-coupling in nanofiber cavities are preliminary steps in this direction. Furthermore the recent demonstrations of the chiral nature of light-matter interaction in nanofibers may offer unprecedented functionality for complex quantum networks.

In only a decade, the field of nanofiber quantum photonics has shown significant development and popularity. However, we believe that this is just the beginning and the field awaits a vast expansion in the near future. We hope this review will be a good starting point for the new players in this field.

Appendix A. Light propagation in step-index optical fibers
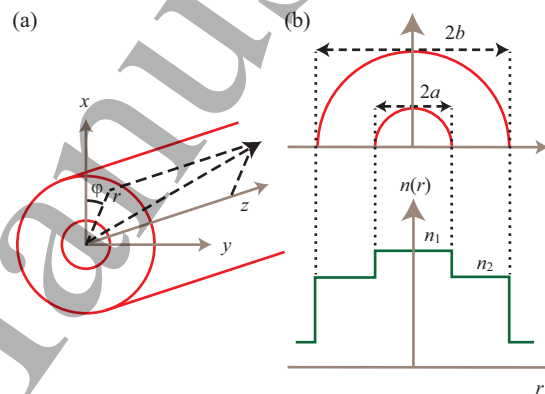
Figure A1. a) Geometry of a standard glass fiber and b) the profile of its refractive index as a function of the radial distance r. In practice, we have $b \gg a$.

A typical step-index optical fiber has a cylindrical doped silica core of radius a and and refractive index n_1 and a cylindrical silica cladding of radius b and refractive index n_2, where $n_2 < n_1$ (figure A1). We use the Cartesian coordinates (x, y, z) as well as the cylindrical coordinates (r, φ, z), where r and φ are the polar coordinates in the fiber transverse plane and z is the coordinate along the fiber axis. We consider a light field of wavelength λ, frequency ω and free-space wave number $k = 2\pi/\lambda = \omega/c$ propagating in the fiber. We assume that the cladding radius b is large as compared to the core radius a and the light wavelength λ. Then, we can use the limit $b = \infty$ and write the refractive index $n = n(r, \varphi, z)$ of the medium as

$$n(r, \varphi, z) = n(r) = \begin{cases} n_1 & \text{if } r < a, \\ n_2 & \text{if } r > a. \end{cases} \quad (A.1)$$

The dielectric constant ϵ is related to the refractive index n as $\epsilon = n^2 \epsilon_0$, where ϵ_0 is the dielectric constant of free space. Since the materials of optical waveguides are normally nonmagnetic, we assume that the magnetic permeability is equal to the free-space value μ_0. In addition, we assume that the medium is

source-free. In view of the very low losses of silica in the wavelength range of interest, we neglect material absorption. Under these conditions, the Maxwell's equations for the electric field $\mathbf{E}$ and the magnetic field $\mathbf{H}$ take the form [166]

$$\nabla \times \mathbf{E} = -\mu_0 \frac{\partial \mathbf{H}}{\partial t},$$

$$\nabla \times \mathbf{H} = \epsilon \frac{\partial \mathbf{E}}{\partial t},$$

$$\nabla \cdot (\epsilon \mathbf{E}) = 0,$$

$$\nabla \cdot \mathbf{H} = 0. \tag{A.2}$$

When the refractive index n does not vary with distance z along the fiber axis, it is convenient to express the electric and magnetic fields as a superposition of fields in modes with the separable form [57, 58, 59]

$$\left[\begin{array}{c} \mathbf{E}(r,\varphi,z,t) \\ \mathbf{H}(r,\varphi,z,t) \end{array} \right] = \frac{1}{2} \left[\begin{array}{c} \boldsymbol{\mathcal{E}}(r,\varphi) \\ \boldsymbol{\mathcal{H}}(r,\varphi) \end{array} \right] \mathrm{e}^{-\mathrm{i}(\omega t - \beta z)} + \mathrm{c.c.}, \tag{A.3}$$

where ω and β are the frequency and propagation constant of a mode, respectively, and $\boldsymbol{\mathcal{E}}$ and $\boldsymbol{\mathcal{H}}$ are the complex amplitudes of the electric and magnetic components, respectively, of the field in the mode.

We use the notations

$$\left[\begin{array}{c} \boldsymbol{\mathcal{E}} \\ \boldsymbol{\mathcal{H}} \end{array} \right] = \left[\begin{array}{c} \mathbf{e} \\ \mathbf{h} \end{array} \right] \exp(\mathrm{i}l\varphi). \tag{A.4}$$

We decompose the mode amplitudes into radial, azimuthal and axial components denoted by subscripts r, φ and z, respectively. Then, we have $e_z = AJ_l(hr)$ and $h_z = BJ_l(hr)$ for the inside of the core ($r < a$) and $e_z = CK_l(qr)$ and $h_z = DK_l(qr)$ for the outside of the core ($r > a$). Here the parameters

$$h = (n_1^2 k^2 - \beta^2)^{1/2} \tag{A.5}$$

and

$$q = (\beta^2 - n_2^2 k^2)^{1/2} \tag{A.6}$$

characterize the fields inside and outside the fiber, respectively. The transverse components e_r, e_φ, h_r and h_φ can be expressed in terms of e_z and h_z. The results are summarized below:

For $r < a$, we find

$$e_r = \frac{\beta}{h} \left[\mathrm{i}AJ_l'(hr) - \frac{\omega\mu_0 l}{\beta} B \frac{J_l(hr)}{hr} \right],$$

$$e_\varphi = -\frac{\beta}{h} \left[lA \frac{J_l(hr)}{hr} + \frac{\mathrm{i}\omega\mu_0}{\beta} BJ_l'(hr) \right],$$

$$e_z = AJ_l(hr), \tag{A.7}$$

and

$$h_r = \frac{\beta}{h} \left[\mathrm{i}BJ_l'(hr) + \frac{\omega\epsilon_1 l}{\beta} A \frac{J_l(hr)}{hr} \right],$$

$$h_\varphi = -\frac{\beta}{h} \left[lB \frac{J_l(hr)}{hr} - \frac{\mathrm{i}\omega\epsilon_1}{\beta} AJ_l'(hr) \right],$$

$$h_z = BJ_l(hr), \tag{A.8}$$

where $J_l'(x) = \mathrm{d}J_l(x)/\mathrm{d}x$ is the derivative of $J(x)$ with respect to the argument x and $\epsilon_1 = n_1^2 \epsilon_0$ is the dielectric constant for the core.

For $r > a$, we obtain

$$e_r = -\frac{\beta}{q} \left[\mathrm{i}CK_l'(qr) - \frac{\omega\mu_0 l}{\beta} D \frac{K_l(qr)}{qr} \right],$$

$$e_\varphi = \frac{\beta}{q} \left[lC \frac{K_l(qr)}{qr} + \frac{\mathrm{i}\omega\mu_0}{\beta} DK_l'(qr) \right],$$

$$e_z = CK_l(qr), \tag{A.9}$$

and

$$h_r = -\frac{\beta}{q} \left[\mathrm{i}DK_l'(qr) + \frac{\omega\epsilon_2 l}{\beta} C \frac{K_l(qr)}{qr} \right],$$

$$h_\varphi = \frac{\beta}{q} \left[lD \frac{K_l(qr)}{qr} - \frac{\mathrm{i}\omega\epsilon_2}{\beta} CK_l'(qr) \right],$$

$$h_z = DK_l(qr), \tag{A.10}$$

where $K_l'(x) = \mathrm{d}K_l(x)/\mathrm{d}x$ is the derivative of $K(x)$ with respect to the argument x and $\epsilon_2 = n_2^2 \epsilon_0$ is the dielectric constant for the cladding.

The normalization constants A, B, C and D as well as the propagation constant β are related to each other by the boundary conditions. The tangential components $e_{\varphi,z}$ and $h_{\varphi,z}$ are continuous at the core-cladding boundary. These conditions together with (A.7)–(A.10) yield the fiber eigenvalue equation

$$\left[\frac{J_l'(ha)}{haJ_l(ha)} + \frac{K_l'(qa)}{qaK_l(qa)} \right] \left[\frac{n_1^2 J_l'(ha)}{haJ_l(ha)} + \frac{n_2^2 K_l'(qa)}{qaK_l(qa)} \right]$$

$$= l^2 \left(\frac{1}{h^2 a^2} + \frac{1}{q^2 a^2} \right)^2 \frac{\beta^2}{k^2}, \tag{A.11}$$

which determines the propagation constant β for each guided mode. The coefficients B, C and D are related to the coefficient A as

$$\frac{C}{A} = \frac{J_l(ha)}{K_l(qa)},$$

$$\frac{B}{A} = \frac{\mathrm{i}\beta l}{\omega\mu_0} \left(\frac{1}{h^2 a^2} + \frac{1}{q^2 a^2} \right) \left[\frac{J_l'(ha)}{haJ_l(ha)} + \frac{K_l'(qa)}{qaK_l(qa)} \right]^{-1},$$

$$\frac{D}{A} = \frac{C B}{A^2}. \tag{A.12}$$

The coefficient A can be determined by accounting for the energy flux in the z direction.

The index $l = 0, \pm 1, \pm 2, \ldots$ in the above equations stems from the ansatz (A.4) for the mode functions in the cylindrical coordinates. The sign $+$ or $-$ of l refers to the solution with left- or right-handed circulation of the transverse field around the fiber axis. For convenience, we can label two different modes of the opposite orders l and $-l$ by using the same index l and adding a polarization index $p = +1$ or -1. The solution for a quasilinearly polarized light $\mathbf{E}^{\mathrm{lin}}$ can be composed as a superposition of left- and right-handed circular fields $\mathbf{E}^{\mathrm{left}}$ and $\mathbf{E}^{\mathrm{right}}$, that is,

$$\mathbf{E}^{\mathrm{lin}} = \frac{1}{\sqrt{2}} (\mathbf{E}^{\mathrm{left}} \mathrm{e}^{-\mathrm{i}\varphi_0} + \mathbf{E}^{\mathrm{right}} \mathrm{e}^{\mathrm{i}\varphi_0}). \tag{A.13}$$

Nanofiber quantum photonics   45

Here the angle φ_0 specifies the direction of the polarization vector.

We now discuss the solutions of the fiber eigenvalue equation (A.11) for the propagation constant β and the properties of the associated modes. We solve (A.11) for $J'_l(ha)/haJ_l(ha)$ and use the relation $J'_l(x) = -J_{l+1}(x) + (l/x)J_l(x) = J_{l-1}(x) - (l/x)J_l(x)$ to rearrange the result. Then, we obtain two sets of eigenvalue equations, namely,

HE modes:

$$\frac{J_{l-1}(ha)}{haJ_l(ha)} = -\frac{n_1^2 + n_2^2}{2n_1^2}\frac{K'_l(qa)}{qaK_l(qa)} + \frac{l}{h^2a^2} - R, \quad \text{(A.14)}$$

EH modes:

$$\frac{J_{l+1}(ha)}{haJ_l(ha)} = \frac{n_1^2 + n_2^2}{2n_1^2}\frac{K'_l(qa)}{qaK_l(qa)} + \frac{l}{h^2a^2} - R, \quad \text{(A.15)}$$

with

$$R = \left[\left(\frac{n_1^2 - n_2^2}{2n_1^2}\right)^2\left(\frac{K'_l(qa)}{qaK_l(qa)}\right)^2 \right.$$
$$\left. + \left(\frac{l\beta}{n_1k}\right)^2\left(\frac{1}{q^2a^2} + \frac{1}{h^2a^2}\right)^2\right]^{1/2}. \quad \text{(A.16)}$$

Equations (A.14) and (A.15) can be solved graphically by plotting each side as a function of ha using $qa = \sqrt{(n_1^2 - n_2^2)(ka)^2 - (ha)^2}$. When $l \neq 0$, equations (A.14) and (A.15) correspond to the HE and EH modes, respectively. If the eigenvalues for HE (EH) modes with a given value $l \neq 0$ are β_m, where $m = 1, 2, 3, \ldots$, then the modes are designated as HE_{lm} (EH_{lm}). In the special case where $l = 0$, equations (A.14) and (A.15) correspond to the TE and TM modes, respectively. If the eigenvalues for TE (TM) modes are β_m, where $m = 1, 2, 3, \ldots$, then the modes are designated as TE_{0m} (TM_{0m}).

Confined modes require that q be real to achieve an exponential decay of the field in the cladding. Therefore, we need to consider only ha in the range $0 \leq ha \leq V$, where

$$V = ka\sqrt{n_1^2 - n_2^2}. \quad \text{(A.17)}$$

At the point $ha = V$, we have $qa = 0$ and hence $K_l(qa) = \infty$. Consequently, the point $ha = V$ is the position of the singularity of the right-hand sides of (A.14) and (A.15). For a given l, the number of solutions is determined by the position of the singularity of the right-hand sides of (A.14) and (A.15), that is, by the point $ha = V$. The parameter V is hence the characteristic size parameter for the fiber.

We note that the HE_{11} mode always exists regardless of the value of V. This means that the HE_{11} mode does not have a cut-off. However, all other modes have cut-off values. At the cut-off for a mode, the propagation constant of the mode β takes the value $\beta = kn_2$, yielding $q = 0$. As the mode

approaches its cut-off, the field penetrates deeply into the cladding medium and the mode is poorly confined and poorly guided. Below the cut-off value $V_c \cong 2.405$ only the mode HE_{11}, called the fundamental mode, can propagate. Thus, the single-mode condition is $V \equiv ka\sqrt{n_1^2 - n_2^2} \leq V_c \cong 2.405$.

For many applications requiring a well-defined phase front of the propagating light (e.g. telecommunication, interferometry etc.), single-mode operation is compulsory. In nanofiber photonics, we are interested in the situations where the fields are tightly confined in the fiber transverse plane. Such situations may occur only in the singe-mode regime. Therefore, below we discuss only the HE_{11} mode.

We consider a fundamental mode with quasicircular polarization. In the cylindrical coordinates, the solutions of Maxwell's equations for the cylindrical components of the electric field amplitude $\boldsymbol{\mathcal{E}}$ in such a mode are given by [57, 58, 59]

$$\begin{aligned}
\mathcal{E}_r &= e_r e^{\pm i\varphi}, \\
\mathcal{E}_\varphi &= \pm e_\varphi e^{\pm i\varphi}, \\
\mathcal{E}_z &= e_z e^{\pm i\varphi}.
\end{aligned} \quad \text{(A.18)}$$

Here the functions e_j ($j = r, \varphi, z$) describe the radial dependences of the field components. They are defined, for $r < a$, as

$$\begin{aligned}
e_r &= iA\frac{\beta}{2h}[(1 - s)J_0(hr) - (1 + s)J_2(hr)], \\
e_\varphi &= -A\frac{\beta}{2h}[(1 - s)J_0(hr) + (1 + s)J_2(hr)], \\
e_z &= AJ_1(hr),
\end{aligned} \quad \text{(A.19)}$$

and, for $r > a$, as

$$\begin{aligned}
e_r &= iA\frac{\beta}{2q}\frac{J_1(ha)}{K_1(qa)}[(1 - s)K_0(qr) + (1 + s)K_2(qr)], \\
e_\varphi &= -A\frac{\beta}{2q}\frac{J_1(ha)}{K_1(qa)}[(1 - s)K_0(qr) - (1 + s)K_2(qr)], \\
e_z &= A\frac{J_1(ha)}{K_1(qa)}K_1(qr).
\end{aligned} \quad \text{(A.20)}$$

The upper (lower) sign in (A.18) corresponds to the counterclockwise (clockwise) circulation of the azimuthal phase around the z axis. It is clear that the total intensity $|\mathcal{E}|^2$ of the electric field is independent of the azimuthal angle φ. We note that the complex quadratures $\mathcal{E}_r$ and $\mathcal{E}_\varphi$ have a difference of $\pi/2$ between their phases. Therefore, the polarization of the total transverse component of the field is elliptical (or circular).

The normalized profile functions for quasilinearly polarized guided modes are given as

$$\begin{aligned}
\mathbf{e}^{(\omega fx)} &= \sqrt{2}(\hat{\mathbf{r}}e_r\cos\varphi + i\hat{\boldsymbol{\varphi}}e_\varphi\sin\varphi + f\hat{\mathbf{z}}e_z\cos\varphi), \\
\mathbf{e}^{(\omega fy)} &= \sqrt{2}(\hat{\mathbf{r}}e_r\sin\varphi - i\hat{\boldsymbol{\varphi}}e_\varphi\cos\varphi + f\hat{\mathbf{z}}e_z\sin\varphi)\quad\text{(A.21)}
\end{aligned}$$

Appendix B. Radiation modes of a nanofiber

We present the electric component of the field in the form $\mathbf{E} = (1/2)(\boldsymbol{\mathcal{E}}\mathrm{e}^{-\mathrm{i}\omega t}+\mathrm{c.c.})$, where $\boldsymbol{\mathcal{E}}$ is the envelope. For a radiation mode with a propagation constant β in the range $-kn_2 < \beta < kn_2$ and a mode order $m = 0, \pm 1, \pm 2, \ldots$, we can write $\boldsymbol{\mathcal{E}} = \mathbf{e}\mathrm{e}^{\mathrm{i}\beta z+\mathrm{i}m\varphi}$, where $\mathbf{e}$ is the mode profile function. The characteristic parameters for the field in the inside and outside of the fiber are $h = \sqrt{k^2 n_1^2 - \beta^2}$ and $q = \sqrt{k^2 n_2^2 - \beta^2}$, respectively.

The mode functions of the electric parts of the radiation modes $\nu = (\omega\beta mp)$ [57, 58, 59] are given, for $r < a$, by

$$e_r^{(\nu)} = \frac{\mathrm{i}}{h^2}\left[\beta h A J_m'(hr) + \mathrm{i}m\frac{\omega\mu_0}{r}BJ_m(hr)\right],$$
$$e_\varphi^{(\nu)} = \frac{\mathrm{i}}{h^2}\left[\mathrm{i}m\frac{\beta}{r}AJ_m(hr) - h\omega\mu_0 BJ_m'(hr)\right],$$
$$e_z^{(\nu)} = AJ_m(hr), \tag{B.1}$$

and, for $r > a$, by

$$e_r^{(\nu)} = \frac{\mathrm{i}}{q^2}\sum_{j=1,2}\left[\beta q C_j H_m^{(j)\prime}(qr) + \mathrm{i}m\frac{\omega\mu_0}{r}D_j H_m^{(j)}(qr)\right],$$
$$e_\varphi^{(\nu)} = \frac{\mathrm{i}}{q^2}\sum_{j=1,2}\left[\mathrm{i}m\frac{\beta}{r}C_j H_m^{(j)}(qr) - q\omega\mu_0 D_j H_m^{(j)\prime}(qr)\right],$$
$$e_z^{(\nu)} = \sum_{j=1,2}C_j H_m^{(j)}(qr). \tag{B.2}$$

Here A and B as well as C_j and D_j with $j = 1,2$ are coefficients. The coefficients C_j and D_j are related to the coefficients A and B as [63]

$$C_j = (-1)^j\frac{\mathrm{i}\pi q^2 a}{4n_2^2}(AL_j + \mathrm{i}\mu_0 cBV_j),$$

$$D_j = (-1)^{j-1}\frac{\mathrm{i}\pi q^2 a}{4}(\mathrm{i}\epsilon_0 cAV_j - BM_j), \tag{B.3}$$

where

$$V_j = \frac{mk\beta}{ah^2 q^2}(n_2^2 - n_1^2)J_m(ha)H_m^{(j)*}(qa),$$

$$M_j = \frac{1}{h}J_m'(ha)H_m^{(j)*}(qa) - \frac{1}{q}J_m(ha)H_m^{(j)*\prime}(qa),$$

$$L_j = \frac{n_1^2}{h}J_m'(ha)H_m^{(j)*}(qa) - \frac{n_2^2}{q}J_m(ha)H_m^{(j)*\prime}(qa). \tag{B.4}$$

We specify two polarizations by choosing $B = \mathrm{i}\eta A$ and $B = -\mathrm{i}\eta A$ for $p = +$ and $p = -$, respectively. We take A to be a real number. The orthogonality of the modes requires

$$\int_0^{2\pi}d\varphi\int_0^\infty n_{\mathrm{ref}}^2\left[\mathbf{e}^{(\nu)}\mathbf{e}^{(\nu')*}\right]_{\beta=\beta',m=m'} rdr$$
$$= N_\nu\delta_{pp'}\delta(\omega-\omega'). \tag{B.5}$$

This leads to

$$\eta = \epsilon_0 c\sqrt{\frac{n_2^2|V_j|^2 + |L_j|^2}{|V_j|^2 + n_2^2|M_j|^2}}. \tag{B.6}$$

The constant N_ν is given by

$$N_\nu = \frac{8\pi\omega}{q^2}\left(n_2^2|C_j|^2 + \frac{\mu_0}{\epsilon_0}|D_j|^2\right). \tag{B.7}$$

Appendix C. Theoretical formulation of optical trapping potential using guided modes of nanofiber

The guided modes of an optical nanofiber can have very different properties compared with simple beams in free space for which the paraxial approximation holds. For example, the appearance of a longitudinal component of the field (also present in strongly focused laser beams) is one of the most striking features of tightly confined light. Experiments in both non-paraxial dipole traps [167, 168] and traps formed in the evanescent field of a nanofiber [37, 38] have led to important discussions regarding the coherence properties of atoms in such tight optical traps.

In this subsection, we give a theoretical background of trapping atoms. We present the scattering rate and dipole force in the near-resonance and far-of-resonance cases. We discuss two-level atoms, multilevel atoms, the AC-Stark shift and the surface–atom interaction. We also calculate numerically optical potentials in a nanofiber-based trap.

Appendix C.1. Interaction of a classical dipole oscillator with a light field

The interaction of a monochromatic light field and a neutral atom is well described by the Lorentz model [166]. In this model, the atom is reduced to a classical harmonic oscillator consisting of an electron (mass m_e, charge $-e$) bound to a massive core by a harmonic potential. In the presence of a light field, the displacement $\mathbf{r}$ of the electron from its mean position is governed by the equation [166]

$$\ddot{\mathbf{r}}(t) + \gamma\dot{\mathbf{r}}(t) + \omega_0^2\mathbf{r}(t) = -\frac{e}{m_e}\mathbf{E}(t), \tag{C.1}$$

where ω_0 is the angular frequency of the oscillator, $\mathbf{E}$ is the electric component of the field, and $\gamma = e^2\omega_0^2/6\pi\epsilon_0 m_e c^3$ is the energy dissipation rate due to classical dipole radiation. In the above equation, we have neglected the magnetic force, which is small for non-relativistic motion of the electron in the atom.

We consider a monochromatic driving field $\mathbf{E} = (\boldsymbol{\mathcal{E}}\mathrm{e}^{-\mathrm{i}\omega t} + \mathrm{c.c.})/2$. Here ω and $\boldsymbol{\mathcal{E}}$ are the angular frequency and complex amplitude of the field. We write $\mathbf{r} = (\mathbf{u}\mathrm{e}^{-\mathrm{i}\omega t} + \mathrm{c.c.})/2$, where $\mathbf{u}$ is the complex

Nanofiber quantum photonics   47

displacement amplitude. In the stationary regime, the solution for **u** is

$$\mathbf{u} = -\frac{\alpha}{e}\boldsymbol{\mathcal{E}}, \tag{C.2}$$

where

$$\alpha = \frac{e^2}{m_e} \frac{1}{\omega_0^2 - \omega^2 - i\gamma\omega} \tag{C.3}$$

is the complex polarizability of the atom. It is clear that the complex amplitude $\wp = -e\mathbf{u}$ of the induced dipole moment $\mathbf{d} = -e\mathbf{r} = (\wp e^{-i\omega t} + \text{c.c.})/2$ is determined by the expression $\wp = \alpha\boldsymbol{\mathcal{E}}$.

The time-averaged power absorbed by the atom is the work that the field does on the induced dipole and is given by

$$P = \overline{\dot{\mathbf{d}}(t) \cdot \mathbf{E}(t)} = \frac{\omega|\mathcal{E}|^2}{2}\text{Im}[\alpha]. \tag{C.4}$$

In the classical picture, the energy of the driving field is dissipated continuously. However, in the quantum mechanical picture the photons in the driving field are scattered by the atom. The scattering rate is

$$\Gamma_{\text{scatt}} = \frac{P}{\hbar\omega} = \frac{|\mathcal{E}|^2}{2\hbar}\text{Im}[\alpha]. \tag{C.5}$$

For a classical dipole oscillator, we find

$$\Gamma_{\text{scatt}} = \frac{e^2}{c\epsilon_0\hbar m_e}\frac{\gamma\omega}{(\omega_0^2 - \omega^2)^2 + \gamma^2\omega^2}I. \tag{C.6}$$

The time-averaged optical potential of the induced dipole moment **d** interacting with the driving electric field **E** is given by

$$U = -\frac{1}{2}\overline{\mathbf{d}(t) \cdot \mathbf{E}(t)} = -\frac{1}{4}|\mathcal{E}|^2\text{Re}[\alpha]. \tag{C.7}$$

Here the first factor of $1/2$ accounts for the fact that the dipole moment is induced and another $1/2$ for the cycle average of the squared electric field modulus. The optical dipole force exerted on the atom is given by the well-known classical formula

$$\mathbf{F} = -\nabla U(\mathbf{r}). \tag{C.8}$$

For a classical dipole oscillator, we find

$$U(\mathbf{r}) = -\frac{e^2}{2c\epsilon_0 m_e}\frac{\omega_0^2 - \omega^2}{(\omega_0^2 - \omega^2)^2 + \gamma^2\omega^2}I(\mathbf{r}). \tag{C.9}$$

Appendix C.2. Interaction of a two-level atom with a near-resonant field

Note that the classical dipole oscillator is not a quantum system. Moreover, a quantum harmonic oscillator has an infinitely large number of equidistant energy levels. In a semiclassical approach, the atom is considered as a two-level quantum system interacting with a classical field. We denote the upper and lower levels of the atom by the notations $|2\rangle$ and $|1\rangle$, respectively. The quantum state of the atom is described by the density matrix $\rho_{ij} = \langle i|\hat{\rho}|j\rangle$, where

$i, j = 1, 2$. We use the dipole and rotating-wave approximations. The time evolution of the atomic population difference $w = \rho_{22} - \rho_{11}$ and the atomic coherence $\xi = \rho_{21}e^{i\omega t}$ is governed by the optical Bloch equations [169]

$$\begin{aligned}\dot{w} &= -\gamma(w+1) + i(\Omega\xi^* - \Omega^*\xi),\\ \dot{\xi} &= (i\Delta - \gamma/2)\xi - (i\Omega/2)w,\end{aligned} \tag{C.10}$$

where $\Omega = d_\parallel\mathcal{E}/\hbar$ is the Rabi frequency, $\Delta = \omega - \omega_0$ is the detuning of the field and $\gamma = \omega_0^3 d^2/3\pi\epsilon_0\hbar c^3$ is the decay rate of the excited state. Here d is the magnitude of the dipole moment of the atom and $d_\parallel$ is the magnitude of the projection of the atomic dipole moment onto the polarization vector of the electric field component.

The positive frequency component of the induced dipole moment is $\wp = 2d_\parallel^*\xi = \alpha\mathcal{E}$, where α is the polarizability of the atom. In the stationary regime, we have [169]

$$\alpha = -\frac{2|d_\parallel|^2}{\hbar\gamma^2}\frac{2\Delta - i\gamma}{1 + I/I_0 + (2\Delta/\gamma)^2}, \tag{C.11}$$

where $I = c\epsilon_0|\mathcal{E}|^2/2$ is the intensity of the field and $I_0 = c\epsilon_0\hbar^2\gamma^2/4|d_\parallel|^2$ is the saturation intensity.

For a two-level quantum atom, the scattering rate is found to be

$$\Gamma_{\text{scatt}} = \frac{\gamma}{2}\frac{I/I_0}{1 + I/I_0 + (2\Delta/\gamma)^2}. \tag{C.12}$$

Near to resonance ($\Delta \ll \gamma$) and at strong saturation ($I \gg I_0$), the scattering rate of single atoms can achieve substantial values $\Gamma_{\text{scatt}} \cong \gamma/2$ ($\sim 10^7$photons/s for alkali-metal atoms).

For a two-level quantum atom, the optical potential is found to be

$$U(\mathbf{r}) = \frac{\hbar\Delta}{2}\frac{I(\mathbf{r})/I_0}{1 + I(\mathbf{r})/I_0 + (2\Delta/\gamma)^2}. \tag{C.13}$$

It is clear from the above formula that a red detuning ($\Delta = \omega - \omega_0 < 0$) creates an attractive potential while a blue detuning ($\Delta = \omega - \omega_0 > 0$) creates a repulsive one. That is, for a red detuning, atoms will be attracted to intensity maxima, while for a blue detuning, they will be repelled from intensity maxima.

When we compare (C.12) and (C.13), we find a simple relation

$$\Gamma_{\text{scatt}} = \frac{\gamma}{\hbar\Delta}U. \tag{C.14}$$

In typical trapping applications, we wish to avoid heating of atoms due to scattering while maximizing the trap depth. Such a regime can be realized by using far detuned fields ($|\Delta| \gg \gamma$) at high intensity.

Nanofiber quantum photonics   48

Appendix C.3. Interaction of a two-level atom with a far-off-resonant field

We assume that the detuning $\omega - \omega_0$ is large compared to the atomic decay rate $\gamma = \omega_0^3 d^2 / 3\pi\epsilon_0 \hbar c^3$ and the Rabi frequency $\Omega = d_\parallel \mathcal{E}/\hbar$. In this case, the rotating-wave approximation is not valid and, therefore, we need to take into account counter-rotating terms in the interaction Hamiltonian [170]. The polarizability α of the atom is found to be

$$\alpha = -\frac{|d_\parallel|^2}{\hbar}\left(\frac{1}{\omega - \omega_0 + i\gamma/2} - \frac{1}{\omega + \omega_0 + i\gamma/2}\right). \text{(C.15)}$$

The scattering rate and the optical potential are given as

$$\Gamma_{\text{scatt}} = \frac{|d_\parallel|^2 \gamma \omega}{2c\epsilon_0 \hbar^2 \omega_0}\left(\frac{1}{\omega_0 - \omega} + \frac{1}{\omega_0 + \omega}\right)^2 I,$$

$$U = -\frac{|d_\parallel|^2}{2c\epsilon_0 \hbar}\left(\frac{1}{\omega_0 - \omega} + \frac{1}{\omega_0 + \omega}\right) I. \qquad \text{(C.16)}$$

Appendix C.4. Scalar theory for the polarizability of a multilevel atom

When the detuning of the field is large enough, the two-level model for the atom is not valid anymore. In this case, we need to take into account the multilevel structure of real atoms. In a scalar theory for a multilevel atom with dipole-allowed transitions between the ground state and excited levels, each transition can be approximated as an independent harmonic oscillator. The polarizability of the atom can be constructed as a sum of the contributions of all individual transitions, yielding

$$\alpha = \sum_j f_j \alpha_j. \qquad \text{(C.17)}$$

Here j denotes the transition between the ground state $|g\rangle$ and an excited state $|e\rangle$ and f_j is the oscillator strength of the transition. The relation between the linewidth (decay rate) γ_j and the oscillator strength f_j is

$$f_j = \gamma_j \frac{2\pi\epsilon_0 m_e c^3}{e^2 \omega_j^2}\frac{g_e}{g_g}, \qquad \text{(C.18)}$$

where ω_j denotes the transition frequency of the j transition and g_e and g_g are the degeneracies of the excited and ground states, respectively.

Let us use the fine structure of levels of an alkali atom. Let J and J' be the total angular quantum numbers of the ground state and an excited level, respectively. Then, we have $g_g = 2J + 1$ and $g_e = 2J' + 1$. Hence, expression (C.17) for the complex polarizability of the atom becomes

$$\alpha = 2\pi\epsilon_0 c^3 \sum_j \frac{2J' + 1}{2J + 1}\frac{\gamma_j / \omega_j^2}{\omega_j^2 - \omega^2 - i\gamma_j \omega}. \qquad \text{(C.19)}$$

When we insert the above expression into equations (C.5) and (C.7), we obtain the following expressions for the scattering rate and the optical dipole potential of an alkali atom in the ground state:

$$\Gamma_{\text{scatt}} = \frac{\pi\epsilon_0 c^3}{\hbar}|\mathcal{E}|^2 \sum_j \frac{2J' + 1}{2J + 1}\frac{\gamma_j^2 \omega / \omega_j^2}{(\omega_j^2 - \omega^2)^2 + \gamma_j^2 \omega^2},$$

$$U = -\frac{\pi\epsilon_0 c^3}{2}|\mathcal{E}|^2 \sum_j \frac{2J' + 1}{2J + 1}\frac{(\omega_j^2 - \omega^2)\gamma_j/\omega_j^2}{(\omega_j^2 - \omega^2)^2 + \gamma_j^2 \omega^2}. \qquad \text{(C.20)}$$

Note that the above calculations do not take into account the tensor nature of the atomic energy levels.

Appendix C.5. Tensor theory for the ac-Stark shift

For atom trapping, far-off-resonance lasers are used because they ensure low scattering rates and thus provide a long coherence time. The presence of an intense far-detuned light field shifts the energy levels of the atom. In strongly confining traps the differential light shift of a pair of atomic states leads to a strong position-dependent ac-Stark shift of the atomic transition frequency. We follow [171, 172] to present a general formula for the ac-Stark shift of a multilevel atom interacting with a light field of an arbitrary polarization.

Let us evaluate the energy shifts for the fine-structure state $|nJ\rangle$. The hfs interaction operator V^{hfs} and the Stark interaction operator V^{EE} (expressions for which follow later) shift the atomic energy levels according to the total interaction Hamiltonian

$$H_{\text{int}} = V^{\text{hfs}} + V^{EE}. \qquad \text{(C.21)}$$

Because level mixing may occur, it is necessary to diagonalize H_{int} to find the energy level shifts and thus the optical potential.

The hfs interaction between the electron angular momentum $\mathbf{J}$ and the nuclear spin $\mathbf{I}$ is given by the operator [169]

$$V^{\text{hfs}} = \hbar A_{\text{hfs}} \mathbf{I}\cdot\mathbf{J} + \hbar B_{\text{hfs}}\frac{6(\mathbf{I} \cdot \mathbf{J})^2 + 3\mathbf{I} \cdot \mathbf{J} - 2\mathbf{I}^2\mathbf{J}^2}{2I(2I-1)2J(2J-1)}, \text{(C.22)}$$

where A_{hfs} and B_{hfs} are the hfs constants depending on the fine structure level.

Due to the hfs interaction, the projection J_z of the total electronic angular momentum $\mathbf{J}$ onto the quantization axis z is not conserved. However, in the absence of the external light field, the projection F_z of the total angular momentum of the atom, described by the operator $\mathbf{F} = \mathbf{J} + \mathbf{I}$, onto the quantization axis z is conserved. We use the notation $|nJFM\rangle$ for the atomic hfs basis (F basis) states, where F is the quantum number for the total angular momentum $\mathbf{F}$ of the atom, M is the quantum number for the projection F_z of $\mathbf{F}$ onto the quantization axis z, J is the

quantum number for the total angular momentum $\mathbf{J}$ of the electron, and n is the set of the remaining quantum numbers $\{nLSI\}$, with L and S being the quantum numbers for the total orbital angular momentum and the total spin of the electrons, respectively. In the hfs basis $\{|nJFM\rangle\}$, the operator V^{hfs} is diagonal.

The hfs interaction leads to non-conservation of J_z (The projection of $\mathbf{J}$ onto the quantization axis). However, the projection of the total angular momentum F_z (where $\mathbf{F} = \mathbf{J} + \mathbf{I}$) is conserved, in the absence of an external field. The hfs basis, or F basis, is denoted by the states $|nJFM\rangle$, where F is the quantum number for the total angular momentum $\mathbf{F}$ of the atom, M is the quantum number for the projection F_z of $\mathbf{F}$ onto the quantization axis z, J is the quantum number for the total angular momentum $\mathbf{J}$ of the electron, and n is the set of the remaining quantum numbers $\{nLSI\}$, with L and S being the quantum numbers for the total orbital angular momentum and the total spin of the electrons, respectively. In the hfs basis $\{|nJFM\rangle\}$, the operator V^{hfs} is diagonal.

Next, let us consider an atom interacting with a classical electromagnetic field due to the Stark effect. The light field is given by

$$\mathbf{E} = \frac{1}{2}\boldsymbol{\mathcal{E}}e^{-i\omega t} + \text{c.c.} = \frac{1}{2}\mathcal{E}\mathbf{u}e^{-i\omega t} + \text{c.c.}, \tag{C.23}$$

where ω is the angular frequency, $\boldsymbol{\mathcal{E}} = \mathcal{E}\mathbf{u}$ is the positive-frequency electric field envelope, and $\mathcal{E}$ and $\mathbf{u}$ being the field amplitude and the polarization vector, respectively. Note that $\mathcal{E}$ is a complex scalar and $\mathbf{u}$ is a complex unit vector in general.

If we assume far-detuning of the light relative to the atomic resonance, and that the Stark energy is small relative to the fine structure splitting, then J is a good quantum number, and we can write the Stark operator as follows

$$V^{EE} = \sum_{FMF'M'} V^{EE}_{FMF'M'}|(nJ)FM\rangle\langle(nJ)F'M'|, \tag{C.24}$$

where $V^{EE}_{FMF'M'} \equiv \langle(nJ)FM|V^{EE}|(nJ)F'M'\rangle$ are the matrix elements and are given as [171]

$$V^{EE}_{FMF'M'} = \frac{1}{4}|\mathcal{E}|^2 \sum_{\substack{K=0,1,2 \\ q=-K,\dots,K}} \alpha^{(K)}_{nJ}\{\mathbf{u}^* \otimes \mathbf{u}\}_{Kq}$$
$$\times (-1)^{J+I+K+q-M}\sqrt{(2F+1)(2F'+1)}$$
$$\times \begin{pmatrix} F & K & F' \\ M & q & -M' \end{pmatrix}\begin{Bmatrix} F & K & F' \\ J & I & J \end{Bmatrix}, \tag{C.25}$$

where $|(nJ)FM\rangle \equiv |nJFM\rangle$.

Here we have introduced the notations

$$\alpha^{(K)}_{nJ} = (-1)^{K+J+1}\sqrt{2K+1}$$
$$\times \sum_{n'J'}(-1)^{J'}\begin{Bmatrix} 1 & K & 1 \\ J & J' & J \end{Bmatrix}|\langle n'J'\|\mathbf{d}\|nJ\rangle|^2$$
$$\times \frac{1}{\hbar}\mathrm{Re}\left(\frac{1}{\omega_{n'J'nJ} - \omega - i\gamma_{n'J'nJ}/2}\right.$$

$$\left. + \frac{(-1)^K}{\omega_{n'J'nJ} + \omega + i\gamma_{n'J'nJ}/2}\right), \tag{C.26}$$

with $K = 0, 1, 2$, for the reduced dynamical scalar ($K = 0$), vector ($K = 1$), and tensor ($K = 2$) polarizabilities of the atom in the fine-structure level $|nJ\rangle$. The angular frequency and linewidth of the transition between fine-structure levels $|n'J'\rangle$ and $|nJ\rangle$ are denoted by $\omega_{n'J'nJ} = \omega_{n'J'} - \omega_{nJ}$ and $\gamma_{n'J'nJ} = \gamma_{n'J'} + \gamma_{nJ}$ respectively. Note that the above-defined polarizabilities are the real parts of the complex polarizabilities, with the imaginary parts being related to the scattering rate of the atom [166].

The compound tensor components $\{\mathbf{u}^* \otimes \mathbf{u}\}_{Kq}$ in Eq. (C.25) are defined as

$$\{\mathbf{u}^* \otimes \mathbf{u}\}_{Kq} = \sum_{\mu,\mu'=0,\pm1}(-1)^{q+\mu'}u_\mu u^*_{-\mu'}$$
$$\times \sqrt{2K+1}\begin{pmatrix} 1 & K & 1 \\ \mu & -q & \mu' \end{pmatrix}. \tag{C.27}$$

Here $u_{-1} = (u_x - iu_y)/\sqrt{2}$, $u_0 = u_z$, and $u_1 = -(u_x+iu_y)/\sqrt{2}$ are the spherical tensor components of the polarization vector $\mathbf{u}$ in the Cartesian coordinate frame $\{x, y, z\}$.

We note that the Stark interaction operator (C.24) with the matrix elements (C.25) can be written in the form [171, 173]

$$V^{EE} = -\frac{1}{4}|\mathcal{E}|^2\left\{\alpha^s_{nJ} - i\alpha^v_{nJ}\frac{[\mathbf{u}^* \times \mathbf{u}] \cdot \mathbf{J}}{2J}\right.$$
$$\left. + \alpha^T_{nJ}\frac{3[(\mathbf{u}^* \cdot \mathbf{J})(\mathbf{u} \cdot \mathbf{J}) + (\mathbf{u} \cdot \mathbf{J})(\mathbf{u}^* \cdot \mathbf{J})] - 2\mathbf{J}^2}{2J(2J-1)}\right\} \tag{C.28}$$

Here α^s_{nJ}, α^v_{nJ}, and α^T_{nJ} are the conventional dynamical scalar, vector, and tensor polarizabilities, respectively, of the atom in the fine-structure level $|nJ\rangle$. They are given as [171]

$$\alpha^s_{nJ} = \frac{1}{\sqrt{3(2J+1)}}\alpha^{(0)}_{nJ},$$

$$\alpha^v_{nJ} = -\sqrt{\frac{2J}{(J+1)(2J+1)}}\alpha^{(1)}_{nJ},$$

$$\alpha^T_{nJ} = -\sqrt{\frac{2J(2J-1)}{3(J+1)(2J+1)(2J+3)}}\alpha^{(2)}_{nJ}. \tag{C.29}$$

For the ground states of alkali-metal atoms ($J = 1/2$) the tensor polarizability is zero. Furthermore, for linearly polarized light, $\mathbf{u}$ is real, and $[\mathbf{u}^* \times \mathbf{u}]$ vanishes, so that the vector polarizatbility makes no contribution to the ac Stark shift. Additionally, $\gamma_{n'J'nJ}$ can be omitted from the denominators in Eq. (C.26) in the large detuning limit.

In general, V^{EE} is not diagonal neither in F and nor in M. Therefore, in order to find the new eigenstates and eigenvalues, one has to diagonalize the Hamiltonian (C.21), which includes both the hfs

splitting and the ac Stark interaction. However, in the case where the Stark interaction energy is small compared to the hfs splitting, we can neglect the mixing of atomic energy levels with different quantum numbers F. In this case, the Stark operator V^{EE} for the atom in a particular hfs level $|nJF\rangle$ can be presented in the form [174]

In the most general case, V^{EE} is not diagonal in either the F or M bases. It is therefore necessary to diagonalize the Hamiltonian of Eq. (C.21) to find the new eigenstates and eigen-energies. Nonetheless, if the Stark interaction energy is sufficiently small compared to the hfs splitting, energy level mixing among levels with different F can be neglected allowing the Stark operator for a given hfs level $|nJF\rangle$ to be written in the form [174]

$$V^{EE} = -\frac{1}{4}|\mathcal{E}|^2\left\{\alpha^s_{nJF} - i\alpha^v_{nJF}\frac{[\mathbf{u}^* \times \mathbf{u}] \cdot \mathbf{F}}{2F}\right.$$
$$\left. + \alpha^T_{nJF}\frac{3[(\mathbf{u}^* \cdot \mathbf{F})(\mathbf{u} \cdot \mathbf{F}) + (\mathbf{u} \cdot \mathbf{F})(\mathbf{u}^* \cdot \mathbf{F})] - 2\mathbf{F}^2}{2F(2F-1)}\right\}\text{(C.30)}$$

where

$$\alpha^s_{nJF} = \alpha^s_{nJ} = \frac{1}{\sqrt{3(2J+1)}}\alpha^{(0)}_{nJ},$$

$$\alpha^v_{nJF} = (-1)^{J+I+F}\sqrt{\frac{2F(2F+1)}{F+1}}\left\{\begin{array}{ccc} F & 1 & F \\ J & I & J \end{array}\right\}\alpha^{(1)}_{nJ},$$

$$\alpha^T_{nJF} = -(-1)^{J+I+F}\sqrt{\frac{2F(2F-1)(2F+1)}{3(F+1)(2F+3)}}$$
$$\times \left\{\begin{array}{ccc} F & 2 & F \\ J & I & J \end{array}\right\}\alpha^{(2)}_{nJ}. \qquad \text{(C.31)}$$

The coefficients α^s_{nJF}, α^v_{nJF} and α^T_{nJF} are the conventional scalar, vector, and tensor polarizabilities of the atom, respectively, in a particular hfs level. Note that the scalar polarizability α^s_{nJF} does not depend on F. This statement holds true only in the framework of our formalism, where the hfs splitting is omitted in the expression for the atomic transition frequency $\omega_{n'J'F'nJF}$ in the calculations for the atomic polarizability, that is, where the approximation $\omega_{n'J'F'nJF} = \omega_{n'J'nJ}$ is used. We emphasize that Eq. (C.30) is valid only when the coupling between different hfs levels $|nJF\rangle$ is negligible. Thus, Eq. (C.30) is less rigorous than Eq. (C.28).

It is clear from Eqs. (C.28) and (C.30) that the effect of the vector polarizability on the Stark shift is equivalent to that of a magnetic field with the induction vector

$$\mathbf{B}^{\text{fict}} = \frac{\alpha^v_{nJ}}{8\mu_B g_{nJ}J}i[\mathcal{E}^* \times \mathcal{E}] = \frac{\alpha^v_{nJF}}{8\mu_B g_{nJF}F}i[\mathcal{E}^* \times \mathcal{E}].\text{(C.32)}$$

Here μ_B is the Bohr magneton and g_{nJ} and g_{nJF} are the Landé factors for the fine-structure level $|nJ\rangle$ and the hfs level $|nJF\rangle$, respectively. The nonrelativistic value of the Landé factor g_{nJ} is given by [169]

$$g_{nJ} = g_L\frac{J(J+1) + L(L+1) - S(S+1)}{2J(J+1)}$$
$$+ g_S\frac{J(J+1) + S(S+1) - L(L+1)}{2J(J+1)}. \quad \text{(C.33)}$$

Here $g_L = 1$ and $g_S \simeq 2.0023193$ are the orbital and spin g-factors for the electron, respectively. When the contribution of the nuclear magnetic moment is neglected, the Landé factor g_{nJF} is

$$g_{nJF} = g_{nJ}\frac{F(F+1) + J(J+1) - I(I+1)}{2F(F+1)}. \quad \text{(C.34)}$$

The direction of the light-induced fictitious magnetic field $\mathbf{B}^{\text{fict}}$ is determined by the vector $i[\mathcal{E}^* \times \mathcal{E}]$, which is a real vector. The fictitious magnetic field has the following points in common with real magnetic fields: i) It is a pseudovector (i.e. it does not flip under a spatial reflection). ii) It flips under time reversal, the same as a real magnetic field. Note that creation of the fictitious magnetic field requires ellitically polarized light since $[\mathcal{E}^* \times \mathcal{E}] = 0$ for linear polarizations. Additionally, we note that the middle expression in Eq. (C.32) shows that $\mathbf{B}^{\text{fict}}$ is independent of F. Specifically, $\mathbf{B}^{\text{fict}}$ is the same for all hfs levels $|nJF\rangle$ of a fine-structure level $|nJ\rangle$. Furthermore, comparison between the middle and last expressions in Eq. (C.32) shows that the factor $\alpha^v_{nJF}/g_{nJF}F$ does not depend on F.

Appendix C.6. Surface interaction

Atoms experience a potential when they are close to a material surface. It is important to note that despite a large amount of research into this topic, the complexity of surface physics along with a lack of data mean that the form of this potential is still not rigorously known in general [175]. One useful form which may be approximately true in many cases is that of the potential induced by a flat surface [175]

$$V(x) = Ae^{-\alpha x} - \frac{C_3}{x^3}, \qquad \text{(C.35)}$$

where x is the distance from the atom to the surface, C_3 is the van der Waals coefficient, and A and α determine the height and range, respectively, of the short-range repulsion, and depend on both the material and the atom. Note that typical magnitudes of A and α are $A = 10^{18}$ Hz and $\alpha = 50$ nm^{-1} and for atoms a few nanometers away from the surface, the shot-range repulsion potential $Ae^{-\alpha x}$ can be neglected.

Now, the van der Waals coefficient for a cesium atom in its ground state near a perfect metal surface is $C_3^{(\text{metal})} = 4.5$ a.u. $= 4.39$ kHz μm^3 [176]. On the other hand, in the case of a dielectric medium with refractive index n, an approximate expression is $C_3 = (n^2 - 1)/(n^2 + 1)C_3^{(\text{metal})}$ [175]. In the case

we are interested, where the material is pure fused silica, and for a broad region around the cesium D_2-line wavelength $\lambda_0 = 852$ nm, $C_{3g} = 1.56$ kHz μm^3 for cesium in the $6S_{1/2}$ ground state. We note that the van der Waals coefficient C_{3e} for the cesium excited state $6P_{3/2}$ has not yet been accurately calculated in the manner of Ref. [176]. However, from the results of Refs. [177, 178] the ratio of excited to ground state values can be inferred to be $C_{3e}/C_{3g} = 1.98$.

The van der Waals potential depends on the curvature of the surface of the dielectric medium. The van der Waals potential of an atom near the surface of a cylindrical dielectric rod is given by [179, 180]

$$V(r) = \frac{\hbar}{4\pi^3\epsilon_0} \sum_{n=-\infty}^{\infty} \int_0^\infty dk \, [k^2 K_n'^2(kr)$$
$$+ (k^2 + n^2/r^2) K_n^2(kr)] \int_0^\infty d\xi \, \alpha(\mathrm{i}\xi) G_n(\mathrm{i}\xi), \tag{C.36}$$

where

$$G_n(\omega) = \frac{[\epsilon(\omega) - \epsilon_0] I_n(ka) I_n'(ka)}{\epsilon_0 I_n(ka) K_n'(ka) - \epsilon(\omega) I_n'(ka) K_n(ka)}. \tag{C.37}$$

Here $\epsilon(\omega)$ is the dynamical dielectric function and I_n is the modified Bessel function of the first kind.

Let us now use the above formulae to evaluate the van der Waals potential of a ground-state cesium atom near the surface of a silica fiber. The dynamical dielectric function of silica is given by [181]

$$\frac{\epsilon(\omega)}{\epsilon_0} = 1 + \frac{0.6961663\,\lambda^2}{\lambda^2 - 0.0684043^2} + \frac{0.4079426\,\lambda^2}{\lambda^2 - 0.1162414^2}$$
$$+ \frac{0.8974794\,\lambda^2}{\lambda^2 - 9.896161^2}, \tag{C.38}$$

where λ is in units of micrometers. Using the following approximate expression for the polarizability, $\alpha(\omega) = 2\pi\epsilon_0 c^3 \sum_{j\neq 0} g_j A_{j0}/[g_0\omega_{j0}^2(\omega_{j0}^2 - \omega^2)]$, we can evaluate the integral (C.36). We take into account four dominant lines of the atom, namely, $\lambda_{10} = 852.113$ nm, $\lambda_{20} = 894.347$ nm, $\lambda_{30} = 455.528$ nm, and $\lambda_{40} = 459.317$ nm (see [182]). The emission transition probabilities of these lines are $A_{10} = 3.276 \times 10^7$ s^{-1}, $A_{20} = 2.87 \times 10^7$ s^{-1}, $A_{30} = 1.88 \times 10^6$ s^{-1}, and $A_{40} = 8 \times 10^5$ s^{-1}. The statistical weights of the four corresponding upper states are $g_1 = 4$, $g_2 = 2$, $g_3 = 4$, and $g_4 = 2$. The statistical weight of the ground state is $g_0 = 2$.

Note that for a fiber radius a which is small compared to the atom-to-surface distance x, the van der Waals potential V is, in general, different from the flat-surface bulk-medium van der Waals potential $V_{\text{flat}} = -C_3/x^3$. In the flat surface case, C_3 was determined by [183] to be $C_3 = (\hbar/16\pi^2\epsilon_0) \int_0^\infty d\xi \, \alpha(\mathrm{i}\xi)[\epsilon(\mathrm{i}\xi) - \epsilon_0]/[\epsilon(\mathrm{i}\xi) + \epsilon_0]$. For cesium atoms and flat silica surfaces, this coefficient

is estimated to be $C_3 \cong 5.6 \times 10^{-49}$ J m$^3 \cong 4.1 \times 10^{-5}$ mK $\mu\text{m}^3 \cong 0.85$ kHz μm^3.

When the atom-to-surface distance x is comparable to or much larger than the light wavelength λ, due to the retardation effect, the surface-induced potential V reduces and is given as the retarded Casimir-Polder potential $V = -C_4/x^4$. The Casimir-Polder coefficient C_4 for the cesium-silica interaction can be estimated from the formula $C_4 = C_4^{\text{metal}}[(n^2 - 1)/(n^2 + 1)]\phi(n)$, where $C_4^{\text{metal}} = 6579$ a.u. is the Casimir coefficient for the cesium-metal interaction [184], $n = 1.45$ is the refractive index of silica, and $\phi(n)$ is a tabulated function [185, 186]. Using the value $\phi(n = 1.45) = 0.76$ [185, 186], we find $C_4 = 1787$ a.u. $= 92$ Hz μm^4.

The attractive part of the surface-induced potential contains the van der Waals potential and the retarded Casimir-Polder potential in two different limits, and can be effectively described by the potential $V = -C_4/[x^3(x + C_4/C_3)]$. The exact shape of the attractive part of the potential can be numerically calculated from the Lifshitz formula [187]. Such calculations have been performed for the interaction between a cesium atom in a ground or excited state and a silica dielectric with a planar or cylindrical surface [188]. For the ground-state atom and the planar dielectric, their calculation gives $C_3 = 1178$ Hz μm^3 and $C_4 = 154$ Hz μm^4.

Appendix C.7. Two-color trapping potential

The two-color trap [29, 74] stands as the only nanofiber trapping scheme (among many proposed [75, 29, 74, 118]) to have been implemented experimentally so far. In two-color trapping, atoms are confined near a nanofiber by balancing the respective attraction and repulsion of red- and blue-detuned guided fields. Although such a scheme provides only transverse confinement relative to the nanofiber axis, axial confinement can be implemented rather simply by introducing a counterpropagating red-detuned field, as in Vetsch *et al* [37] (Fig. C1). It is important to note that the ellipticity of the blue-detuned, running-wave guided mode field (due to the non-zero longitudinal component) gives rise to a vector light shift dependent on the Zeeman sublevel of the atom. This shift can be compensated by using a standing wave configuration for the blue-detuned field [76], as realized experimentally in [38].

Let us consider the scheme used by Vetsch *et al* [37] in more detail. Nanofiber fundamental modes $\boldsymbol{\mathcal{E}}_1$ and $\boldsymbol{\mathcal{E}}_2$ with red- and blue-detuned frequencies ω_1 and ω_2, respectively, were introduced to the nanofiber producing a trap minimum away from the nanofiber surface. More specifically, $\boldsymbol{\mathcal{E}}_1$ was formed by counter-propagating, x-polarized fields while $\boldsymbol{\mathcal{E}}_2$ was a single y-polarized field. The combined field of the two counter
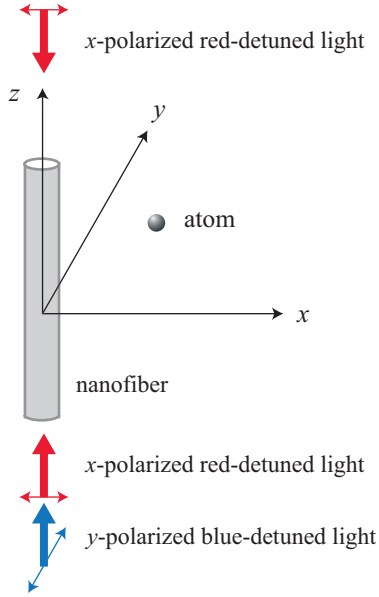
Figure C1. Illustration of the two-color trapping setup used in [37]. The counter-propagating x-polarized fields are red-detuned, and the y-polarized running-wave field is blue-detuned. From Fam Le Kien *et al* [189].

propagating, x-polarized red-detuned beams is

$$\boldsymbol{\mathcal{E}}_1 = A_1\{[\hat{\mathbf{x}}(e_r \cos^2\varphi - \mathrm{i}e_\varphi \sin^2\varphi) + \hat{\mathbf{y}}(e_r + \mathrm{i}e_\varphi)$$
$$\times \sin\varphi\cos\varphi]\cos\beta z + \mathrm{i}\hat{\mathbf{z}}e_z \cos\varphi\sin\beta z\}. \quad (\text{C.39})$$

Note that here, we have assumed that $z = 0$ is an antinode of the field's transverse component. We note that the total field is linearly polarized. For the y-polarized, blue-detuned field, we have

$$\boldsymbol{\mathcal{E}}_2 = A_2[\hat{\mathbf{x}}(e_r + \mathrm{i}e_\varphi)\sin\varphi\cos\varphi$$
$$+ \hat{\mathbf{y}}(e_r \sin^2\varphi - \mathrm{i}e_\varphi \cos^2\varphi) + \hat{\mathbf{z}}e_z \sin\varphi]\mathrm{e}^{\mathrm{i}\beta z}.(\text{C.40})$$

Note that in the expressions above, A_1 and A_2 can be calculated from the power in the fields. Eqs. (C.39) and (C.40) can be used to calculate the two-color trap potential as we show below.

To calculate the potential experienced by an atom in a two-color trap, both the optical potential U_{opt} and the potential induced by the nanofiber surface U_{surf} must be taken into account. That is, we must evaluate the potential

$$U = U_{\mathrm{opt}} + U_{\mathrm{surf}}. \quad (\text{C.41})$$

The optical potential is caused by the light shifts induced in the atom by the total field at each point in space, and can be obtained by diagonalizing the interaction Hamiltonian

$$H_{\mathrm{int}} = V^{\mathrm{hfs}} + V_R^{EE} + V_B^{EE}. \quad (\text{C.42})$$

In the above equation, V_R^{EE} and V_B^{EE} are the operators for the Stark interaction caused by the red- and blue-detuned light fields, respectively. Note that the mutual
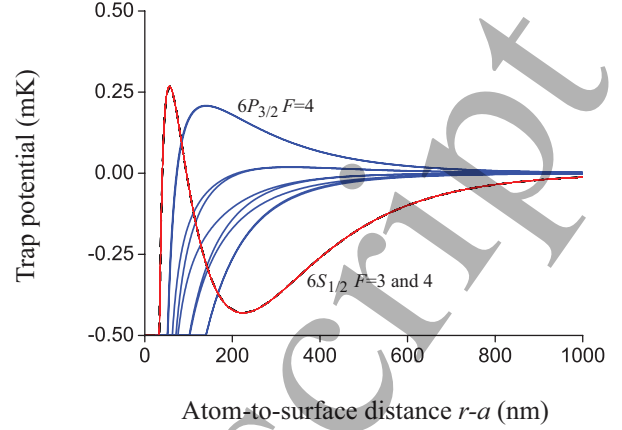

Figure C2. Radial potentials for ground and excited states of a cesium atom in a two-color nanofiber trap. Results for the sublevels of the excited-state hfs level $6P_{3/2}$ $F = 4$ are shown as solid blue curves, and those for the sublevels of the ground-state hfs levels $6S_{1/2}$ $F = 3$ and $6S_{1/2}$ $F = 4$ are shown as dashed black and solid red curves, respectively. Parameters are as given in the text, and he atom is located at azimuthal angle $\varphi = 0$ and $z = 0$.

detuning of the red-detuned and blue-detuned fields allows us to treat them separately, i.e., interference terms between the fields are ignored.

Figures C2, C3, and C4 show the radial, azimuthal, and axial dependences of the potentials, respectively, for hfs levels $F = 3$ (dashed black curves) and $F = 4$ (solid red curves) of the ground state $6S_{1/2}$ and for hfs level $F = 4$ (blue curves) of the excited state $6P_{3/2}$ of the atom [37]. The trap depth is about 0.43 mK, 1.75 mK, and 0.87 mK in the radial, azimuthal, and axial directions, respectively. Note that the potential for the excited state does not give a trap. Additionally, the axial trapping potential shows the expected array of trapping sites due to the standing-wave nature of the red-detuned field.

Detail of the potential for the ground-state hfs levels is shown in Fig. C3(b) for a region around the trap minimum at $\varphi = 0$. Degeneracy of the sublevels is lifted away from the points $\varphi = 0, \pm\pi$, and the energy separation between sublevels is seen to vary azimuthally. This is due to the azimuthal dependence of the vector Stark shift which is caused by the blue-detuned running wave field.

Note that the slight azimuthal displacement of the local minimum for the ground-state hfs sublevels is due to the change of sign of the longitudinal component, and the resulting change in sign of the differential shifts experienced by the Zeeman sublevels. Interestingly, this phenomenon can be understood as being due to a fictitious magnetic field, as discussed in more detail in Ref. [189].
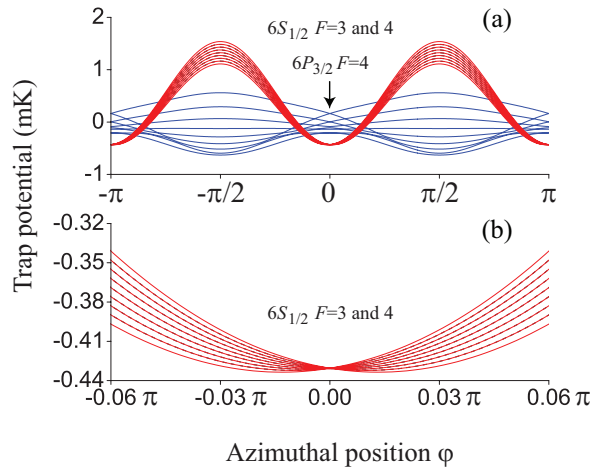
Nanofiber quantum photonics   53

Figure C3. (a) Azimuthal potentials for ground and excited states of a cesium atom in a two-color nanofiber trap. Results for the sublevels of the excited-state hfs level $6P_{3/2}\,F = 4$ are shown as solid blue curves, and those for the sublevels of the ground-state hfs levels $6S_{1/2}\,F = 3$ and $6S_{1/2}\,F = 4$ are shown as dashed black and solid red curves, respectively. Parameters are as given in the text, and the atom is located at azimuthal angle $\varphi = 0$ and $z = 0$. (b) Expanded view of the ground state potentials shown in Fig. C3(a) around the trap minimum at $\varphi = 0$. From Fam Le Kien *et al* [189].
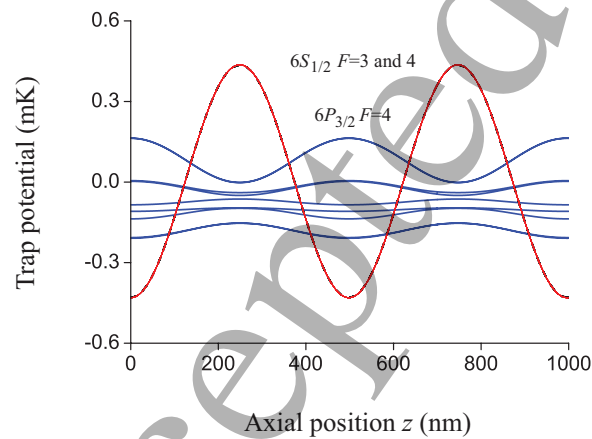

Figure C4. Axial dependence of the potentials of the ground and excited states of a cesium atom in the nanofiber-based trap. The sublevels of the excited-state hfs level $6P_{3/2}\,F = 4$ are shown as solid blue curves, and the sublevels of the ground-state hfs levels $6S_{1/2}\,F = 3$ and $6S_{1/2}\,F = 4$ are shown as dashed black and solid red curves, respectively. The radial distance and azimuthal position of the atom are $r - a = 224$ nm and $\varphi = 0$, respectively. For parameters of the trap, see the text. From Fam Le Kien *et al* [189].

References

[1] Politi A, Matthews J C F, Thompson M and O'Brien J L 2009 Integrated Quantum Photonics *IEEE Journal of selected Topics in Quantum Electronics* **15** 16731684

[2] O'Brien J L, Furusawa A and Vuckovic J 2009 Photonic quantum technologies *Natue Photonics* **3** 687695

[3] Ladd T D, Jelezko F, Laflamme R, Nakamura Y, Monroe C and O'Brien J L 2010 Quantum computers *Nature* **464** 4553

[4] Kimble H J 2008 The quantum internet *Nature* **453** 1023-1030

[5] Aspuru-Guzik A and Walther P 2012 Photonic quantum simulators *Nature Physics* **8** 285291

[6] Georgescu I M, Ashhab S and Nori F 2014 Quantum Simulation *Rev. Mod. Phys.* **86** 153185

[7] Kimble H J, Levin Y, Matsko A B, Thorne K S and Vyatchanin S P 2001 Conversion of conventional gravitational-wave interferometers into quantum nonde-molition interferometers by modifying their input and/or output optics *Phys. Rev. D* **65** 022002

[8] Kimble H J 1994 Cavity Quantum Electrodynamics *Advances in Atomic, Molecular, and Optical Physics Supplement 2, Academic Press, Boston, Ch. Structure and Dynamics in Cavity Quantum Electrodynamics* pp. 203-267.

[9] Kimble H J 1998 Strong Interactions of Single Atoms and Photons in Cavity QED *Phys. Scr.* **1998** 127

[10] McKeever J, Boca A, Boozer A D, Buck J R and Kimble H J 2003 Experimental realization of a one-atom laser in the regime of strong coupling *Nature* **425** 268-271.

[11] Reiserer A and Rempe G 2015 Cavity-based quantum networks with single atoms and optical photons *Rev. Mod. Phys.* **87** 1379

[12] Thompson J D, Tiecke T G, de Leon N P, Feist J, Akimov A V, Gullans M, Zibrov A S, Vuletic V and Lukin M D 2013 Coupling a Single Trapped Atom to a Nanoscale Optical Cavity. *Science* **340** 1202

[13] Tiecke T G, Thompson J D, de Leon N P, Liu L R, Vuletic V and Lukin M D 2014 Nanophotonic quantum phase switch with a single atom *Nature* **508** 241-244

[14] Goban A, Hung C L, Hood J D, Yu S P, Muniz J A, Painter O and Kimble H J 2015 Superradiance for Atoms Trapped along a Photonic Crystal Waveguide *Phys. Rev. Lett.* **115** 063601

[15] Vahala K J 2003 Optical microcavities *Nature* **424** 839846

[16] Aoki T, Dayan B, Wilcut E, Bowen W P, Parkins A S, Kippenberg T J, Vahala K J and Kimble H J 2006 Observation of strong coupling between one atom and a monolithic microresonator *Nature* **443** 671674

[17] Junge C, OShea D, Volz J and Rauschenbeutel A 2013 Strong Coupling between Single Atoms and Nontransversal Photons *Phys. Rev. Lett.* **110** 213604

[18] Akimov A V, Mukherjee A, Yu C L, Chang D E, Zibrov A S, Hemmer P R, Park H and Lukin M D 2007 Generation of single optical plasmons in metallic nanowires coupled to quantum dots *Nature* **450** 402406

[19] Chang D E, Thompson J D, Park H, Vuletic V, Zibrov A S, Zoller P and Lukin M D 2009 Trapping and Manipulation of Isolated Atoms Using Nanoscale Plasmonic Structures *Phys. Rev. Lett.* **103** 123004

[20] Gullans M, Tiecke T G, Chang D E, Feist J, Thompson J D, Cirac J I, Zoller P and Lukin M D 2012 Nanoplasmonic Lattices for Ultracold Atoms *Phys. Rev. Lett.* **109** 235309

[21] Phillips D F, Fleischhauer A, Mair A, Walsworth R L and Lukin M D 2001 Storage of Light in Atomic Vapor *Phys. Rev. Lett.* **86** 783

[22] Duan L M, Lukin M D, Cirac J I and Zoller P 2001 Long-distance quantum communication with atomic ensembles and linear optics *Nature* **414** 413-418

Nanofiber quantum photonics 54

[23] Patnaik A K, Liang J Q and Hakuta K 2002 Slow light propagation in a thin optical fiber via electromagnetically induced transparency *Phys. Rev. A* **66** 063808

[24] Tong L, Gattass R R, Ashcom J B, He S, Lou J, Shen M, Maxwell I and Mazur E 2003 Subwavelength-diameter silica wires for low-loss optical wave guiding *Nature* **426** 816

[25] Brambilla G 2010 Optical fibre nanowires and microwires: a review *J. Opt. A* **12** 043001

[26] Tong L and Sumetsky M 2010 *Subwavelength and Nanometer Diameter Optical Fibers* (Zhejiang University Press and Springer).

[27] Tong L, Zi F, Guo X and Lou J 2012 Optical microfibers and nanofibers: A Tutorial *Opt. Commun.* **285** 4641-4647

[28] Wu X, Tong L 2013 Optical microfibers and nanofibers *Nanophotonics* **2** 407-428

[29] Kien F L, Balykin V I and Hakuta K 2004 Atom trap and waveguide using a two-color evanescent light field around a subwavelength-diameter optical fiber *Phys. Rev. A* **70** 063403

[30] Kien F L, Balykin V I and Hakuta K 2005 State-insensitive trapping and guiding of Cesium atoms using a two-color evanescent field around a subwavelength-diameter fiber *J. Phys. Soc. Japan* **74** 910917

[31] Kien F L, Dutta Gupta S, Balykin V I and Hakuta K 2005 Spontaneous emission of a cesium atom near a nanofiber: Efficient coupling of light to guided modes *Phys. Rev. A* **72** 032509

[32] Kien F L, Balykin V, Hakuta K, 2006 Scattering of an evanescent light field by a single cesium atom near a nanofiber *Phys. Rev. A* **73** 13819

[33] Nayak K P, Melentiev P N, Morinaga M, Kien F L, Balykin V I and Hakuta K 2007 Optical nanofiber as an efficient tool for manipulating and probing atomic fluorescence *Opt. Express* **15** 5431

[34] Sague G, Vetsch E, Alt W, Meschede D and Rauschenbeutel A 2007 Cold-atom physics using ultrathin optical fibers: light-induced dipole forces and surface interactions *Phys. Rev. Lett.* **99** 163602

[35] Nayak K P, and Hakuta K 2008 Single atoms on an optical nanofibre *New J. Physics* **10** 053003

[36] Nayak K, Kien F L, Morinaga M, Hakuta K 2009 Antibunching and bunching of photons in resonance fluorescence from a few atoms into guided modes of an optical nanofiber *Phys. Rev. A* **79** 021801(R)

[37] Vetsch E, Reitz D, Sague G, Schmidt R, Dawkins S T and Rauschenbeutel A 2010 Optical interface created by laser-cooled atoms trapped in the evanescent field surrounding an optical nanofiber *Phys. Rev. Lett.* **104** 203603

[38] Goban A, Choi K S, Alton D J, Ding D, Lacroute C, Pototschnig M, Thiele T, Stern N P, Kimble H J 2012 Demonstration of a state-insensitive, compensated nanofiber trap *Phys. Rev. Lett.* **109** 033603

[39] Fujiwara M, Toubaru K, Noda T, Zhao H Q and Takeuchi S 2011 Highly efficient coupling of photons from nanoemitters into single-mode optical fibers *Nano Lett.* **11** 4362

[40] Yalla R R, Nayak K P and Hakuta K 2012 Fluorescence photon measurements from single quantum dots on an optical nanofiber *Opt. Express* **20** 2932; arXiv:1112.0624v1 (2011)

[41] Schroder T, Fujiwara M, Noda T, Zhao H Q, Benson O and Takeuchi S 2012 A nanodiamond-tapered fiber system with high single-mode coupling efficiency *Opt. Express* **20** 10490

[42] Liebermeister L, Petersen F, Munchow A V, Burchardt D, Hermelbracht J, Tashima T, Schell A W, Benson O, Meinhardt T, Krueger A, Stiebeiner A, Rauschenbeutel A, Weinfurter H and Weber M 2014 Tapered fiber coupling of single photons emitted by a deterministically positioned single nitrogen vacancy center *Appl. Phys. Lett.* **104** 031101

[43] Yalla R R, Kien F L, Morinaga M and Hakuta K 2012 Efficient channeling of fluorescence photons from single quantum dots into guided modes of optical nanofiber *Phys. Rev. Lett.* **109** 063602

[44] Gouraud B, Maxein D, Nicolas A, Morin O and Laurat J 2015 Demonstration of a memory for tightly guided light in an optical nanofiber *Phys. Rev. Lett.* **114** 180503

[45] Sayrin C, Clausen C, Albrecht B, Schneeweiss P and Rauschenbeutel A 2015 Storage of fiberguided light in a nanofiber-trapped ensemble of cold atoms *Optica* **2** 353-356

[46] Sorensen H L, Beguin J B, Kluge K W, Iakoupov I, Sorensen A S, Muller J H, Polzik E S and Appel J 2016 Coherent backscattering of light off one-dimensional atomic strings *Phys. Rev. Lett.* **117** 133604

[47] Corzo N V, Gouraud B, Chandra A, Goban A, Sheremet A S, Kupriyanov D, Laurat J 2016 Large bragg reflection from one-dimensional chains of trapped atoms near a nanoscale waveguide *Phys. Rev. Lett.* **117** 133603

[48] Kien F L and Hakuta K 2009 Cavity-enhanced channeling of emission from an atom into a nanofiber *Phys. Rev. A* **80** 053826

[49] Nayak K P, Kien F L, Kawai Y, Hakuta K, Nakajima K, Miyazaki H T and Sugimoto Y 2011 Cavity formation on an optical nanofiber using focused ion beam milling technique *Opt. Express* **19** 14040-14050

[50] Wuttke C, Becker M, Bruckner S, Rothhardt M and Rauschenbeutel A 2012 Nanofiber Fabry-Perot microresonator for nonlinear optics and cavity quantum electrodynamics *Opt. Lett.* **37** 1949-1951

[51] Nayak K P and Hakuta K 2013 Photonic crystal formation on optical nanofibers using femtosecond laser ablation technique *Opt. Express* **21** 2480-2490

[52] Yalla R, Sadgrove M, Nayak K P and Hakuta K 2014 Cavity quantum electrodynamics on a nanofiber using a composite photonic crystal cavity *Phys. Rev. Lett.* **113** 143601

[53] Schneeweiss P, Zeiger S, Hoinkes T, Rauschenbeutel A and Volz J 2017 Fiber ring resonator with a nanofiber section for chiral cavity quantum electrodynamics and multimode strong coupling *Opt. Lett.* **42** 85

[54] Kato S and Aoki T 2015 Strong Coupling between a Trapped Single Atom and an All-Fiber Cavity *Phys. Rev. Lett.* **115** 093603

[55] Mitsch R, Sayrin C, Albrecht B, Schneeweiss P and Rauschenbeutel A 2014 Quantum state-controlled directional spontaneous emission of photons into a nanophotonic waveguide *Nature Commun.* **5** 5713

[56] Sayrin C, Junge C, Mitsch R, Albrecht B, O'Shea D, Schneeweiss P, Volz J and Rauschenbeutel A 2015 Nanophotonic optical isolator controlled by the internal state of cold atoms *Phys. Rev. X* **5** 041036

[57] Snyder A W and Love J D, *Optical Waveguide Theory* (Kluwer, London, 2000)

[58] Yariv A, *Optical Electronics* (CBS College, New York, 1985)

[59] Marcuse D, *Light Transmission Optics* (Krieger, Malabar, 1989).

[60] Kien F L, Liang J Q, Hakuta K and Balykin V I 2004 Field intensity distributions and polarization orientations in a vacuum-clad subwavelength-diameter optical fiber *Opt. Commun.* **242** 445

[61] Tong L, Lou J and Mazur E 2004 Single-mode guiding properties of subwavelength-diameter silica and silicon wire waveguides *Opt. Express* **12** 1025

[62] Nha H and Jhe W 1997 Cavity quantum electrodynamics for a cylinder: Inside a hollow dielectric and near a solid

dielectric cylinder *Phys. Rev. A* **56** 2213

[63] Søndergaard T and Tromborg B 2001 General theory for spontaneous emission in active dielectric microstructures: Example of a fiber amplifier *Phys. Rev. A* **64** 033812

[64] Klimov V V and Ducloy M 2004 Spontaneous emission rate of an excited atom placed near a nanofiber *Phys. Rev. A* **69** 013812

[65] Kien F L and Hakuta K 2008 Effect of the orientation of a weak magnetic field on the radiative decay of a cesium atom near a nanofiber *Phys. Rev. A* **78** 063803

[66] Caves C M and Crouch D D 1987 Quantum wideband traveling-wave analysis of a degenerate parametric amplifier *J. Opt. Soc. Am. B* **4** 1535

[67] Blow K J, Loudon R, Phoenix S J D and Shepherd T J 1990 Continuum fields in quantum optics *Phys. Rev. A* **42** 4102

[68] Domokos P, Horak P and Ritsch H 2002 Quantum description of light-pulse scattering on a single atom in waveguides *Phys. Rev. A* **65**, 033832

[69] Kien F L, Busch T, Truong V G and Chormaic S N 2017 Channeling of spontaneous emission from an atom into the fundamental and higher-order modes of a vacuum-clad ultrathin optical fiber *Phys. Rev. A* **96** 043859

[70] Kien F L and Rauschenbeutel A 2014 Anisotropy in scattering of light from an atom into the guided modes of a nanofiber *Phys. Rev. A* **90** 023805

[71] Grimm R, Weidemüller M and Ovchinnikov Y B 2000 Optical Dipole Traps for Neutral Atoms *Adv. At., Mol., Opt. Phys.* **42** 95-170

[72] Schlosser N, Reymond G, Protsenko I and Grangier P 2001 Sub-poissonian loading of single atoms in a microscopic dipole trap *Nature* **411** 1024

[73] Greiner M, Mandel O, Esslinger T, Hänsch T W and Bloch I 2002 Quantum phase transition from a superfluid to a Mott insulator in a gas of ultracold atoms *Nature* (London) **415** 39

[74] Dowling J P and Gea-Banacloche J 1996 Evanescent Light-Wave Atom Mirrors, Resonators, Waveguides, and Traps *Adv. At., Mol., Opt. Phys.* **37** 1

[75] Balykin V I, Hakuta K, Kien F L, Liang J Q, and Morinaga M 2004 Atom trapping and guiding with a subwavelength-diameter optical fiber *Phys. Rev. A* **70** 011401(R)

[76] Lacroute C, Choi K S, Goban A, Alton D J, Ding D, Stern N P, Kimble H J 2012 A state-insensitive, compensated nanofiber trap *New. J. Phys.* **14** 023056

[77] Béguin J B, Bookjans E M, Christensen S L, Sørensen H L, Müller J H, Polzik E S and Appel J 2014 Generation and Detection of a Sub-Poissonian Atom Number Distribution in a One-Dimensional Optical Lattice *Phys. Rev. Lett.* **113** 263603

[78] Lee J, Grover J A, Hoffman J E, Orozco L A and Rolston S L 2015 Inhomogeneous broadening of optical transitions of 87 rb atoms in an optical nanofiber trap *Journal of Physics B: Atomic, Molecular and Optical Physics* **48** 165004

[79] Brambilla G, Finazzi V and Richardson D J 2004 Ultra-low-loss optical fiber nanotapers *Opt. Express* **12** 2258

[80] Stiebeiner A, Garcia-Fernandez R and Rauschenbeutel A 2010 Design and optimization of broadband tapered optical fibers with a nanofiber waist *Opt. Express* **18** 22677

[81] Hoffman J E, Ravets S, Grover J A, Solano P, Kordell P R, Wong-Campos J D, Orozco L A and Rolston S L 2014 Ultrahigh transmission optical nanofibers *AIP Adv.* **4** 067124

[82] Ravets S, Hoffman J E, Kordell P R, Wong-Campos J D, Rolston S L and Orozco L A 2013 Intermodal energy transfer in a tapered optical fiber: optimizing

transmission *J. Opt. Soc. Am. A* **30** 2361

[83] Ward J M, Maimaiti A, Le V H and Chormaic S N 2014 Optical micro- and nanofiber pulling rig *Rev. Sci. Instrum.* **85** 111501

[84] Nagai R and Aoki T 2014 Ultra-low-loss tapered optical fibers with minimal lengths *Opt. Express* **22** 28427

[85] Sorensen H L, Polzik E S and Appel J 2014 Heater Self-Calibration Technique for Shape Prediction of Fiber Tapers *J. Lightwave Tech.* **32** 1886

[86] Clohessy A M, Healy N, Murphy D F and Hussey C D 2005 Short low-loss nanowire tapers on singlemode fibres *Electron. Lett.* **41**, 954-955

[87] Sumetsky M 2006 How thin can a microfiber be and still guide light? *Opt. Lett.* **31** 870

[88] Sumetsky M, Dulashko Y, Domachuk P and Eggleton B J 2007 Thinnest optical waveguide: experimental test *Opt. Lett.* **32** 754-756

[89] Birks T and Li Y 1992 The shape of fiber tapers *J. Lightwave Technol.* **10** 432-438

[90] Frawley M C, Petcu-Colan A, Truong V G and Chormaic S N 2012 Higher order mode propagation in an optical nanofiber *Opt. Commun.* **285** 4648

[91] Dimmick T E, Kakarantzas G, Birks T A and Russell P St J 1999 Carbon dioxide laser fabrication of fused-fiber couplers and tapers *Appl. Opt.* **38** 6845-6848

[92] Stewart W J and Love J D 1985 Design limitation on tapers and couplers in single mode fibers *Proc. 5th IOOC/11th ECOC* 559-562

[93] Snyder A W and Love J D 1983 *Optical Waveguide Theory* (Chapman & Hall)

[94] Birks T A, Knight J C and Dimmick T E 2000 High-resolution measurement of the fiber diameter variations using whispering gallery modes and no optical alignment *IEEE Photn. Technol. Lett.* **12** 182

[95] Sumetsky M, Dulashko Y, Fini J M, Hale A and Nicholson J W 2006 Probing optical microfiber nonuniformities at nanoscale *Opt. Lett.* **31** 2393

[96] Sumetsky M and Dulashko Y 2010 Radius variation of optical fibers with angstrom accuracy *Opt. Lett.* **35** 4006

[97] Keloth J, Sadgrove M, Yalla R and Hakuta K 2015 Diameter measurement of optical nanofibers using a composite photonic crystal cavity *Opt. Lett.* **40** 4122-4125

[98] Madsen L S, Baker C, Rubinsztein-Dunlop H and Bowen W P 2016 Nondestructive Profilometry of Optical Nanofibers *Nano Lett.* **16** 7333-7337

[99] Fatemi F K, Hoffman J E, Solano P, Fenton E F, Beadie G, Rolston S L and Orozco L A 2017 Modal interference in optical nanofibers for sub-Angstrom radius sensitivity *Optica* **4** 157-162

[100] Wiedemann U, Karapetyan K, Dan C, Pritzkau D, Alt W, Irsen S and Meschede D 2010 Measurement of submicrometre diameters of tapered optical fibres using harmonic generation *Opt. Express* **18** 7693

[101] Xu Y, Fang W and Tong L 2017 Real-time control of micro/nanofiber waist diameter with ultrahigh accuracy and precision *Opt. Express* **25** 10434-10440

[102] Lai Y H, Yang K Y, Suh M G and Vahala K J 2017 Fiber taper characterization by optical backscattering reflectometry *Opt. Exp.* **25** 302043

[103] Morrissey M J, Deasy K, Chakrabarti S, Chormaic S N 2009 Tapered optical fibers as tools for probing magneto-optical trap characteristics *Review of Scientific Instruments* **80** 053102

[104] Russell L, Deasy K, Daly M J, Morrissey M J, Chormaic S N 2012 Sub-Doppler temperature measurements of laser-cooled atoms using optical nanofibres *Meas. Sci. Technol.* **23** 015201

[105] Russell L, Kumar R, Tiwari V, Chormaic S N 2013 Measurements on release recapture of cold 85Rb atoms using an optical nanofibre in a magneto-optical trap *Opt.*

Commun. **309** 313-317

[106] Kien F L and Hakuta K 2007 Spontaneous radiative decay of translational levels of an atom near a dielectric surface *Phys. Rev. A* **75** 013423

[107] Kien F L, Dutta Gupta S, and Hakuta K 2007 Optical excitation spectrum of an atom in a surface-induced potential *Phys. Rev. A* **75** 032508

[108] Nayak K, Das M, Kien F L, Hakuta K 2012 Spectroscopy of near-surface atoms using an optical nanofiber. *Opt. Commun.* **285** 4698

[109] Das M, Shirasaki A, Nayak K P, Morinaga M, Kien F L, Hakuta K 2010 Measurement of fluorescence emission spectrum of few strongly driven atoms using an optical nanofiber *Opt. Express* **18** 17154-17164

[110] Grover J A, Solano P, Orozco L A, Rolston S L 2015 Photon-correlation measurements of atomic-cloud temperature using an optical nanofiber *Phys. Rev. A* **92** 013850

[111] Ruddell S K, Webb K E, Herrera I, Parkins A S and Hoogerland M D 2017 Collective strong coupling of cold atoms to an all-fiber ring cavity *Optica* **4** 576

[112] Kien F L and Hakuta K 2008 Correlations between photons emitted by multiatom fluorescence into a nanofiber *Phys. Rev. A* **77** 033826

[113] Vetsch E, Dawkins S T, Mitsch R, Reitz D, Schneeweiss P, and Rauschenbeutel A 2012 Nanofiber-based optical trapping of cold neutral atoms *IEEE Journal of Selected Topics in Quantum Electronics* **18** 1763-1770

[114] Vetsch E 2010 Optical Interface Based on a Nanofiber Ph.D. thesis University of Mainz

[115] Wuttke C,Cole G D and Rauschenbeutel1 A 2013 Optically active mechanical modes of tapered optical fibers *Phys. Rev. A* **88** 061801(R)

[116] Reitz D, Sayrin C, Mitsch R, Schneeweiss P and Rauschenbeutel A 2013 Coherence properties of nanofiber-trapped cesium atoms *Phys. Rev. Lett.* **110** 243603

[117] Fu J, Yin X and Tong L 2007 Two-colour atom guide and 1D optical lattice using evanescent fields of high-order transverse modes *J. Phys. B: At. Mol. Opt. Phys.* **40** 41954210

[118] Sague G, Baade A and Rauschenbeutel A 2008 Blue-detuned evanescent field surface traps for neutral atoms based on mode interference in ultrathin optical fibres *New J. Phys.* **10** 113008

[119] Kien F L and Hakuta K 2009 Microtraps for atoms outside a fiber illuminated perpendicular to its axis: Numerical results *Phys. Rev. A* **80** 013415

[120] Kumar R, Gokhroo V, Tiwari V B and Chormaic S N 2016 Temperature measurement of cold atoms using transient absorption of a resonant probe through an optical nanofibre *J. Opt.* **18** 115401

[121] Reitz D, Sayrin C, Albrecht B, Mazets I, Mitsch R, Schneeweiss P and Rauschenbeutel A 2014 Backscattering properties of a waveguide-coupled array of atoms in the strongly nonparaxial regime *Phys. Rev. A* **89** 031804(R)

[122] Mitsch R, Sayrin C, Albrecht B, Schneeweiss P and Rauschenbeutel A 2014 Exploiting the local polarization of strongly confined light for sub-micrometer-resolution internal state preparation and manipulation of cold atoms *Phys. Rev. A* **89** 063829

[123] Petersen J, Volz J and Rauschenbeutel A 2014 Chiral nanophotonic waveguide interface based on spin-orbit interaction of light *Science* **346** 67

[124] Sadgrove M, Sugawara M, Mitsumori Y and Edamatsu K 2017 Polarization response and scaling law of chirality for a nanofibre optical interface *Sci. Rep.* **7** 17085

[125] Kien F L and Rauschenbeutel A 2014 Propagation of nanofiber-guided light through an array of atoms *Phys. Rev. A* **90** 063816

[126] Dawkins S T, Mitsch R, Reitz D, Vetsch E and Rauschenbeutel A 2011 Dispersive optical interface based on nanofiber-trapped atoms *Phys. Rev. Lett.* **107** 243601

[127] Solano P, Fatemi F K, Orozco L A and Rolston S L 2017 Dynamics of trapped atoms around an optical nanofiber probed through polarimetry *Opt. Lett.* **42** 2283

[128] Kien F L and Rauschenbeutel A 2013 Negative azimuthal force of nanofiber-guided light on a particle *Phys. Rev. A* **88** 063845

[129] Sadgrove M, Wimberger S and Chormaic S N 2016 Quantum coherent tractor beam effect for atoms trapped near a nanowaveguide *Sci. Rep.* **6** 28905

[130] Kumar R, Gokhroo V, Deasy K, Maimaiti A, Frawley M C, Phelan C and Chormaic S N 2015 Interaction of laser-cooled 87 Rb atoms with higher order modes of an optical nanofibre *New J. Phys.* **17** 013026

[131] Kien F L, Dutta Gupta S, Nayak K P and Hakuta K 2005 Nanofiber-mediated radiative transfer between two distant atoms *Phys. Rev. A* **72** 063815

[132] Kien F L and Hakuta K 2012 Cooperative enhancement of channeling of emission from atoms into a nanofiber *Adv. Nat. Sci.: Nanosci. Nanotechnol.* **3** 035001

[133] Kien F L and Hakuta K 2009 Slowing down of a guided light field along a nanofiber in a cold atomic gas *Phys. Rev. A* **79** 013818

[134] Kien F L and Hakuta K 2009 Intracavity electromagnetically induced transparency in atoms around a nanofiber with a pair of Bragg grating mirrors *Phys. Rev. A* **79** 043813

[135] Kien F L and Hakuta K 2011 Deterministic generation of a pair of entangled guided photons from a single atom in a nanofiber cavity *Phys. Rev. A* **84** 053801

[136] Kien F L and Rauschenbeutel A 2015 Electromagnetically induced transparency for guided light in an atomic array outside an optical nanofiber *Phys. Rev. A* **91** 053847

[137] Kien F L and Rauschenbeutel A 2016 Nanofiber-based all-optical switches *Phys. Rev. A* **93** 013849

[138] Kumar R, Gokhroo V, Deasy K and Chormaic S N 2015 Autler-townes splitting via frequency up-conversion at ultralow-power levels in cold 87Rb atoms using an optical nanofiber *Phys. Rev. A* **91** 053842

[139] Kumar R, Gokhroo V and Chormaic S N 2015 Multi-level cascaded electromagnetically induced transparency in cold atoms using an optical nanofibre interface *New J. Phys.* **17** 123012

[140] Invitrogen, Certificate of analysis Q21371MP 834674.

[141] Empedocles S A, Neuhauser R, Shimizu K and Bawendi M G 1999 Photoluminescence from single semiconductor nanostructures *Adv. Mater.* **11** 1243-1256

[142] Arians R, Kummell T, Bacher G, Gust A, Kruse C and Hommel D 2007 Room temperature emission from CdSe/ZnSSe/MgS single quantum dots *Appl. Phys. Lett.* **90** 101114

[143] Nirmal M, Dabbousi B O, Bawendi M G, Macklin J J, Trautman J K, Harris T D and Brus L E 1996 Fluorescence intermittency in single cadmium selenide nanocrystals *Nature* **383** 802-804

[144] Efros A L and Rosen M 1997 Random telegraph signal in the photoluminescence intensity of a single quantum dot *Phys. Rev. Lett.* **78** 1110-1113

[145] Kuno M, Fromm D P, Hamann H F, Gallagher A and Nesbitt D J 2000 Nonexponential blinking kinetics of single CdSe quantum dots: A universal power law behavior *J. Chem. Phys.* **112** 3117-3120

[146] Kuno M, Fromm D P, Hamann H F, Gallagher A and Nesbitt D J 2001 On/off fluorescence intermittency of single semiconductor quantum dots *J. Chem. Phys.* **115** 1028-1040

[147] Loudon R, *Quantum Theory of Light* 2000 (Oxford University Press, Oxford)

[148] In the company quotation, the quantum efficiency was measured relatively to rhodamine 101. We assume the quantum efficiency of rhodamine 101 to be 100%.

[149] Karstens T and Kobs K 1980 Rhodamine B and rhodamine 101 as reference substances for fluorescence quantum yield measurements *J. Phys. Chem.* **84** 1871-1872

[150] Stratton J A, *Electromagnetic Theory* 1941 (McGraw-Hill, New York); Chap. 6

[151] Morinaga M, Yalla R R, and Hakuta K 2015 Photon field in the presence of a nanofiber *Jpn. J. Appl. Phys.* **54** 072001

[152] Schell A W, Kewes G, Schroder T, Wolters J, Aichele T and Benson O 2011 A scanning probe-based pick-and-place procedure for assembly of integrated quantum optical hybrid devices *Rev. Sci. Instrum.* **82** 073709

[153] Neu E, Steinmetz D, Riedrich-Moller J, Gsell S, Fischer M, Schreck M and Becher C 2011 Single photon emission from silicon-vacancy colour centres in chemical vapour deposition nano-diamonds on iridium *New J. Phys.* **13** 025012

[154] Aharonovich I, Castelletto S, Simpson D A, Su C-H, Greentree A D and Prawer S 2011 Diamond-based single-photon emitters *Rep. Prog. Phys.* **74** 076501

[155] Fujiwara M, Zhao H Q, Noda T, Ikeda K, Sumiya H and Takeuchi S 2015 Ultrathin fiber-taper coupling with nitrogen vacancy centers in nanodiamonds at cryogenic temperatures *Opt. Lett.* **40** 5702-5705

[156] Skoff S M, Papencordt D, Schauffert H and Rauschenbeutel A 2016 An optical nanofiber based interface for single molecules *arXiv:1604.04259*

[157] Schell A W, Takashima H, Kamioka S, Oe Y, Fujiwara M, Benson O and Takeuchi S 2016 Highly efficient coupling of nanolight emitters to a ultra-wide tunable nanofibre cavity *Scientific Reports* **5** 9619

[158] Takashima H, Fujiwara M, Schell A W and Takeuchi S 2016 Detailed numerical analysis of photon emission from a single light emitter coupled with a nanofiber Bragg cavity *Opt. Express* **24** 15050-15058

[159] Li W, Du J, Truong V G and Chormaic S N 2017 Optical nanofiber-based cavity induced by periodic air-nanohole arrays *Appl. Phys. Lett.* **110** 253102

[160] Nayak K P, Zhang P and Hakuta K 2014 Optical nanofiber based photonic crystal cavity *Opt. Lett.* **39** 232-235

[161] Keloth J, Nayak K P and Hakuta K 2017 Fabrication of a centimeter-long cavity on a nanofiber for cavity quantum electrodynamics *Opt. Lett.* **42** 1003-1006

[162] Nayak K P, Keloth J and Hakuta K 2017 Fabrication of 1-D photonic crystal cavity on a nanofiber using femtosecond laser-induced ablation *J. Vis. Exp.* **120** e55136

[163] Sadgrove M, Yalla R, Nayak K P and Hakuta K 2013 Photonic crystal nanofiber using an external grating *Opt. Lett.* **38** 2542-2545

[164] Sadgrove M and Nayak K P 2017 Composite device for interfacing an array of atoms with a single nanophotonic cavity mode *New J. Phys.* **19** 063003

[165] Jones D E, Hickman G T, Franson J D and Pittman T B 2016 Nanofiber-segment ring resonator *Opt. Lett.* **41** 3683

[166] Jackson J D 1999 *Classical Electrodynamics* (Wiley, New York).

[167] Kaufman A M, Lester B J and Regal C A 2012 Cooling a single atom in an optical tweezer to its quantum ground state *Phys. Rev. X* **2** 041014

[168] Thompson J D, Tiecke T G, Zibrov A S, Vuletic V and Lukin M D 2013 Coherence and Raman sideband cooling of a single atom in an optical tweezer *Phys. Rev. Lett.* **110** 133001

[169] Metcalf H J and van der Straten P 1999 *Laser Cooling and Trapping* (Springer, New York)

[170] Allen L and Eberly J H 1975 *Optical Resonance and Two-Level Atoms* (New York, Wiley).

[171] Rosenbusch P, Ghezali S, Dzuba V A, Flambaum V V, Beloy K and Derevianko A 2009 ac Stark shift of the Cs microwave atomic clock transitions *Phys. Rev. A* **79** 013404

[172] Kien F L, Schneeweiss P and Rauschenbeutel A 2013 Dynamical polarizability of atoms in arbitrary light fields: general theory and application to cesium *Eur. Phys. J. D* **67** 92

[173] Manakov N L, Ovsiannikov V D and Rapoport L P 1986 Atoms in a laser field *Phys. Rep.* **141** 320

[174] Deutsch I H and Jessen P S 2010 Quantum control and measurement of atomic spins in polarization spectroscopy *Opt. Commun.* **283** 681

[175] Hoinkes H 1980 The physical interaction potential of gas atoms with single-crystal surfaces, determined from gas-surface diffraction experiments *Rev. Mod. Phys.* **52** 933

[176] Johnson W R, Dzuba V A, Safronova U I and Safronova M S 2004 Finite-field evaluation of the Lennard-Jones atom-wall interaction constant C_3 for alkali-metal atoms *Phys. Rev. A* **69** 022508

[177] Chevrollier M, Fichet M, Oria M, Rahmat G, Bloch D and Ducloy M 1992 High resolution selective reflection spectroscopy as a probe of long-range surface interaction : measurement of the surface van der Waals attraction exerted on excited Cs atoms *J. Phys. II France* **2** 631

[178] Courtois J Y, Courty J M and Mertz J C 1996 Internal dynamics of multilevel atoms near a vacuum-dielectric interface *Phys. Rev. A* **53** 1862

[179] Boustimi M, Baudon J, Candori P and Robert J 2002 van der Waals interaction between an atom and a metallic nanowire *Phys. Rev. B* **65** 155402

[180] Boustimi M, Baudon J and Robert J 2003 Molecules interacting with a metallic nanowire *Phys. Rev. B* **67** 045407

[181] Ghosh G 1997 *Handbook of Thermo-Optic Coefficients of Optical Materials with Applications* (Academic Press, New York)

[182] Sansonetti J E and Martin W C 2009 *Handbook of Basic Atomic Spectroscopic Data* http://physics.nist.gov/Handbook (Natl. Inst. Stand. Technol.: Gaithersburg)

[183] McLachlan A D 1964 Van der Waals forces between an atom and a surface *Mol. Phys.* **7** 381

[184] Marinescu M, Dalgarno A and Babb J F 1997 Retarded long-range potentials for the alkali-metal atoms and a perfectly conducting wall *Phys. Rev. A* **55** 1530

[185] Dzyaloshinskii I E, Lifshitz E M and Pitaevskii L P 1961 The general theory of van der Waals forces *Adv. Phys.* **10** 165

[186] Yan Z C, Dalgarno A and Babb J F 1997 Long-range interactions of lithium atoms *Phys. Rev. A* **55** 2882

[187] Lifshitz E M and Pitaevskii L P 1991 *Statistical Physics* (Pergamon, Oxford) Part 2

[188] Stern N P, Alton D J and Kimble H J 2011 Simulations of atomic trajectories near a dielectric surface *New J. Phys.* **13** 085004

[189] Kien F L, Schneeweiss P and Rauschenbeutel A 2013 State-dependent potentials in a nanofiber-based two-color trap for cold atoms *Phys. Rev. A* **88** 033840